



HAL
open science

Quadratic and cubic nonlinear optical responses of ZnO harmonic nanoparticles and KDP single crystals with incorporated metal oxides nanoparticles

Volodymyr Multian

► **To cite this version:**

Volodymyr Multian. Quadratic and cubic nonlinear optical responses of ZnO harmonic nanoparticles and KDP single crystals with incorporated metal oxides nanoparticles. Optics / Photonics. Université Savoie Mont Blanc, 2019. English. NNT: . tel-02406550

HAL Id: tel-02406550

<https://theses.hal.science/tel-02406550>

Submitted on 12 Dec 2019

HAL is a multi-disciplinary open access archive for the deposit and dissemination of scientific research documents, whether they are published or not. The documents may come from teaching and research institutions in France or abroad, or from public or private research centers.

L'archive ouverte pluridisciplinaire **HAL**, est destinée au dépôt et à la diffusion de documents scientifiques de niveau recherche, publiés ou non, émanant des établissements d'enseignement et de recherche français ou étrangers, des laboratoires publics ou privés.

THÈSE

Pour obtenir le grade de

**DOCTEUR DE LA COMMUNAUTE UNIVERSITE
GRENOBLE ALPES**

**préparée dans le cadre d'une cotutelle *entre la
Communauté Université Grenoble Alpes et Institute
of Physics, National Academy of Sciences of
Ukraine***

Spécialité : **Sciences pour l'Ingénieur**

Arrêté ministériel : le 6 janvier 2005 – 25 mai 2016

Présentée par

Volodymyr Multian

Thèse dirigée par **Ronan Le Dantec** et **Volodymyr Gayvoronsky**

Préparée au sein du **Laboratoire SYMME : Systèmes et
Matériaux pour la Mécatronique** dans l'Ecole Doctorale **SISEO**
et du **AMNOD laboratory: Advanced Materials Nonlinear
Optical Diagnostics**

**Propriétés optiques non linéaires du
deuxième et troisième ordre de
nanoparticules de ZnO et de cristaux
massifs de KDP dopés par des
nanoparticules d'oxydes métalliques**

Thèse soutenue publiquement le **4 octobre 2019**,
devant le jury composé de :

Fedir Sizov

Professeur, Institute of Semiconductor Physics, Kyiv, rapporteur

Bouchta Sahraoui

Professeur, Université d'Angers, rapporteur et président du jury

Volodymyr Gayvoronsky

Professeur, Institute of Physics NASU, Kyiv, directeur de thèse

Ronan Le Dantec

Professeur, Université Savoie Mont Blanc, directeur de thèse





THESIS

For the grade of

PhD OF THE COMMUNAUTÉ UNIVERSITE GRENOBLE ALPES

prepared in the framework of a cotutelle *between
the Community Université Grenoble Alpes and the
Institute of Physics of the National Academy of
Sciences of Ukraine*

Specialty: **Sciences for the Engineering**

Ministerial Order: January 6, 2005 - May 25, 2016

Presented by

Volodymyr MULTIAN

Thesis directed by **Ronan Le Dantec** and
Volodymyr Gayvoronsky

prepared in the **SYMME** laboratory: **System and Materials for
Mechatronics** in the Doctoral School **SISEO**
and **AMNOD** laboratory: **Advanced Materials Nonlinear Optical
Diagnostics**

Quadratic and cubic nonlinear optical responses of ZnO harmonic nanoparticles and KDP single crystals with incorporated metal oxides nanoparticles

Thesis public defense on October 4, 2019.

The jury composed of:

Fedir Sizov

Professor, Institute of Semiconductor Physics, Kyiv, Ukraine, reviewer

Bouchta Sahraoui

Professor, University of Angers, reviewer and president of the jury

Volodymyr Gayvoronsky

Professor, Institute of Physics NASU, Kyiv, Ukraine, thesis director

Ronan Le Dantec

Professor, SYMME, University of Savoie Mont Blanc, thesis director



Table of contents

List of abbreviations.....	3
Introduction	4
Chapter 1 Literature review	6
1.1 Harmonic nanoparticles	6
1.2 Composite materials based on KDP single crystals with incorporated inorganic NPs and organic impurities	14
Chapter 2 Experimental optical techniques	18
2.1 Elastic light scattering indicatrices technique	18
2.2 Nonlinear optical response of medium	24
2.3 Characterization of the nonlinear susceptibilities of HNPs.....	25
Conclusions to the chapter 2	39
Chapter 3 Nonlinear optical response of ZnO harmonic nanoparticles.....	41
3.1 Preparation of ZnO colloidal suspensions	42
3.2 Averaged third-order susceptibility from the interface scanning technique	43
3.3. Multiphoton microscopy of single ZnO nanoparticles	54
Conclusions to the chapter 3	63
Chapter 4 Characterization of different types of ZnO based nanostructures and bulk crystals	64
4.1 Studied materials	64
4.2 Influence of the synthesized ZnO NPs size on the nonlinear optical response.....	68
4.3 Multiphoton microscopy of raspberry-like ZnO NPs	73
4.4 Analysis of the energy structure and nonlinear optical response of bulk ZnO crystals with different content of intrinsic defects.....	75
Conclusions to the chapter 4	89
Chapter 5 Analysis of the optical harmonics generation efficiency of composite materials based on single crystals of KDP	90
5.1 Composites based on KDP single crystals	90
5.2 Nonlinear optical response of KDP single crystal with incorporated TiO ₂ nanoparticles	95
5.3 Influence of Al ₂ O ₃ ·nH ₂ O nanofibers incorporation in KDP single crystal on the nonlinear optical response.....	103
5.4 Influence of KDP single crystals doping by L-arginine on NLO response efficiency	111
Conclusions to the chapter 5	115
General Conclusion.....	116
Publications list.....	119
Appendix	122
References	129
Résumé en français	140

List of abbreviations

α – optical absorption coefficient	MeCN - acetonitrile
$\Delta\alpha$ – photoinduced variations of absorption coefficient	n – refractive index
ε – dielectric permittivity	Δn – photoinduced refractive index variation
ε_{scat} – scattering losses	NIR – near infrared range of spectra
λ – wavelength	NF – nanofiber
$\chi^{(2)}$, $\chi^{(3)}$ – quadratic/cubic nonlinear susceptibilities	NLO – nonlinear optics
BFO – BiFeO ₃	NOA – nanostructured oxyhydroxide of aluminum Al ₂ O ₃ · n (H ₂ O)
BS – beam splitter	ND - neutron diffraction
CB - conduction band	NP – nanoparticle
CCD– charge-coupled device	ns , ps , fs – nano-, pico-, femtosecond
CW – continuous wave excitation	P_0 – excitation power
DPSS – diode-pumped solid-state laser	PPG – propylene glycol
DT– deep traps	PD – photodiode
E_g – bandgap	PL – photoluminescence
EtOH – ethanol	PMT – photomultiplier
FOM – nonlinear quality factor	pNA – para-nitroaniline
FTIR – Fourier-transform infrared spectroscopy	SEM – scanning electron microscopy
FWHM – full width at half maximum	SH – second harmonic
HNP – harmonic nanoparticle	SHG – second harmonic generation
HRS – hyper-Rayleigh scattering	ST – shallow traps
HRS@SH(TH) - HRS at SH(TH)	T_0 – linear transmittance coefficient
IR – infrared range of spectra	ΔT – photoinduced transmittance variation
IS@TH – interface scanning technique at TH	TEM – transmission electron microscopy
i-PrOH - isopropyl alcohol	TH – third harmonic
k – wavenumber	THG – third harmonic generation
KDP – potassium dihydrogen phosphate (KH ₂ PO ₄)	THS – third harmonic scattering
KTP – KTiOPO ₄	UV – ultraviolet range of spectra
L – sample thickness	VB – valence band
L_{eff} – effective thickness	

Introduction

The development of advanced optical applications is often based on the combination of nonlinear optics (NLO) and nanophotonics. Design of new nanostructures and nanocomposite materials with high effective nonlinear optical response is thus of tremendous importance.

This work is focused on the study of two different materials. First, the so-called harmonic nanoparticles – a new type of biological markers that effectively convert laser frequency – will be introduced in the framework of bioimaging applications. A biomarker, or biological marker is a measurable indicator of some biological state or condition [1]. Biomarkers are used in many scientific fields. The most important parameters of biomarkers are: sensitivity, specificity, robustness, accuracy, reproducibility. Today one of the most widespread optical biomarkers is based on organic dyes that have many advantages but also suffering from such problems as emission saturation vs time, flickering and others. In this meaning the harmonic nanoparticles have high potential for practical application that will be described in next paragraphs.

Second part of the work contains the main characteristics of composite materials based on KDP single crystals, for which very interesting nonlinear optical properties have already been demonstrated. In general, KDP crystal has extremely high structural and optical perfection that make it possible to produce wide-aperture laser radiation frequency multipliers and Pockels cells for powerful laser setups [2,3]. However, one of the main functional restrictions for these crystals is the relatively low magnitude of the quadratic NLO susceptibility. Since KDP group crystals contain a developed hydrogen bonds network, they can effectively capture impurity centers of different nature.

The NLO materials with enhanced SHG efficiency are of interest due to their commercial importance in optical communication, signal processing, sensing, and instrumentation [4]. Though, the incorporation of organic and inorganic additives into KDP matrix can result in SHG efficiency enhancement

(anatase NPs [17], organic molecules [18, 19]) or reduction (amino acids [20]). Second part of the work is focused on the study of the influence of different types of additives on the response of the KDP crystal.

This work was done in the framework of a dual degree PhD “Cotutelle” program between France and Ukraine. One part of research was done in SYMME laboratory in Annecy and the second one in AMNOD laboratory in Kyiv. This thesis contains results obtained in both experimental laboratories.

Chapter 1 contains literature review for HNPs and KDP based composites.

Chapter 2 is focused on the description of the experimental techniques used for the harmonic nanoparticles and bulk crystals characterization.

Chapter 3 presents the main results obtained with commercial ZnO NPs (40-150nm). It contains two parts: (i) analysis of the THG efficiency from the ensemble measurement and (ii) study of the spectral response of single NPs.

Chapter 4 contains the characterization of the NLO properties of different ZnO based materials: (i) synthesized small NPs (<10nm); (ii) raspberry-like NPs - small NPs(<10nm) on the large NPs (<150nm); (iii) bulk crystals with different concentrations of defects.

Chapter 5 presents the diagnostics of KDP single crystals with enhanced quadratic and cubic NLO responses by incorporation TiO_2 , $\text{Al}_2\text{O}_3 \cdot n(\text{H}_2\text{O})$ nanoparticles/nanofibers and doping by L-arginine molecules.

The last part summarizes the main conclusions and presents the outlook for the future research work.

Chapter 1 Literature review

1.1 Harmonic nanoparticles

The optical microscopy field is continuously evolving in order to improve the resolution and contrast of images. Numerous methods, such as confocal, dark-field, phase-contrast and polarization microscopy, are shown as improvements to conventional optical microscopy. As a visualization tool, ordinary optical microscopy suffers from its low physical and chemical specificity. This can be eliminated by combining microscopy with spectroscopic techniques such as fluorescence, infrared or Raman spectroscopy [5].

Nonlinear optical microscopy is based on the strong interaction of light and matter, revealing specific chemical / biological properties and structures. The contrast of the obtained images is determined by the difference in the nonlinear optical properties of the object and the environment.

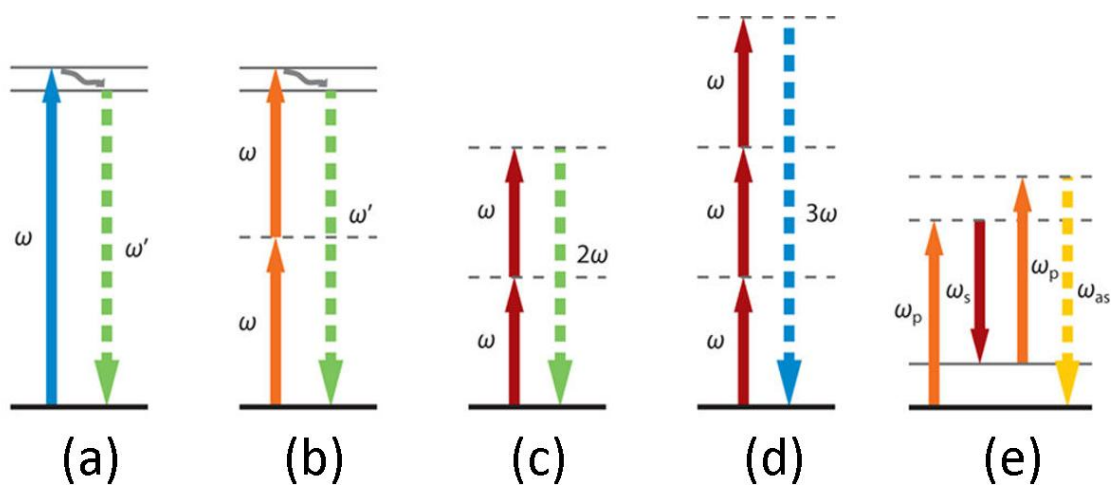


Fig. 1.1 Energy diagram for linear (luminescence) and nonlinear optical processes: (a) photoluminescence, (b) two photon luminescence, (c) second harmonic generation, (d) third harmonic generation, (e) CARS – coherent anti-Stokes Raman scattering. Dashed lines corresponds to the virtual states [6].

The efficiency of the interaction of light with matter is characterized by the dielectric susceptibility of the material. When the objects are excited by the radiation of halogen lamps or continuous (CW) lasers, the electromagnetic response is linear in relation to the magnitude of the incident light field.

However, with the use of pulsed laser radiation of high intensity, which usually exceeds several MW/cm^2 , a series of nonlinear optical effects, whose contributions depend on the intensity of excitation, are clearly manifested.

Typically, image formation in NLO microscopy is based on two types of NLO effects that result in the laser radiation frequency conversion: (i) the generation of optical harmonics, and (ii) the generation of combinational radiation through the excitation of vibrational resonances of chemical bonds. For the mentioned parametric processes, there is a generation of coherent radiation at wavelengths that differ from the wavelength of excitation [7].

Fig. 1.1 schematically presents energy diagrams for the following processes: photoluminescence with (a) single- and (b) two-photon excitation, generation of the second (SH) and third (TH) optical harmonics, and coherent anti-Stokes Raman scattering of light (CARS) [6]. Compared to fluorescence microscopy with single-photon excitation, multiphoton microscopy has an enhanced imaging depth and high spatial resolution (see Fig. 1.2) by reading the signal only from the region of the laser beam waist [8].

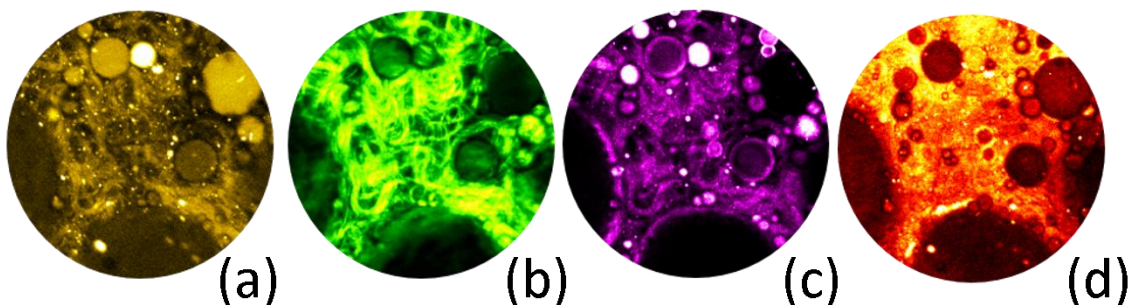


Fig. 1.2 Examples of simultaneously captured images using techniques of multiphoton microscopy for human breast cancer tissue excited in a transparency window: (a) two-photon fluorescence reflects fluorescence properties; (b) SHG – manifestation of noncentrosymmetry; (c) THG – manifestation of heterogeneity; (d) CARS is the chemical composition of the tissues [9].

In this context, Harmonic Nanoparticles (HNPs) are a new type of NLO markers for biological systems based on inorganic oxide nanocrystals with a noncentrosymmetric lattice that effectively convert laser radiation [10–12]. This term was introduced for the designation of a new broad class of nanoparticles

(NPs) that can simultaneously generate SH, TH and higher optical harmonics with high efficiency.

HNPs markers are promising for applications in the field of bio-imaging due to the possibility of changing the wavelength of excitation, the high depth of imaging [10] and photostability for long-term observation. Such markers can be easily identified through their optical harmonics signals against the background due to the response of the components of biological tissues [11,12].

Typical HNPs are: KNbO_3 , BiFeO_3 (BFO), LiNbO_3 , BaTiO_3 , $\text{Fe}(\text{IO}_3)_3$, $\text{Ba}(\text{BO}_2)_2$ (BBO), KTiOPO_4 (KTP), and ZnO [13]. In general, any NPs based on already known crystals - frequency converters of laser radiation, can be used as HNPs. Compared to typical fluorophore molecules, HNPs have a much narrower spectral response (see Fig. 1.3) and the harmonic signals are large enough to be detected in most of the standard nonlinear optical microscopy systems (see Fig. 1.4).

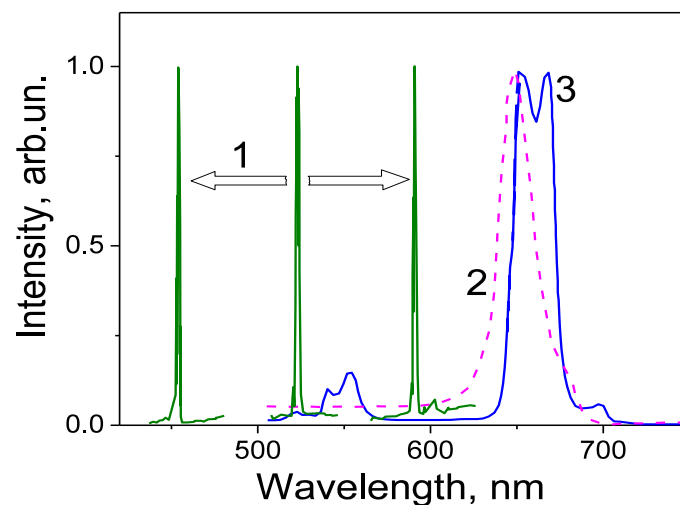


Fig. 1.3 An example of the possibility of tuning the narrow peaks of the SHG signals: (1) HNPs $\text{Sr}_{0.6}\text{Ba}_{0.4}\text{Nb}_2\text{O}_6$ with a size of 42 nm in comparison with the luminescence bands of (2) CdSe quantum dots with the size of 4 nm; (3) upconversion NPs $\text{NaYF}_4:\text{Er}^{3+}, \text{Yb}^{3+}$ with size of 18 nm under two-photon excitation [14].

Generally, an efficient generation of optical harmonics is obtained in nonlinear optical crystals under the conditions of phase synchronism or phase matching. Due to the strong dispersion of the refractive index, such conditions

can be fulfilled in a NLO crystal only in a limited range of excitation wavelengths, for specific crystal orientations and polarizations of the pump beam. However, if the size of the crystals does not exceed the coherent length (typically below one micron), these restrictions are removed [15].

Table 1.1 Normalized values of the spatially averaged nonlinear coefficients of various inorganic nanomaterials, and comparison of the response efficiency with two-photon excitation for different types of materials [11].

HNPs	KNbO ₃	LiNbO ₃ ,	BaTiO ₃	KTP	ZnO
$\langle d \rangle$, pm/V	3.4± 1.1	4.8± 1.6	4.6± 0.7	1.4± 0.3	1.9± 0.6
Marker			σ_{2P} , GM*		Ref.
Rhodamine 6G			150		[16]
Quantum dots			47x10 ³		[17]
BaTiO ₃ (120 nm)			13x10 ³		[18]

* The values are expressed in units of Goeppert-Mayer (1 GM = 10⁻⁵⁰ cm⁴·s·photon⁻¹)

Optical contrast based on the frequency doubling and tripling process can bring a number of benefits to bioimaging. First of all, as only virtual electronic states are involved, there is limited energy absorption, preventing bleaching, which is usually observed in fluorescent probes. Thus, it is possible to achieve observations over a long period of time without reducing the signal intensity [11]. In addition, SHG and THG are non-resonant processes that can occur for any wavelength of excitation [10,11,19]. Consequently, the pump wavelength can be tuned to a specific spectral range, where the absorption and scattering of biological tissues are low, which limits photo-degradation and increases the depth of penetration [20]. The correct selection of pump wavelength also avoids overlays with auto-fluorescence of the sample and thus increases the contrast of the image. Moreover, the SH signal from NPs has a quadratic dependence on the intensity of the excitation. Detection and visualization of such individual biological markers typically require high peak excitation power, which is now

easy to achieve with femtosecond laser sources, even at very moderate pulse energies [20,21].

In nonlinear microscopy, bleaching and blinking are well-known causes of image degradation. In the case of fluorescent probes, that reached the excited state when photons are absorbed, they can, with a negligible probability, pass on to another non-radiation-emitted excited state. Similarly, fluctuations in the intensity affecting radiation from quantum dots (blinking), as a consequence of capturing photo-excited electrons on the surface of HNPs, cannot occur with SHG and THG.

It is known that in the electro-dipole approximation, the intensity of the second optical harmonic increases as the square of the nanocrystal volume. This was confirmed in the literature for various noncentrosymmetric oxide nanocrystals [22–24]. When the particles size decreases, there is thus a significant reduction of the generation efficiency (NPs with two times smaller radius should generate 64 times lower SHG signal) that imposes restrictions for practical applications. HNPs have many attractive characteristics, but real biological implementation sometimes requires a decrease of the sizes of the NPs for the best permeability in biological tissues and their successful natural removal from the body [25,26]. Particles with dimensions less than 10 nm [25] may be interesting for some specific applications. In that case, harmonic generation efficiency has to be increased.

One approach for that is to combine a dielectric oxide core with a metal shell to amplify local fields through resonance excitation of surface plasmons. Among such materials, it is worth mentioning BaTiO₃ NPs with a gold shell, which demonstrated high SHG [27] or parametric amplification of light radiation [28]. A similar approach was observed for third harmonic generation of individual NPs located within a metallic nanoantenna gap that promotes the amplification of the local fields [29,30].

Generation of resonantly amplified SH is also well studied in pure metallic NPs [31], where the amplification of a local electric field is achieved

thanks to the contribution of plasmon resonances. Such nanostructures generate a NLO response due to surface effects or disturbances of the symmetry of excited modes [32], since the bulk second-order susceptibility tensor $\chi^{(2)}$ is zero due to the lattice's symmetry.

In recent years, nanophotonics have been intensively developed on the basis of all-dielectrics nanostructures as an alternative to plasmonics. This approach is based on the use of bulk resonances of the Mie-type - resonances of displacement currents - instead of the response of surface plasmons. In accordance with the Mie theory of scattering, the resonance [33] is located at $\lambda \sim nd$, where d is the characteristic size of the NP and n its refractive index. Although the field amplification in these dielectric structures is usually weaker than that of metallic analogs, their high Q factor factors allow to implement effective NLO responses. Nonlinear effects, such as SHG and THG, are also sensitive to resonant properties of dielectric nanostructures. This allowed the researchers to observe a significant gain in SHG and THG efficiency in dielectric and semiconductor materials [34,35].

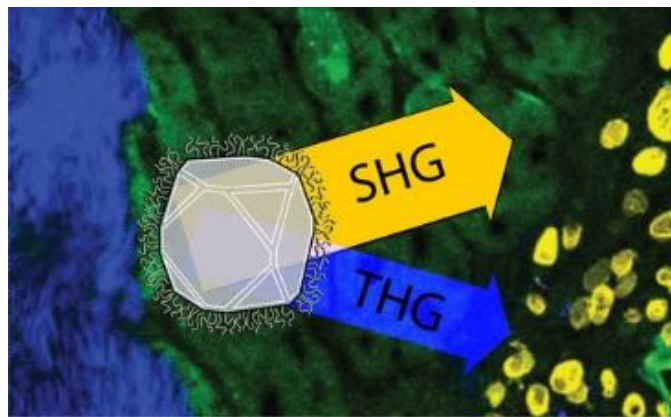


Fig. 1.4 An example of the simultaneous generation of signals of SH and TH by BiFeO₃ harmonic NPs in stem cells of human skeletal muscle [36].

Another approach to extending the range of application of harmonic nanoparticles is to create multifunctional nanoprobes that combine generation of optical harmonics at pulsed excitation and up-conversion with continuous laser excitation [37]. Unlike traditional fluorescent markers with UV excitation (quantum dots, fluorophore molecules), upconverting nanoparticles allow

pumping in the near-infrared range that can significantly reduce the contribution of tissue autofluorescence and increase imaging penetration in biological tissues up to 1 mm [36]. These new multifunctional nanoprobe combine resonant and nonresonant excitation conditions [38] with up-conversion and SHG processes and excitation in the first infrared window of biological tissues (700-900 nm), which extends the scope of applications of HNPs.

In the last few years, there has been a significant expansion of the use of HNPs, that requires a proper characterization of their nonlinear optical properties. At the beginning, the main attention was concentrated on the study of second harmonic generation, but over time, for more advanced applications, the response at the third and higher optical harmonics become relevant. Indeed, measuring the signals of several harmonics at the same time and comparing these images can significantly improve the accuracy of the identification of the HNPs against the background from biological tissues.

In reference [36], BFO HNPs was used as a marker for stem cells from human skeletal muscle (hMuStem) to study the feasibility of a therapeutic implementation of stem cell-based approaches, namely, their distribution and fixation. It was shown that the simultaneous measurement of SHG and THG allows to clearly identify the response from the HNPs against the response of biological tissues, for a significant increase in the selectivity of the images (see Fig. 1.4). The possibility of detecting 100 nm HNPs in muscle tissues, at a distance of more than 1 mm and with excitation in the second transparency window of the near-infrared range 1000 -1700 nm, has been demonstrated. These studies were performed for 14 days without any modification of the proliferative and morphological features of hMuStem cells. Other studies have also shown high biocompatibility of such NPs and efficiency for bioimaging applications [36].

Following these developments, it was then of particular interest to develop a quantitative method to measure the THG efficiency of the HNPs. From the experimental point of view, this measure is more complex compared to SHG.

One approach is to analyze harmonic signals from individual nanoparticles with multiphoton microscopy. However, it takes a lot of time for collecting a set of statistical data, and the results are difficult to analyze because NPs orientation is unknown [39–41].

For the study of SHG efficiency, as an alternative to microscopy, the hyper-Rayleigh scattering technique (HRS@SH) has been developed. HRS@SH is an experimental method based on the analysis of the scattered SH signal from a solution of molecules, which was then extended to the study of nanoparticles in colloidal suspensions [18-19]. Using this experimental technique, one can measure the orientation averaged second-order susceptibility of harmonic nanoparticles. The protocol is based on the comparison of the response from a colloidal suspension with the response from a reference solution of molecules [42–44], but applying this approach at the TH frequency(HRS@TH) is significantly more complicated and less precise from the experimental point of view.

In this work, an experimental method based on the interface scanning technique at third harmonic (IS@TH)[45], that will be described in the experimental section, was optimized to study HNPs. We indeed applied this experimental method (see chapter 3) to derive the averaged third-order susceptibility of ZnO nanoparticles and compared the obtained values with Third Harmonic Scattering measurements (HRS@TH). Initially, the interface scanning method has been developed to derive the third harmonic susceptibilities of liquids and gases [46].

Moreover, a linear scattering and laser beam self-action effect were also applied to study ZnO harmonic nanoparticles or more complex nanostructures (see chapter 4). Finally, nonlinear optical properties of ZnO harmonic nanoparticles were also studied using a multiphoton microscopy setup (see chapter 3), that was developed during my last year of PhD program at the SYMME laboratory.

1.2 Composite materials based on KDP single crystals with incorporated inorganic NPs and organic impurities

Single crystals of potassium dihydrogen phosphate, known as KDP (KH_2PO_4), deuterated KDP (DKDP or KD^*P), and ammonium dihydrogen phosphate, known as ADP ($\text{NH}_4\text{H}_2\text{PO}_4$) groups are widely used in nonlinear optics, optoelectronics and laser engineering. The high laser damage threshold and the possibility of growing crystals of large size makes these materials economically beneficial for the production of wide-aperture laser frequency converters and Pockels cells for powerful laser setups [47]. In KDP crystals, there is a large amount of hydrogen bonds, so they are able to effectively capture impurities of different nature [48], making them model objects for the search for new memory elements, substances for nonlinear optics and laser [49].

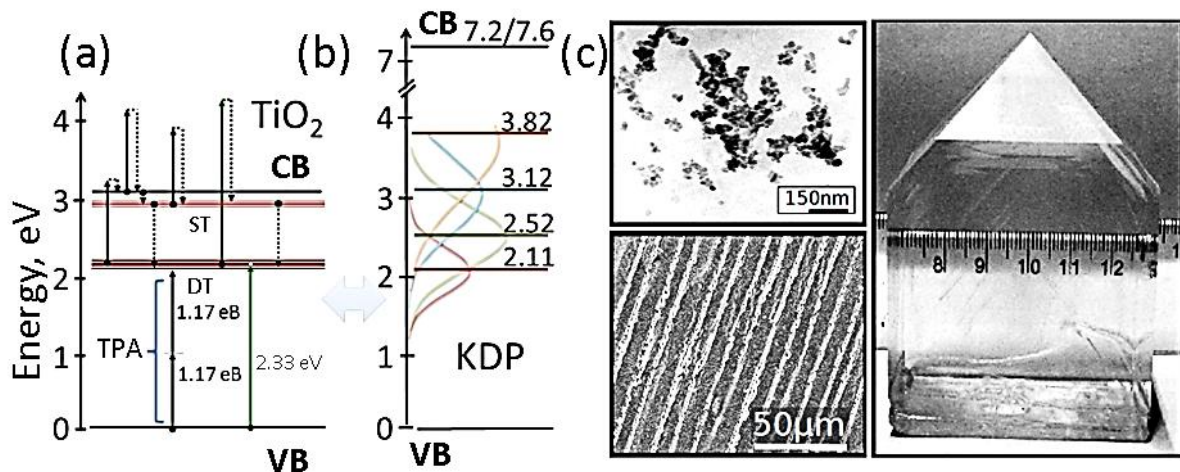


Fig. 1.5 Scheme of intrinsic defects energy levels (a) of nanocrystalline TiO_2 in the anatase modification [50,51] and (b) KDP single crystal [52]. For the anatase, the scheme of excitation/relaxation of carriers under the influence of laser radiation with quantum energies 1.17 eV (1064 nm) and 2.33 eV (532 nm) is given. VB and CB - valence band and conduction bands, ST and DT - shallow and deep traps. (c) Photo of KDP single crystals: TiO_2 with incorporated anatase NPs, TEM image of the NPs, and the structure of their layered entry into the KDP matrix.

However, due to the relatively low nonlinear coefficients of KDP, on practice it is more efficient to use different composites based on KDP matrix as “host” with different “guest” inclusions such as organic molecules or

nanoparticles. The influence of “guest” subsystems on “host” matrix will be described in literature review.

It is known that the doping of KDP crystals with complex organic molecules such as L-arginine leads to an increase of the efficiency of the second harmonic generation by 30-70% [53]. Doping KDP crystals with urea (carbamide) at a concentration of 2 wt. % leads to an increase of the efficiency of the SHG by 30% [2]. This is due to the additional deformation of the charged tetrahedron $(\text{PO}_4)^{3-}$ due to hydrogen bonds formation between the amino group of urea and the hydrophosphate (H_2PO_4) group of the crystalline matrix.

It was also shown that the incorporation of metal oxides nanoparticles into a crystalline matrix of nominally pure KDP leads, under certain conditions of excitation, to a amplification of the cubic NLO response [54], that is induced by a nonlocal transformation of the hydrogen bonds system around the NPs in the crystal [55]. The dimensions of the formed nanosized domains induced by NPs spontaneous polarization substantially increase the size of the NPs itself. As a result, at room temperature, the formation of an effective medium of "guest-host" type occurs, where the crystalline KDP matrix in the paraelectric state acts as the "host", and in the role of the "guest" - the NPs surrounded by a nonlocal layer of permeated hydrogen bounds of the KDP matrix. This leads to an increase in photoinduced changes of the macroscopic refractive index, leading to self-focusing phenomenon, which finally causes an increase of optical harmonics generation efficiency.

This approach was proposed for KDP:TiO₂ composites based on KDP crystals with incorporated anatase titanium dioxide nanoparticles [3] (see Fig. 1.5). It was discovered that the different growth sectors of the KDP and KDP:TiO₂ crystals have different SH efficiencies under excitation at 1064 nm [56]. As previously mentioned, this is due to an internal self-focusing effect of the pump beam caused by the high cubic nonlinear optical response from the incorporated NPs [57].

A reduction of the pulse duration of pumping from tens picoseconds to

few picoseconds [58], twice higher efficiency of the generation of sum frequency was obtained [64]. Under femtosecond pulsed excitation, a generation of a broadband optical continuum (400-800 nm) and three times higher SHG efficiency under excitation at 1.3 microns were obtained [59]. Previously, the effects of self-action in KDP single crystals with incorporated nanofibers of nanostructured oxyhydroxide of alumina (NOA) were studied [3]. In this dissertation work, it was shown that addition of such nanofibers also leads to a significant increase in the SHG efficiency (15-17 times) compared to nominally pure KDP with nanosecond excitation at 1064 nm [4].

Theoretical modeling work [60] showed that under continuous wave (CW) laser excitation and linear absorption in the KDP: TiO₂ crystal the efficiency of generation of the THz range radiation is several percent higher compared to nominally pure KDP crystal. The effect of two-photon absorption of ultrashort laser pulses can lead to gain in the THz range up to 15%, and the efficiency of the conversion of the laser radiation frequency can increase by 70% [61].

To summarize, research is being carried out in the field of composite materials based on dielectric matrices with incorporated organic impurities [49,62] and nanoparticles [48,57,63]. The contribution of the organic subsystem (organic molecules) consists in increasing the quadratic hyperpolarizability (anharmonic oscillations) of the group PO₄ in the periodic lattice of the crystal. It is estimated that the mentioned anharmonicity causes ~ 99% of a macroscopic quadratic NLO response of a nominally pure crystal [55], when the rest is related to the contribution of hydrogen bonds. The contribution of the inorganic subsystem (nanoparticles) is to enhance the macroscopic cubic NLO susceptibility, which results in efficient self-focusing of the saturated pump radiation with increasing excitation levels. Such composite media "Dielectric matrix with NPs /organic molecules" are very promising for the development of nonlinear optical elements for controlling the laser light and converting the frequency of laser radiation.

This literature review presents a set of different materials for various applications. These materials are at the initial research stage and should be better studied and optimized for practical implementation. However, taking into account their specificity, conventional optical experimental techniques are limited and cannot provide effective feedback for material scientists. For these reasons, new experimental approaches have been developed and will be presented in the following chapters.

Chapter 2 Experimental optical techniques

The development of advanced high-efficient materials requires detailed characterizations in order to understand the physical mechanisms in such newly designed objects and to optimize their properties. For this purpose, it is necessary to develop a set of techniques that provides a feedback to the synthesis of new materials. Important conditions for these experimental techniques are: (i) high sensitivity; (ii) rapid analysis; and (iii) nondestructive approach. Linear and nonlinear optical techniques are convincing for each of these points.

In this chapter, I will first present a light scattering experimental setup and show its interest for the study of nanomaterials. Then, three NLO response analysis techniques will be presented: (i) hyper-Rayleigh scattering (HRS), (ii) interface scanning technique for the TH generation efficiency measurements (IS@TH), (iii) self-action of continuous and pulsed laser beams with femto, pico, and nanosecond ranges of pulse duration. Finally, I will present the development of a multiphoton microscope based on a femtosecond tunable source. All these techniques have been developed in Kyiv and Annecy in order to carefully characterize linear and nonlinear optical properties of various nanomaterials.

2.1 Elastic light scattering indicatrices technique

Light scattering technique is an effective instrument for studying of the surface texture, optical quality of bulk materials, sizes and shapes of particles and microorganisms, etc. The analysis of the exact laser beam reflection, ballistic transmittance, angle distribution of the scattered light allows to obtain many optical parameters that describe the properties of material.

Conventional commercial products based on light scattering effects are designed to solve a specific limited task and range of application. You can easily measure a total reflectance/transmittance in the integrating sphere, estimation of

the size of the particles in dynamic laser scattering based devices, estimation of transmittance/absorbance in spectrophotometers, etc.

However, the study of novel materials requires designing new instruments with high sensitivity and resolution for measuring the light scattering effects. In this section a prototype of device for light scattering indicatrices measurements will be described. It allows measuring the scattered light distribution with high sensitivity and resolution. Data are then analyzed using a scattering model (for example Mie scattering theory [64]) that describes the multiple optical properties of the materials. This approach already allowed us to study for example samples of transparent NPs in transparent matrix [4], that wasn't possible before with the conventional UV-vis spectroscopy .

The cross-section of elastic optical scattering intensity distribution was studied with the designed experimental platform presented in Fig. 2.1 [65]. As sources, collimated beams (TEM_{00} mode) of continuous (CW) lasers were used at wavelengths of 405, 532, 660 and 1064 nm, whose power in the sample plane did not exceed 100 mW.

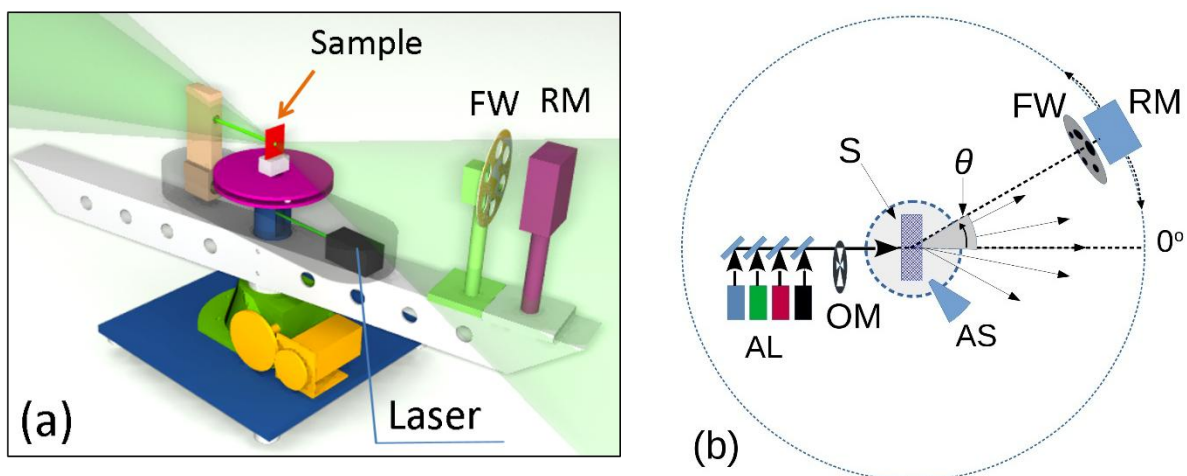


Fig. 2.1 a) Prototype of the instrument for measuring the cross-section of the elastic optical scattering indicatrix [65]. FW – wheel of neutral filters, RM – photodiode, photomultiplier, or CCD matrix (see appendix). b) Conceptual scheme of the setup: RM – registration module (PD, PMT, CCD), AS – angular position sensor, OM – optical modulator, AL – array of lasers (1064, 660, 532, 405 nm).

The laser beam passes through the rotation axis of the setup and is normal to the surface of the sample. The scattered radiation registration unit is located on the moving arm of the device. Rotation is realized by a stepper motor with an angular rotation sensor as feedback. This approach allows a rotation of the registration unit in the range of $-180^\circ < \theta < 180^\circ$ from the direction of propagation of the beam $\theta = 0^\circ$ with an angular resolution of $\sim 0.05^\circ$.

The registration of the signal $P(\theta)$ was carried out using a PD, PMT or CCD matrix (see Fig 1s.3 in appendix), in front of which a wheel with a set of neutral filters was placed in order to read the signal in the working range of the ADC.

For precision measurements, high-sensitive detectors were used in the wavelength range of excitation: in the visible and UV bands - a photomultiplier (Hamamatsu H10721-210 with a spectral sensitivity of 230-700 nm), a germanium photodiode in the near infrared range.

For signal readout, a 16-bit ADC was used with a measure of the unipolar signal from 0 to 10 volts. For complete covering of the intensity range from the background signal to the laser intensity peak, a set of five neutral filters with an optical density of 0.6 to 7 was used. To increase the sensitivity of measurements, the laser beam was modulated by an optical modulator with a frequency of 100 Hz. This approach allows to increase the signal-to-noise ratio and reduces the thermal effects in the sample. For example, the relative error of the scattering signal readout in the air does not exceed 15% in the perpendicular direction to the laser beam.

In general, the implementation of these approaches allowed to obtain a dynamic range of up to eight orders in the case of a photomultiplier and up to 6 orders of magnitude for a germanium photodiode. The high sensitivity of the developed device makes it possible to apply it for the study of a wide class of materials from highly absorbing and highly dispersive materials to transparent crystals.

For isotropic media, the scattering is axially symmetric, so it is enough to measure the cross-section of the angular light intensity distribution in one plane.

In the spherical coordinate system, the optical scattering indicatrix is determined by the power of the scattered radiation $\Delta P(\theta)$ in the solid angle $\Delta\Omega = 4\pi\sin^2(\Delta\theta / 2)$ along the direction of the zenith angle θ , $\Delta\theta = \text{arctg}(d / 2L)$ - the ratio of the aperture of the detector d to its distance from the rotation axis L . In the approximation of isotropic scattering, the integral transmittance coefficient ε_s in the cone $\gamma_1 \leq \theta \leq \gamma_2$ can be calculated from the equation [45]:

$$\varepsilon_s(\gamma_1, \gamma_2) = \frac{2\pi}{P_0} \int_{\gamma_1}^{\gamma_2} \frac{\Delta P(\theta)}{\Delta\Omega} \sin\theta d\theta, \quad (2.1)$$

where P_0 – incident power.

Knowing the angular distribution of scattered light, it is possible to separate the contributions of the ballistic transmittance of T_b along the direction of the laser beam and the extinction of light due to elastic scattering in the sample. For estimation of $T_b = \varepsilon_s(0, \theta_b)$ in the formula (2.1), integration is carried out in the range from 0 to the angular size $\theta_b = \text{arctg}(D/2L)$ of the collimated beam with a diameter D . The coefficient of elastic optical scattering losses in the forward hemisphere $\varepsilon_{scat} = \varepsilon_s(\theta_b, \pi/2)$ can be used as an effective metric for the analysis of the optical properties of various disperse materials.

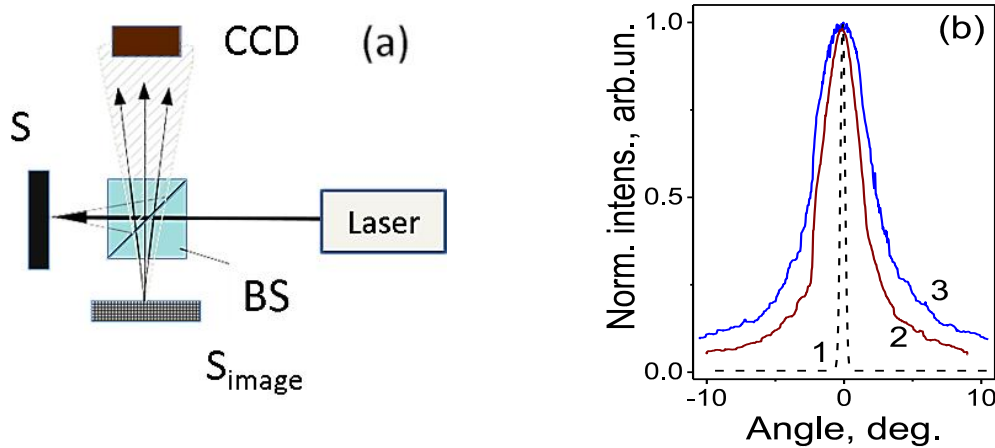


Fig. 2.2 (a) Scheme of extension to measure exact backscattering: S , S_{image} – sample and its image; BS – beam splitter; CCD – camera, photodiode or photomultiplier. (b) Manifestation of the self-defocusing effect in ZnO-II in the forward direction at a laser excitation intensity of 0.37 W/cm^2 (2) and 0.78 W/cm^2 (3), curve (1) corresponds to the free propagation of the laser beam [67].

In order to study the complete scattering indicatrix, a special extension was developed (see Fig. 2.2a), that allows to measure the reflected beam with the backscattered light in the range of $\pm 15^\circ$ from the normal (see the DR region in Fig. 2.3). In this scheme, the propagation of the laser beam and the sample position are aligned in order to place the image of the sample on the axis of rotation of the detector. For calibration a mirror with a known reflection coefficient is used.

As an example, linear scattering of $\text{Zn}_{1-x}\text{O}_{1-y}$ single crystals is shown in Fig. 2.3. They were grown by the hydrothermal method with different stoichiometry - ZnO-II ($x = 0.062$, $y = 0.060$) and ZnO-III ($x = 0.048$, $y = 0.051$) [67]. Fig. 2.2b shows a laser beam profile modification due to the passage through the sample ZnO-II (see chapter 4). The measured angular distribution of scattered radiation shows a self-defocusing effect due to the impact of delocalized carriers under continuous laser excitation at 532 nm

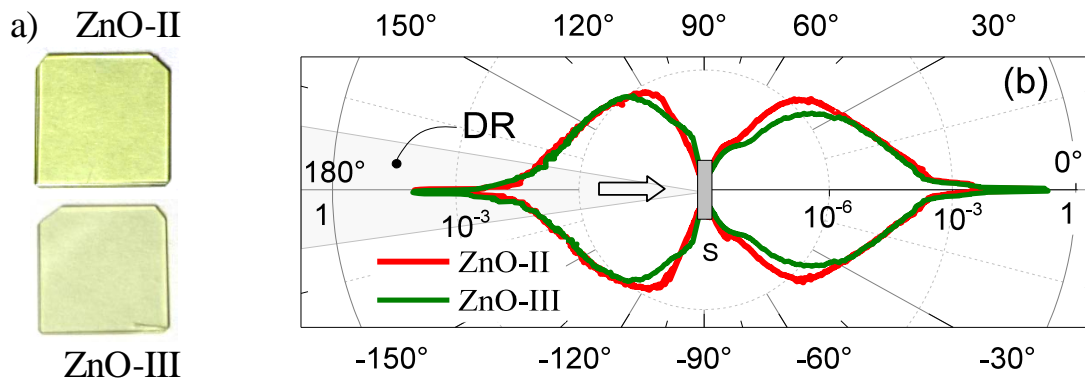


Fig. 2.3 (a) Photo of ZnO-II and ZnO-III crystals with different concentration of defects (b) Spatial distribution of elastic light scattering in ZnO crystals at 532 nm in polar coordinates (logarithmic scale on the radial axis). DR – exact backscattering region. S is the sample position. Arrow corresponds to the incident laser beam [67].

It was also shown the high sensitivity of the optical scattering indicatrix at 532 nm to the content of native defects. The analysis of the scattering indicatrix showed (see Fig. 2.3) that the crystals have higher losses in forward direction compared with the extinction in the opposite direction. The main differences in the angular distribution of the scattered intensities are observed in the ranges $30^\circ < |\theta| < 60^\circ$ and $100^\circ < |\theta| < 135^\circ$ in the forward and backward hemispheres,

respectively. It has also been shown that in these ranges, the ZnO-II crystal with a higher content of defects demonstrates higher scattering efficiency than observed for ZnO-III.

On the basis of the angle distribution, the coefficients of total transmittance of crystals $T = \varepsilon_s(0, \pi/2)$ and the reflection $R = \varepsilon_s(\pi/2, \pi)$ were calculated, that correlate with the data of transmission and reflection spectra for $\lambda = 532$ nm obtained by the integral sphere. Such an approach made it possible to correctly evaluate the optical absorption coefficients $\alpha = -\ln(T/(1-R))/d$, where d is the crystal thickness of crystals. It can be seen that the forward losses (22.7 / 18.5%) is higher than the backward one (5.9 / 5.1%). The estimated optical absorption for ZnO-II and ZnO-III crystals is about 5.1 / 4.2 cm^{-1} respectively. The obtained values of α correlate with the ratio of the molar content of oxygen vacancies. A more detailed analysis of the scattering indicatrix in ZnO crystals is described in chapter 3.

Moreover, the effect of TiO_2 and a nanostructured oxyhydroxide of aluminum nanofibers on the light scattering efficiency in $\text{KDP}:\text{TiO}_2$ and $\text{KDP}:\text{NOA}$, respectively, was analyzed (see chapter 4). A significant modification at large scattering angles was observed for these samples in comparison with the response of a nominally pure crystal KDP [68]. Particularly, for nominally pure KDP single crystals, the losses at 1064 nm are higher than those for $\text{KDP}:\text{TiO}_2$ crystals due to the lower concentration of uncontrolled impurities in $\text{KDP}:\text{TiO}_2$ (see Fig. 5.4) [69]. It has been shown that there is a correlation [4] between optical scattering losses in a $\text{KDP}:\text{NOA}$ and the concentration of NOA nanofibers (see Fig. 5.10) at 532 nm. This allows us estimate efficiency of inclusion of nanofibers into a crystalline matrix without the use of ultraviolet spectroscopy, where, in addition to the NOA, the response of uncontrolled impurities of transition metals are observed. These results demonstrate the interest of scattering technique for the characterization transparent composites, using different sources in the visible and near infrared ranges. More examples of studied materials are presented in appendix.

2.2 Nonlinear optical response of medium

In linear optics, the macroscopic polarization P induced in the medium by the electromagnetic field E (characterized by the frequency of oscillations ω and the wavelength $\lambda = 2\pi c/\omega$) is given by $P \propto \chi E$. According to this relation, the polarization is proportional to the field of the incident wave, and the linear response of the medium is characterized by the susceptibility χ . In this case the observed effects is linearly depends on the intensity of the incident wave, and the frequency remains unchanged. In nonlinear optics, the intensity of the incident electric field is much higher and the induced polarization is not proportional to the incident field: it is necessary to take into account the higher order susceptibilities $\chi^{(2)}$, $\chi^{(3)}$ that are tensors depending on the characteristics of the medium. For example the second harmonic generation is a second order optical process, that depends on $\chi^{(2)}$, and it is based on converting of the incident light wave frequency with generation of wave with doubled frequency. It should be noted that SHG can only be observed in noncentrosymmetric media. To generate the third harmonic, which depends on $\chi^{(3)}$ and occurs with tripling of the frequency of radiation, there is no limitation on the symmetry of the medium.

Definitions and general equations. When using lasers as sources of excitation, under the condition of high intensity of radiation, the connection between the polarization of the medium \mathbf{P} and the field \mathbf{E} loses the linear character (the boundary of applicability of the linear optics) and is written as:

$$\mathbf{P} = \chi^{(1)} \mathbf{E} + \chi^{(2)} \mathbf{E}\mathbf{E} + \chi^{(3)} \mathbf{E}\mathbf{E}\mathbf{E} + \dots \quad (2.2)$$

In this expression, each term corresponds to the manifestation of a certain physical effect in the environment. For example, elastic scattering ($\omega = \omega + 0$) corresponds to the prevailing contribution of the first term. Also, the generation of the second ($2\omega = \omega + \omega$) and the third ($3\omega = \omega + \omega + \omega$) optical harmonics, are described by the second and third terms, respectively, and will be studied in this work. Along with the non-degenerate cubic response, a degenerate response,

self-action of laser radiation ($\omega = \omega \pm (\omega - \omega)$) will be studied, that is a very sensitive mechanism for studying the properties of materials.

The coefficients χ , $\chi^{(2)}$, $\chi^{(3)}$.. in (2.2) describes the properties of the medium and their measurements is a primary task for most of nonlinear materials researches. There are many different techniques for the estimation of nonlinear susceptibilities of bulk materials. However, these techniques are generally not suitable for HNPs and only few nonlinear experimental techniques can be applied. Among them, hyper-Rayleigh scattering measurement, interface scanning technique and laser beam self-action techniques demonstrate the most promising results for nondestructive express analysis of nonlinear optical properties of HNPs.

2.3 Characterization of the nonlinear susceptibilities of HNPs

As described in the literature review, the characterization of the third order nonlinear optical properties of HNPs has becoming an important task since their THG signal was used in advanced imaging protocol based on SHG and THG co-localization [70]. For that purpose, a Third Harmonic Scattering technique has first been developed at the SYMME laboratory, which is based on a hyper-Rayleigh scattering set-up [23]. Following this first work, I used and optimized an experimental method based on the measurement of the third harmonic generation at the interface between a colloidal suspension and a silica cuvette. The experimental results obtained with ZnO colloidal suspensions, and the comparison between both experimental techniques, will be described in chapter 3.

2.3.1 Hyper-Rayleigh scattering at the second and third optical harmonics in colloidal suspensions of harmonic nanoparticles

In order to study the efficiency harmonics conversion, the hyper-Rayleigh scattering (HRS) technique can be applied. HRS was firstly designed to measure molecular hyperpolarizabilities and then applied to colloidal suspension of HNPs[23,71,72]. This technique allows to estimate the orientation-averaged

quadratic susceptibility $\langle |\chi_{NPS}^{(2)}|^2 \rangle^{1/2}$ of the NPs (further in the text we will refer quadratic and cubic susceptibilities as $\langle \chi_{NPS}^{(2)} \rangle$ and $\langle \chi_{NPS}^{(3)} \rangle$ correspondingly) of NPs.

Typically, this parameter can be estimated by a comparison of the colloidal suspension response with a reference solution with known molecule hyperpolarizability. Measurements are realized with the reference molecule of para-nitroaniline (pNA) dissolved in methanol in order to calibrate the response of the experimental setup at the SH wavelength.

More specifically, the second harmonic signal scattered by a colloidal suspension of HNPs can be expressed as:

$$I_{2\omega} = \frac{1}{4} G_{2\omega} \lambda_{2\omega}^{-4} N T_{2\omega} \langle (\chi_{NPS}^{(2)})^2 \rangle V^2 I_{\omega}^2, \quad (2.3)$$

where N – concentration of nanocrystals, V – average size of the NPs and I_{ω} – excitation intensity.

In this expression $G_{2\omega}$ describes the signal registration efficiency at SH wavelength, $\langle (\chi^{(2)})^2 \rangle$ – is the square of effective second-order susceptibility of nanocrystals, which is averaged over all orientations [73], and $T_{2\omega}$ is the field reduction coefficient describing the internal macroscopic field within the volume of nanocrystals [74].

Assuming quasi-spherical shape of NPs, $T_{2\omega} = (t_{\omega}^2 t_{2\omega})^2$ with $t_{\omega_i} = 3n_{sol}^2(\omega_i)/(2n_{sol}^2(\omega_i) + n_{NPS}^2(\omega_i))$ where $n_{sol}(\omega_i)$ and $n_{NPS}(\omega_i)$ correspond to the refractive index of the solvent and the NPs at ω_i , respectively.

Hyper-Rayleigh scattering technique can be also used for the analysis of third harmonic scattering by applying the two-step procedure described in [75]. At the first step standard HRS approach is applied to retrieve the averaged second order susceptibility, as described above. Then, TH scattering is recorded. A similar formalism can be used for a TH signal that is scattered perpendicularly:

$$I_{3\omega} = \frac{1}{16} G_{3\omega} \lambda_{3\omega}^{-4} N T_{3\omega} \langle (\chi_{NPS}^{(3)})^2 \rangle V^2 I_{\omega}^3, \quad (2.4)$$

where the factor 1/16 corresponds to the model described in [76]. $T_{3\omega}$ is defined here as $(t_{\omega}^3 t_{3\omega})^2$.

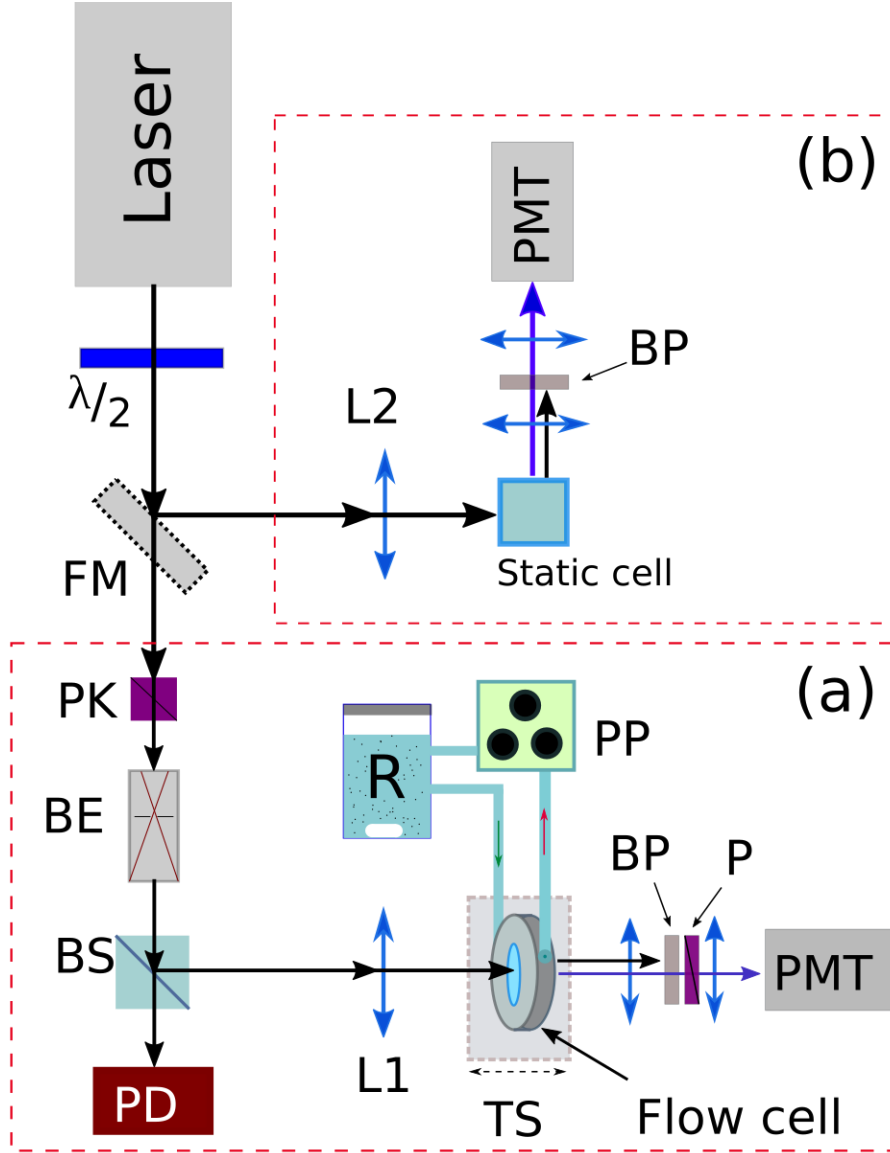


Fig. 2.4 Scheme of experimental setup [77]: (a) for THG efficiency measurements by interface scanning IS@TH. (b) SHG and THG signals readout in the perpendicular direction using the methods of HRS@SH and HRS@TH. BS - beam splitter; L1 and L2 focusing lenses; PD - photodiode; PMT - photomultiplier; $\lambda / 2$ - half-wave plate; P - polarizer; PC - polarization cube; BP - interference filters; TS - translation stage; BE - beam expander with pinhole; FM - folding mirror; PP - peristaltic pump, R - main reservoir.

The ratio between the two scattered harmonic signals can be used to estimate the averaged third order susceptibility $\langle \chi_{NPS}^{(3)} \rangle$. It should be noted that a more straightforward approach that uses an internal reference standard was

recently published by van Stetherhem, et al., to evaluate the second hyperpolarization of molecules [78]. It has not been implemented here, because it requires a higher excitation intensity and high-sensitivity signal registration equipment.

The experimental setup for the study of hyper-Rayleigh scattering (HRS) at second (HRS@SH) and third (HRS@TH) harmonics [75] is shown in Fig. 2.4b. A YAG laser (Wedge HB, Bright solutions, 1064 nm, pulse duration 1 ns, repetition rate of 1kHz) was used as pump source. In this scheme, the laser beam is focused by a lens L2 (focal length 3 cm) in the center of a 1 cm quartz square cuvette containing a colloidal suspension of NPs.

The registration of the SH and TH signals is carried out in perpendicular direction to the pump beam using a photomultiplier (Hamamatsu H10721-210) with two different bandpass filters (centered at 532 nm and 355 nm for SH and TH, respectively). A half-wave plate is used to rotate the input polarization and the intensity of the excitation can be tuned from 0 to 10 GW/cm².

2.3.2 Third harmonic generation at the interface

The interface scanning technique was firstly designed to measure the cubic susceptibility of liquids and gases [45]. The theoretical analysis of the THG signals obtained by scanning the interface between two media is described in detail in [79]. The TH intensity, that is generated by a strongly focused Gaussian beam propagating in the z direction, can be written as:

$$I(3\omega) = G(\omega) \left| b \int_{-\infty}^{\infty} d\xi \exp \frac{(ib\Delta k\xi)}{(1+2i\xi)^2} \chi^{(3)}(3\omega, \xi) \right|^2 I^3(\omega), \quad (2.5)$$

where $G(\omega)$ - experimental coefficient, that depends on the geometry and efficiency of the signals registration system, $\xi = z/b$ is the normalized distance with $\xi = 0$ at the focus and $I(\omega)$ the excitation intensity. Taking into account the diffraction limit, the confocal parameter can be expressed as $b = 2\pi \lambda^{-1} w_0 n(\omega)$, where $n(\omega)$ is the refractive index and w_0 is the radius of the beam waist in the focal plane. $\Delta k = 6\pi\lambda^{-1}(n(\omega) - n(3\omega))$ determines the phase mismatch between the excitation and the emitted TH optical field.

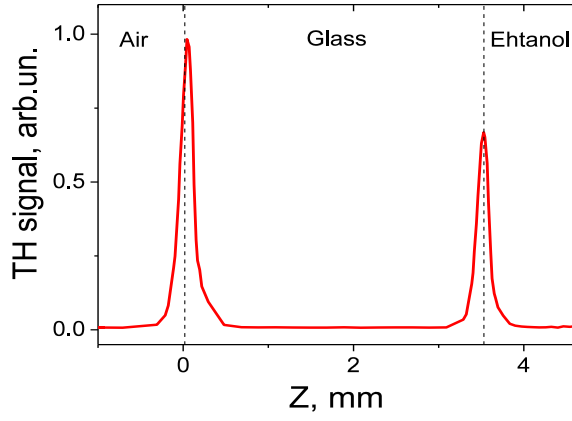


Fig. 2.5 Example of TH signal at the interfaces air/glass and glass/ethanol.

Isotropic media generate weak THG signals due to the Gouy phase shift [80,81] observed on each side of the focus, which leads to destructive interference in the forward direction. This limitation vanishes if the optical properties, namely the refractive index and the cubic susceptibility, differ along the

waist. The efficiency of THG significantly increases at the interface of two optically different materials [45,82], and for the intensity of the THG signal in the far field, a simplified expression can be written:

$$I(3\omega) = G(\omega) \left| \chi_1^{(3)} b_1 J(b_1 \Delta k_1) - \chi_2^{(3)} b_2 J(b_2 \Delta k_2) \right|^2 I^3(\omega), \quad (2.6)$$

where we have here neglected the reflection and absorption coefficients and made use of the dimensionless phase-matching integral $J(b\Delta k) = \int_0^\infty d\xi (1 + i2\xi)^{-2} \exp(ib\Delta k\xi)$ – dimensional integral of phase matching.

Registration of TH signals from two different interfaces (see Fig. 2.5) allows us to retrieve the parameters $G(\omega)$ and the excitation intensity $I(3\omega)$. Usually, a cuvette made of fused silica glass [83,84] with known cubic susceptibility $\chi^{(3)}(3\omega) = 1.99 \pm 0.15 \cdot 10^{-22} \text{ m}^2/\text{V}^2$ is used [76]. Taking into account that $\chi_{gl}^{(3)} \gg \chi_{air}^{(3)} \approx 0$, the ratio of the TH signals at the interfaces of the glass/solvent and glass/air, $I(3\omega)_{sol/gl}$ and $I(3\omega)_{gl/air}$, respectively, can be written from equation (2.6) as:

$$\frac{I(3\omega)_{sol/gl}}{I(3\omega)_{gl/air}} = \left[1 - \frac{\chi_{sol}^{(3)} b_{sol} J(b_{sol} \Delta k_{sol})}{\chi_{gl}^{(3)} b_{gl} J(b_{gl} \Delta k_{gl})} \right]^2. \quad (2.7)$$

From which cubic susceptibility of the solvent $\chi_{sol}^{(3)}$ can be expressed as:

$$\chi_{sol}^{(3)}(3\omega) = \chi_{gl}^{(3)}(3\omega) \frac{J(b_{gl}\Delta k_{gl})b_{gl}(\omega)}{J(b_{sol}\Delta k_{sol})b_{sol}(\omega)} \left(1 + \left[\frac{I(3\omega)_{sol/gl}}{I(3\omega)_{gl/air}} \right]^{\frac{1}{2}} \right). \quad (2.8)$$

An improved model [79], which takes into account the different reflections at the interfaces and the absorption in the medium, has been developed.

It should be noted that these additional corrections result in amendments less than 15% of the final values. In this case, the corrected signal peaks on the interfaces, R_{THG} , is expressed as:

$$R_{THG} = \frac{I(3\omega)_{sol/gl}}{I(3\omega)_{air/gl}} \times \frac{[1-r^2(\omega)_{gl/sol}]^3 [1-\tilde{\alpha}(\omega)_{gl}]^3}{[1-r^2(3\omega)_{gl/sol}] [1-\tilde{\alpha}(3\omega)_{gl}]}, \quad (2.9)$$

where $r_{gl/sol}(\omega) = [n_{gl}(\omega) - n_{sol}(\omega)] / [n_{gl}(\omega) + n_{sol}(\omega)]$ takes into account the reflection on the interfaces and the parameter $\tilde{\alpha}(\omega) = \{[1 - r(\omega)]^2 - t(\omega)\} / [1 - r(\omega)]^2$ corresponds to the absorption in a glass with a linear transmittance $t(\omega)$. Finally, all corrections that taking into account the reflection on the interface $\rho(\omega)$ and variations in the size of the beam waist and the confocal parameters $\beta(\omega)$ can be applied in the expression (2.8). Then we obtain:

$$\chi_{sol}^{(3)}(3\omega) = \chi_{gl}^{(3)}(3\omega) \frac{J(b_{gl/air}\Delta k_{gl})b_{gl/air}(\omega)}{J(b_{sol/gl}\Delta k_{sol})b_{sol/gl}(\omega)} \times (\beta(\omega)\rho(\omega) + \sqrt{R_{THG}}), \quad (2.10)$$

where

$$\beta(\omega) = \frac{J(b_{sol/gl}\Delta k_{gl})b_{sol/gl}(\omega)}{J(b_{gl/air}\Delta k_{gl})b_{gl/air}(\omega)}, \quad \rho(\omega) = \frac{[1-r_{sol/gl}^2(\omega)]^{\frac{3}{2}}}{[1-r_{sol/gl}^2(3\omega)]^{\frac{1}{2}}}.$$

We have just seen that third harmonic generation at the interface is a useful method to retrieve the cubic susceptibility of a liquid $\chi_{sol}^{(3)}$. In addition, this method can be applied for the analysis of colloidal suspensions of NPs. We can indeed use a Maxwell-Garnett effective medium model to estimate the effective susceptibility $\chi_{sol+NPs}^{(3)}$ of the colloidal suspensions. For a very low volume fraction f of NPs, the effective susceptibility $\chi_{sol+NPs}^{(3)}$ of a

nanocomposite consisting of randomly dispersed nanoparticles in a solvent can be written as [85]:

$$\chi_{sol+NPs}^{(3)} = f \left(\frac{3\epsilon_{sol}^{3\omega}}{\epsilon_{NPs}^{3\omega} + 2\epsilon_{sol}^{3\omega}} \right) \left(\frac{3\epsilon_{sol}^{\omega}}{\epsilon_{NPs}^{\omega} + 2\epsilon_{sol}^{\omega}} \right) \chi_{NPs}^{(3)} + \chi_{sol}^{(3)}, \quad (2.11)$$

where ϵ_{sol} and ϵ_{NPs} dielectric permittivity of the solvent and nanoparticles respectively.

For suspensions with a clearly defined NPs size without agglomerates, a linear dependence $\chi_{sol+NPs}^{(3)}$ vs volume fraction f is expected. This has been confirmed by experimental data, and allows us to estimate the orientation-averaged cubic NLO susceptibility $\langle \chi_{NPs}^{(3)} \rangle_{THG}$ for ZnO nanocrystals.

As shown in Fig. 2.4a, the laser beam of the YAG laser is focused by the lens L1 ($f = 5\text{cm}$) on the various interfaces of the filled cuvette, installed on the linear translation stage. TH signals propagating in the forward z direction are collected by lenses and measured by a photomultiplier (Hamamatsu H10721-210) with an interference filter located in front of it to cut off the pump signal and separate the third harmonic signal at 355 nm.

To monitor the laser power variations and adjust the intensity of a horizontally polarized excitation beam, a system consisting of a photodiode, a half-wave plate and a polarization cube is used. Note that a beam expander with a pinhole located after its focal plane also allows filtering the beam profile.

The optimal volume of the waist (tradeoff between the number of probed nanocrystals and the signal resolution at the interfaces), corresponds to a size of the waist $w_0 \approx 15 \mu\text{m}$ and a confocal parameter $b \approx 0.6 \text{ mm}$, that was estimated using the knife-edge technique. Possible artifacts that arise as a result of thermal processes within the readout area, fluctuations of the concentration and sticking of nanocrystals to the cell walls have also been reduced to a minimum. First, in order to avoid any optical damage of nanocrystals in suspensions and walls of cuvettes, the laser excitation energy was set below 20 μJ . However, for frequency repetition of laser radiation of 1 kHz, signal fluctuations, lead to

distortion of the results when a static cell is used. The detailed description of this issue will be presented in the next chapter.

2.3.3 Laser beam self-action effects

The value of the cubic susceptibility (degenerate one) can be obtained from the experiment based on laser beam self-action effect, when a nonlinear dependence of the polarization of the medium with the external field leads to the interaction of laser beams among themselves and the violation of the principle of superposition. This technique will be applied to study ZnO NPs and bulk ZnO crystals in chapter 4 and for KDP single crystal with incorporated NPs in chapter 5.

In isotropic media or crystalline structures with a center of inversion, there is a cubic nonlinearity of $\chi^{(3)}$. For such a medium [86]:

$$P = \chi E + \chi^{(3)} E^3. \quad (2.12)$$

In this approximation, the complex refractive index $\tilde{n} = n(1 + i\alpha/2k)$, (where: n is the real part of the refractive index, α - absorption coefficient, $k=2\pi/\lambda$ - wavevector) is determined by the formulas $D = E + 4\pi P = \varepsilon E = \tilde{n}^2$, where $\tilde{n} = (1 + 4\pi P/E)^{1/2}$. Taking to account (2.2) for the refractive index, we obtain the expression: $\tilde{n} = (1 + 4\pi(\chi + \chi^{(3)} E^2))^{1/2}$.

In the approximation of Kerr nonlinearity, the coefficients of two-photon absorption β and NLO refractive index n_2 (or the same Δn) are determined from the equations:

$$\alpha(I) = \alpha + \beta \cdot I, \quad n(I) = n_0 + n_2 \cdot I, \quad (2.13)$$

where α and n_0 — absorption and refractive index in linear mode, I – excitation intensity, that in the CGS system is related to the amplitude of the electric field as: $I [\text{erg}/(\text{cm}^2 \cdot \text{s})] = c\varepsilon E^2 / (8\pi) [\text{V}/\text{cm}]$, and in SI: $I [\text{W}/\text{m}^2] = 1/2 c n \varepsilon_0 E^2 [\text{V}/\text{m}]$.

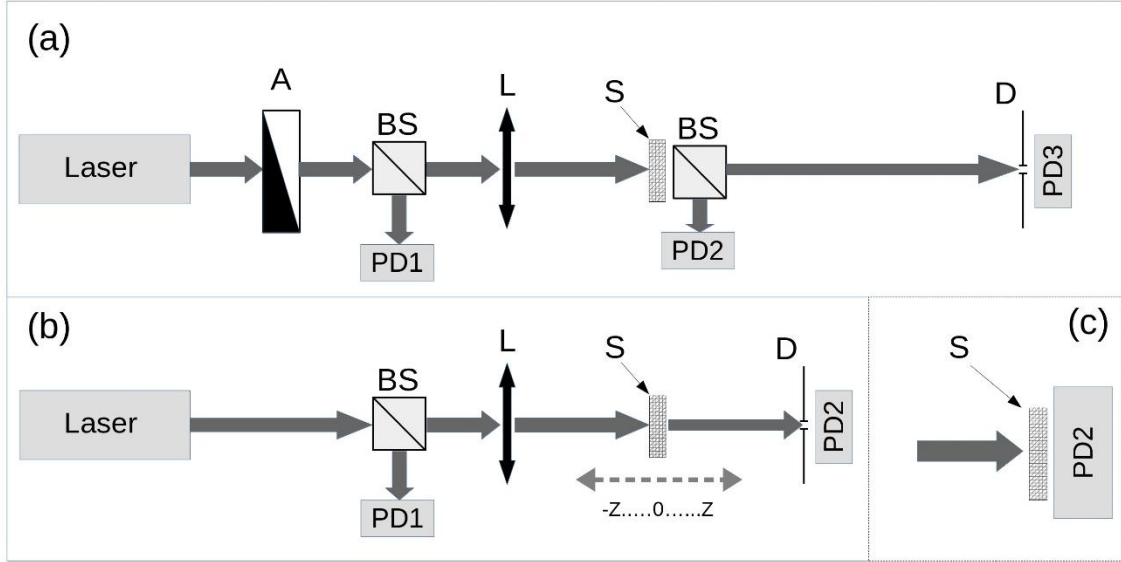


Fig. 2.6 (a) Optical scheme of the experiment for self-action analysis. A – optical attenuator; L – lens; BS – beam splitter; S – sample; D – diaphragm. Photodiodes: PD1 – reference, PD2 – total transmittance, PD3 – on-axis transmittance [87]. (b) is an example of an experimental scheme for Z-scan. (c) - modification of the setup (a) for accurate measurement of the total transmittance through the sample.

Under conditions $n_0 \gg n_2 I$, and $n_0 \gg \alpha \lambda$ we obtain a direct proportionality between the real part of the cubic susceptibility $\text{Re}(\chi^{(3)})$ and n_2 , as well as between the imaginary part of the cubic susceptibility $\text{Im}(\chi^{(3)})$ and β . The following relations for the effect of self-action can be written in esu:

$$\begin{aligned} \text{Im}(\chi^{(3)})[\text{esu}] &= \frac{10^{-14} n_0^2 c \lambda}{19.2 \pi^3} \beta \left[\frac{\text{cm}}{\text{MW}} \right], \\ \text{Re}(\chi^{(3)})[\text{esu}] &= 3 \cdot 10^3 \left(\frac{n_0}{4\pi} \right)^2 n_2 \left[\frac{\text{cm}^2}{\text{MW}} \right]. \end{aligned} \quad (2.14)$$

Experimental technique for measuring of nonlinear optical response due to profile distortion in the far field

Typical technique for the laser beam self-action analysis is Z-scan [86]. We used modification [87] of the standard Z-scan technique, that more effectively allows to determine the parameters of NLO response of the medium when several mechanisms are involved [88]. Its optical scheme is shown in Fig. 2.6a. In contrast to the Z-scan (Fig. 2.6b), the variation in the intensity of the laser beam is realized by changing the optical transmittance of the attenuator A [89–91].

A laser beam with a Gaussian intensity distribution is focused by a lens L on a sample S that is located at a certain distance z from the beam waist. The intensity of the radiation is determined by the coordinate z of the sample and the transmittance of the attenuator A. Combining the change of both parameters allows us to measure the NLO response in a wide range of intensity of excitation.

In the set-up (Fig. 2.6a), three measuring photodiodes are used: the reference photodiode PD1, the photodiode PD2 measuring the power of the incident beam just after the sample, and the photodiode PD3 measuring the power on the beam axis in the far field.

When the attenuator moves, the incident intensity changes. This makes it possible to study the dependence of the nonlinear transmittance coefficient of the sample with the intensity of excitation, that is proportional to the ratio of PD2 / PD1. From the obtained dependence, the NLO absorption coefficient β , that is proportional to the imaginary part of the effective cubic nonlinear susceptibility $\text{Im}(\chi^{(3)})$, can be determined. In this study, the PD2 measuring channel is located close to the sample to prevent any effect due to the change of the refractive index and absorption (or scattering) on total transmittance.

The signal measured by the PD3 photodiode is sensitive to the angular divergence of the laser beam in the far field and, consequently, to the change in the refractive index of the sample [92]. The nonlinear refractive index n_2 is determined by the change in the ratio (PD3 / PD2) vs the intensity of the incident radiation. The NLO refractive index is proportional to the real part of the cubic nonlinear susceptibility $\text{Re}(\chi^{(3)})$.

1) Analysis of total transmittance. The total transmittance of the sample is determined by the formula [93]:

$$T(I_0) = T_{lin} \cdot \ln(1 + q)/q, \quad (2.15)$$

where $q = \beta I_0 L_{eff}$ – dimensional parameter that reflects the nonlinear nature of the absorption process. $L_{eff} = (1 - \exp(-\alpha L))/\alpha$ – effective interaction length, which in the approximation of strong absorption ($\alpha L \ll 1$) is equal to $1/\alpha$, and in the

weak absorption approximation ($\alpha L \gg 1$) is equal to the thickness of the sample L ; T_{lin} - sample transmittance in linear mode: $T_{lin} = 1 - R - A - S$, where R is reflection loss from the surfaces.

In the case of pulsed excitation, the empirical expression for total transmittance has the following form [94]:

$$T(I_0) = \frac{T_{lin} \cdot \ln(1+q) \cdot (1+0.228q)}{q \cdot (1+0.136q)}. \quad (2.16)$$

2) ***On-axis transmittance analysis.*** When a laser beam pass through a NLO sample, there is a change in the angular divergence of the beam due to the change in the refractive index n_2 (same as Δn). In the case $n_2 > 0$, the sample will focus the beam, and vice versa, defocus when $n_2 < 0$.

The analytical expression for on-axis transmittance can be represented as a series in degrees of a nonlinear phase runoff $\Delta\varphi = kn_2 L_{eff} I(r)$:

$$T_a(I_0) = S [1 + C_1 \Delta\varphi(I_0) + C_2 (\Delta\varphi(I_0))^2 + \dots], \quad (2.17)$$

where S and C_m -coefficients that are dependent on the geometry of the experiment and are determined by the formulas [92]:

$$S = 1 - \exp\{-2(r_0 k a)^2 / [4z^2(1 + b^2)]\};$$

$$C_1 = \frac{1}{S} \exp\left(-\frac{4r_0^2(3+b^2)}{a^2(9+b^2)}\right) \sin\left(\frac{8r_0^2 b}{a^2(9+b^2)}\right); \quad (2.18)$$

$$C_2 = \frac{1}{3S} \left\{ \exp\left(-\frac{6r_0^2(5+b^2)}{a^2(25+b^2)}\right) \cos\left(\frac{24r_0^2 b}{a^2(25+b^2)}\right) - \exp\left(-\frac{6r_0^2(1+b^2)}{a^2(9+b^2)}\right) \right\},$$

where r_0 - radius of the diaphragm at PD3, a - beam spot on the sample, $b = -(1 - z/R)/(2z/ka^2)$ - the ratio of the geometric and diffraction defocusing of the beam, R - curvature of wave front on the sample. In the case of a pulsed mode of excitation due to the averaging over the time profile of the pulse, the coefficients C_m multiplied by $(m+1)^{-1/2}$. Parameter S can be represented as transmittance through the diaphragm D for a system without the sample.

2.3.4 Multiphoton microscopy of individual NPs

The interface scanning technique at TH for colloidal suspensions of NPs is an effective tool that allows to quickly analyze new nanomaterials just after their synthesis. It provides an opportunity to evaluate the orientation-averaged effective cubic susceptibility of nanoparticles. However, such ensemble measurements can be complemented by nanoscale nonlinear characterizations using multiphoton microscopy (Fig. 2.7).

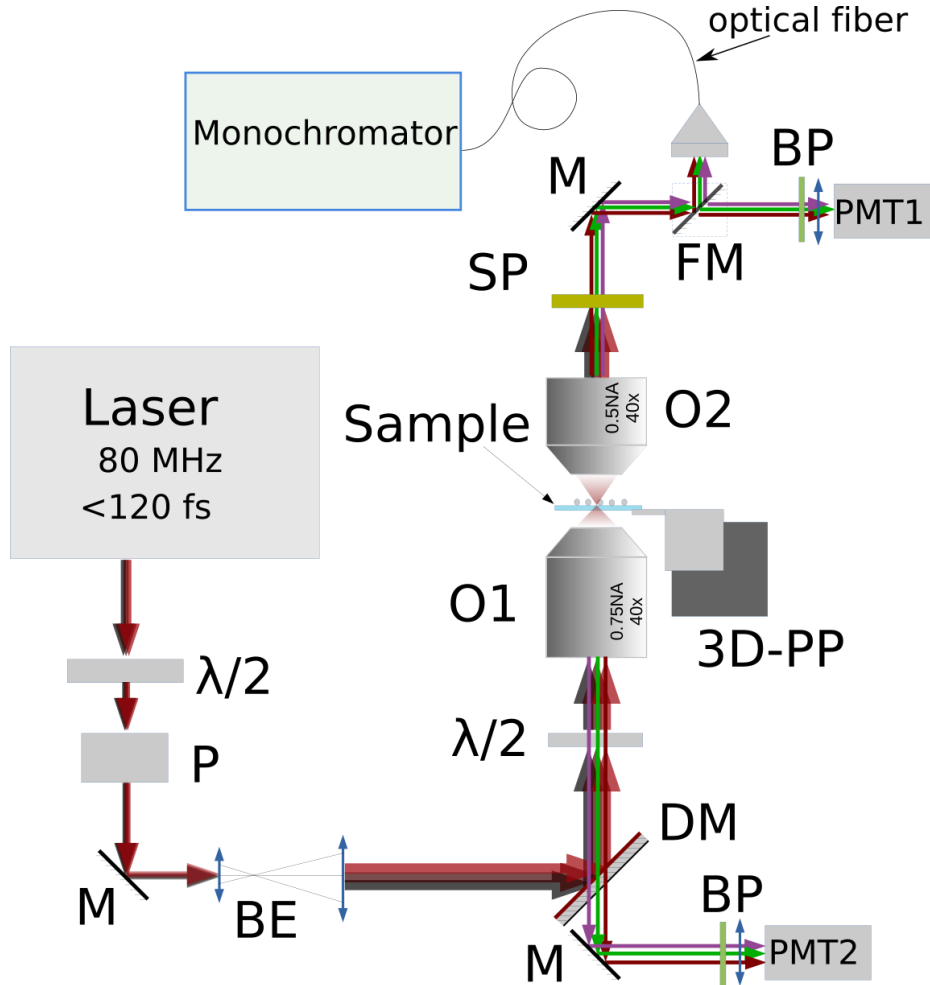


Fig. 2.7 Schematic representation of the experimental setup for multiphoton microscopy. P – polarizer; $\lambda/2$ – half-wave plate; M – mirrors; BE – beam extender; BP – bandpass filters; DM – dichroic mirror; PMT1,2 – photomultipliers; O1,2 – objectives; 3D-PP – 3-axis piezoplateform (working range of 100 μm for three axes, minimum step 0.4 nm); SP – shortpass filter; FM – flipping mirror [95].

With multiphoton microscopy, it is possible to excite individual nanoparticles and readout the signals of the second, third and higher harmonics, as well as luminescence [95]. During this work, I developed a multiphoton

microscopy set-up based on widely tunable (680 to 1300 nm) femtosecond laser (InSight® X3™ Spectra-Physics, repetition rate 80 MHz, pulse duration <120 fs), that has been acquired at the SYMME laboratory.

Typical samples consist of harmonic NPs deposited on a glass substrate by evaporation of a drop from a colloidal suspension. Expanded laser beam is focused on the sample by an objective with a high numerical aperture (Olympus X40, plan Fluor, 0.75NA) and generated signals are collected through a reflective objective (Thorlabs, 40X, 0.50NA) with low transmission losses in a wide range of wavelengths. The sample is located on a three-axis piezoplatfrom (P-616 NanoCube® Nanopositioner) in closed loop control mode, that has a high resolution (~0.4nm) in all translation range (100×100×100μm).

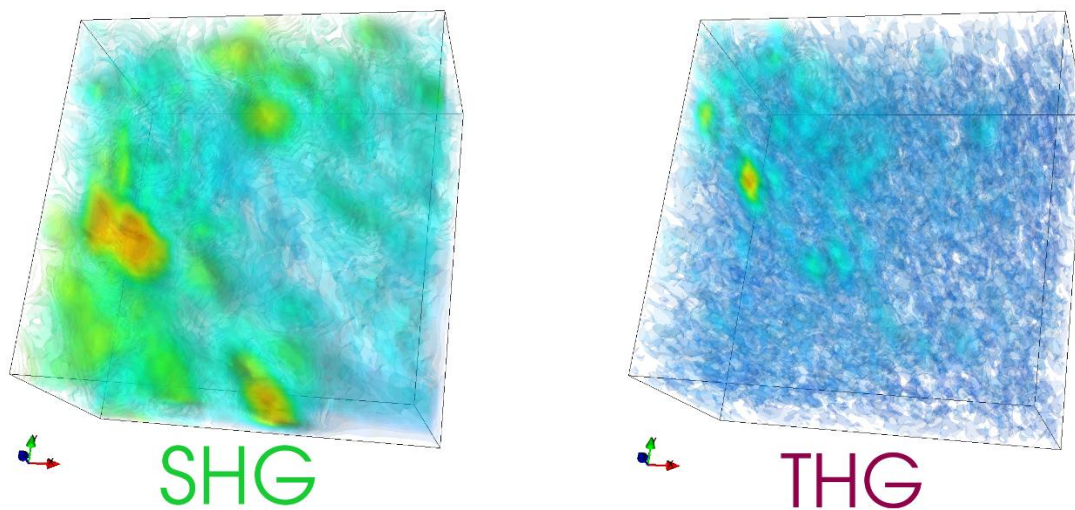


Fig. 2.8 3D reconstruction of SHG and THG signals from KTP microcrystals (~1μm) deposited on the glass substrate. Scanning range 10×10×6 μm².

For fast scanning of large volumes of the sample, Hamamatsu H10721-210 photomultipliers are used, that register signals through bandpass filters in the forward (355nm) and backward directions (532nm). This approach allows to provide a fast readout of SHG and THG signals with pumping at 1064nm and helps to quickly identify NPs on the substrate. It should be noted that at the input of the designed microscope the dichroic mirror DM (see Fig. 3.1) was used. The lower limit of the working range of this mirror is about 710 nm that limiting the pumping range to the 710-1300 nm.

The visualization of the sample is realized by step-by-step translation of the sample relatively to the focused beam waist, harmonic signals readout and reconstruction of the raster images at the wavelengths of SHG and THG. Example of 3D reconstruction for KTiOPO_4 microcrystals deposited on the glass substrate presented on Fig. 2.8.

It should be noted that spatial resolution $\delta_{x,y}$ and depth of focus δ_z in this case depends on the order of nonlinearity N of the process[96]:

$$\delta_{x,y} = \frac{1}{\sqrt{N}} \frac{0.61\lambda}{NA}, \quad \delta_z = \frac{1}{\sqrt{N}} \frac{2n\lambda}{NA^2}, \quad (2.19)$$

where $NA = 0.75$ – numerical aperture of the focusing objective, $n = 1$ – refractive index of immersive medium, $N = 2$ for SHG and $N = 3$ for THG. In this case for pump wavelength range $\lambda = 710 - 1300$ nm theoretical resolution presented in Table 2.1.

It can be seen the resolution of the microscope do not allow to resolve the single NP. However, an additional approach (see chapter 3) based on polarization response analysis can be used to identify single NPs and agglomerates.

Table 2.1 Spatial resolution $\delta_{x,y}$ and depth of focus δ_z of the designed multiphoton microscope for SHG and THG processes (in nm).

NLO effect	$\delta_{x,y}$	δ_z
SHG	408 – 748	1785 – 3268
THG	333– 610	1457 – 2669

For analysis of the spectral response of NPs, a spectrometer (Andor Shamrock 193) coupled to a Peltier-cooled CCD camera (Andor iDus 401) can be used. This allows to reconstruct a raster image of the sample, where for each pixel a full emission spectrum, with potential harmonic and luminescence signals, is recorded. Due to the short laser pulses duration and a high intensity of focused beam $\sim 0.5 \text{ GW/cm}^2$, but with a low energy $\sim 1 \text{ nJ}$, the pulse does not damage the nanoparticles.

The experimental setup allows to realize a high-precision measurements of the excitation spectra in the spectral range of the pump 710 – 1300 nm. A set of scanning optimization algorithms used for long measurements described in chapter 3.

Conclusions to the chapter 2

1) An experimental prototype for analyzing the optical scattering indicatrices under continuous laser excitation in the visible and infrared range was developed. Due to the high dynamic range of eight orders of magnitude, the device has been approved on a wide range of objects: highly absorptive carbon materials and nanostructured "black" silicon, nanoparticles and their colloidal suspensions, crystals and optical ceramics for laser technology [65,97–99]. The main advantages of the designed prototype are:

- (i) automated measurements in the visible and near infrared ranges;
- (ii) wide dynamic range, that is 8 (visible) and 6 (IR) orders of magnitude, due to the use of modern detectors, a set of neutral filters and synchronous detection of the scattered signal;
- (iii) multiple measurement modes: scattering in forward ($|\theta| < 90^\circ$) and backward ($90^\circ < |\theta| \leq 180^\circ$) hemispheres, as well as exact backscattering; high angular resolution - up to 3 angular minutes with registration by a photodetector, and up to 6 angular seconds with registration by the CCD;
- (iv) possibility of reconstruction of the scattering panoramas with high angular resolution for the study of samples with a complicated indicatrix profile.

2) For the first time the interface scanning technique was applied for the third harmonic generation efficiency measurements of HNPs colloidal suspensions. The main advantages of this technique are:

- (i) high sensitivity at low excitation intensities;
- (ii) a robust calibration protocol based on the comparison with the response of well-known quartz glass;
- (iii) monitoring of the reproducibility through the estimation of the cubic susceptibility of the solvent before and after the measurement.

3) The prototype of the multiphoton microscope was designed for studying the response of the individual HNPs under femtosecond laser excitation in pump range 710 – 1300 nm. The detailed sensitivity characterization, applied algorithms and protocols of measurements will be described in chapter 3.

Chapter 3 Nonlinear optical response of ZnO harmonic nanoparticles

Harmonic nanoparticles have shown a high potential for microscopic biological research. The first successful results were obtained for large nanoparticles > 100 nm [11], that effectively generate second harmonic signals. For more accurate identification of nanoparticles response in bioimaging applications, signals from the third, fourth, and higher harmonics are now also being used [100]. More generally, work is also underway to optimize the size of the NPs, to increase the efficiency of the second, third, and higher harmonics generation and to provide a proper surface functionalization for specific applications. To study these new materials, it is necessary to develop a set of techniques that provide a non-destructive and fast characterization of the synthesized NPs. This chapter mainly describes two experimental techniques:

- an interface scanning technique used to analyze the third harmonic generation efficiency of colloidal suspensions, and then to derive the third-order susceptibility of the nanoparticles;
- a multiphoton microscopy technique to study the response of individual NP.

Both experimental techniques will be applied in this chapter to retrieve the nonlinear optical properties of zinc oxide (ZnO) nanoparticles. Among harmonic nanoparticles, ZnO HNPs have attracted much attention for therapeutic and diagnostic purposes, due to their appealing properties and low cost. ZnO is used for various biomedical applications, including delivery of biomolecules (drug, gene, etc.), cancer therapy, angiogenic therapy, antibacterial application, tissue engineering, bioimaging, biosensor, etc. [101,102].

Zinc oxide belongs to wide-bandgap semiconductors with band gap for bulk crystals at $E_g = 3.37$ eV. This material is widely used in optoelectronics [103–107], and nanostructures. In particular quantum dots have been used as radiation sensors, light emitting diodes, etc., and are useful for modern

nanoelectronics. Recently, the possibility of ZnO utilization as a harmonic nanoparticle was demonstrated [23].

3.1 Preparation of ZnO colloidal suspensions

Third Harmonic generation measurements were performed on colloidal suspensions that were obtained starting from commercial ZnO nanopowders, with different mean sizes of nanocrystals: ZnO1 - 90-200 nm (NanoAmor Inc.), ZnO2 - 40-100 nm (NanoTek, Alfa Aesar) and ZnO3 40 nm (NanoAmor Inc). The procedure for the preparation of stable colloidal suspensions was carried out in three stages. At the first stage, the nanopowders were dispersed in a solvent (200 ml) with an initial concentration of ~ 1 mg/ml and treated in an ultrasound bath for about 2 hours. Suspensions were then left to settle for 2 weeks at 18 °C. The supernatant NPs was then separated from the initial suspension.

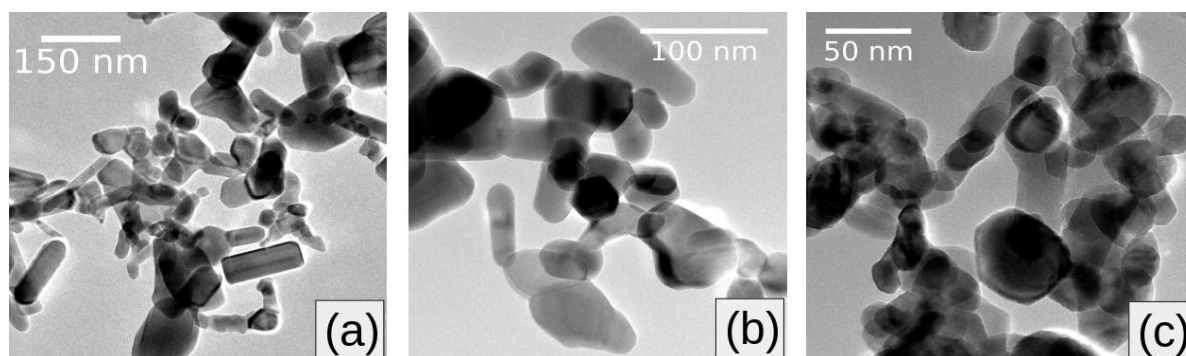


Fig. 3.1 Typical TEM images of (a) ZnO1, (b) ZnO2, (c) ZnO3 in ethanol [77].

This approach allows us to obtain stable suspensions with minimal size of nanoparticles (or their agglomerates in the case of nanopowders with a small size of nanocrystals). The volume fraction or mass concentration was determined by evaporating a known volume of stable suspension and weighing the residual powder. Typical supernatant concentration was around 0.05 mg/ml. The control of the NPs size was carried out through dynamic light scattering (DLS) using the Zetasizer Nano ZS device before each optical measurement (see Table 3.2). TEM images (see Fig. 3.1) of the different samples show a quite high size and shape polydispersity of these commercial nanopowders.

3.2 Averaged third-order susceptibility from the interface scanning technique

Hyper-Rayleigh scattering measurements in perpendicular direction (HRS@SH, see section 2.3) is a well-known technique used to study the second harmonic generation efficiency of harmonic nanoparticles in colloidal suspensions. This simple experimental approach allows us to evaluate the quadratic NLO susceptibility of the NPs by comparing the response from NPs colloidal suspensions with the well-known response from pNA solutions. In the case of third harmonic, this approach requires a well characterized reference material with known third-order susceptibility. To solve this problem, it has been shown [72] that one can use a two steps approach (HRS@TH) to estimate the cubic susceptibility of NPs (see section 2.3). The disadvantages of this method are: (i) some additional parameters like the size of the particles and the fundamental beam intensity must be precisely quantified, which is difficult and reduces the accuracy of the measure; (ii) a higher excitation intensity is needed to get a noticeable THG signal, thus inducing optical damage to the samples.

As an alternative to hyper-Rayleigh scattering, we developed an interface scanning technique (IS@TH) [108]. This method makes it possible to estimate the effective cubic NLO susceptibility of the colloidal suspension $\chi_{col}^{(3)}$ with different concentrations of nanoparticles, which allows then to estimate the orientation-averaged susceptibility of the nanoparticles $\langle \chi_{NPs}^{(3)} \rangle$ and of the solvent $\chi_s^{(3)}$. In this case, the estimated susceptibility of solvent, which is well known from the literature, allows you to control the quality of each measurement.

3.2.1 Drawbacks of the static system

The first measurements were realized with static cuvettes (see Fig. 3.2a) with a wall thickness of 1 mm and an optical path of 3 and 10 mm. The optimal energy of laser pulses, for which there was no damage on the walls of the cuvette, no boiling of the solvent, and no generation of signals with higher order nonlinearities, was less than 20 μJ .

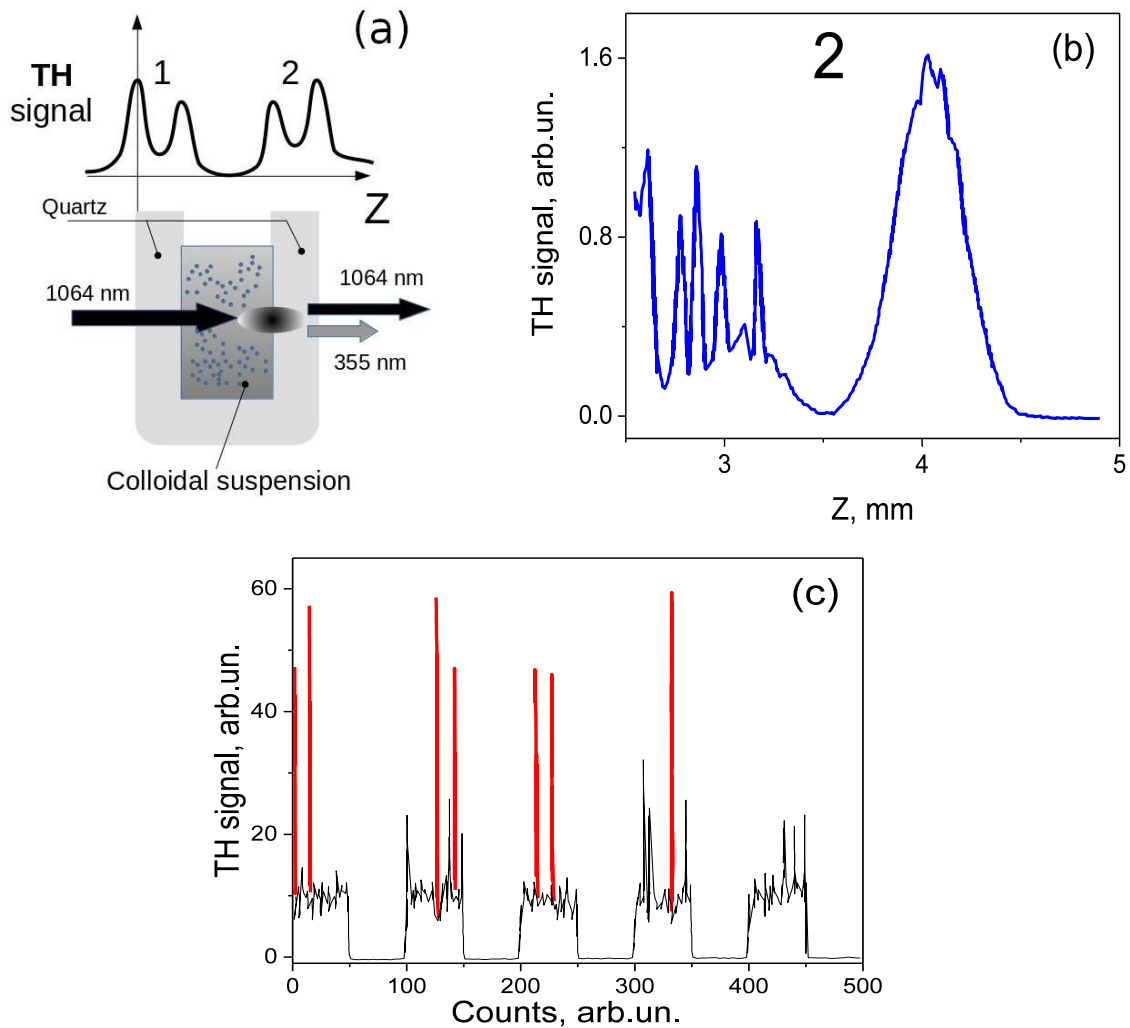


Fig. 3.2 Scanning of a static cuvette with a colloidal suspension of nanoparticles. (a) Schematic representation of the cuvette and response at the interfaces of colloid/quartz and quartz/air of the walls of the cuvette 1 and 2. (b) Scanned with a long averaging time (> 2 s) of the wall 2. (c) THG signal (pump beam modulated by chopper) with spikes that corresponds to the variable number of NPs in the waist and large agglomerates.

For a pulsed excitation mode, one can estimate that the change of the temperature induced by one pulse within the region of beam waist is $T_{\text{peak}} \approx 0.12$ K [109] with a characteristic time for heat dissipation about $\tau_T \approx 0.06$ s. With a high repetitions rate laser, the studied region is warming up, and the temperature gradient may induce some motion of the NPs. We indeed observed an important fluctuation of the THG signal with a static cell (see Fig. 3.2b, c). Moreover, for a small volume of the waist with short-focus lens, i.e., when the number of probed particles does not exceed several hundreds, this effect is significantly increasing. Thus, with nanosecond laser excitation, measurements

with a static cell gives non-reproducible results that depend on the total measurement time (see Fig. 3.2 b,c).

3.2.2 Measurement with colloidal suspension circulation system

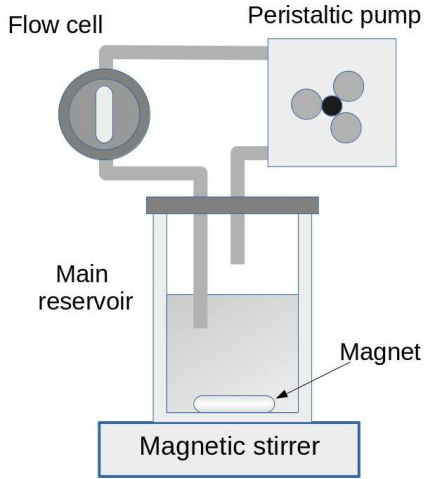


Fig. 3.3 Schematic representation of colloid circulation system.

In order to exclude these reproducibility issues, a specific system with a flow circulation was designed (see Fig. 3.3). The colloidal suspension, placed in a main 50 ml reservoir, is pumped by a peristaltic pump. In the reservoir, colloid is constantly stirred to stabilize the concentration and limit the agglomeration of particles over time.

The suspension passes then through a cell consisting of two UV fused silica walls (5 mm thickness and 2 mm optical path). Using a pumping rate of ~60 ml/min allows to update the volume within the beam waist practically for each laser shot, at 1 kHz repetition rate. As a result, the response of the suspension practically does not vary with time (see below Fig. 3.5) and is much more reproducible.

Table 3.1 Comparison of the results obtained with the literature data $\chi^{(3)}(3\omega = \omega + \omega + \omega)$ for ethanol, methanol, N-BK7.

	$\chi^{(3)}, \cdot 10^{-22} \text{ m}^2/\text{V}^2$	
	Experiment	Reference data
Fused silica		1.99±0.15 [76]
N-BK7	2.63±0.2	2.98±0.15 [76]
Ethanol	2.66±0.2	2.42±0.13 [83]
Methanol	2.25±0.3	1.91±0.10 [110]

$$\chi^{(3)}[\text{m}^2/\text{V}^2] = (4\pi \cdot 10^{-8}/9)\chi^{(3)}[\text{esu}].$$

In order to verify the optical scheme and general approach, the IS@TH method was firstly tested with various solvents with known $\chi_{sol}^{(3)}$, namely, pure methanol or ethanol, and with two cuvettes made of fused silica and N-BK7 for further comparison. The obtained $\chi_{sol}^{(3)}$ values are well consistent with the literature data, as shown in Table 3.1. This confirms the validity of our experimental set-up.

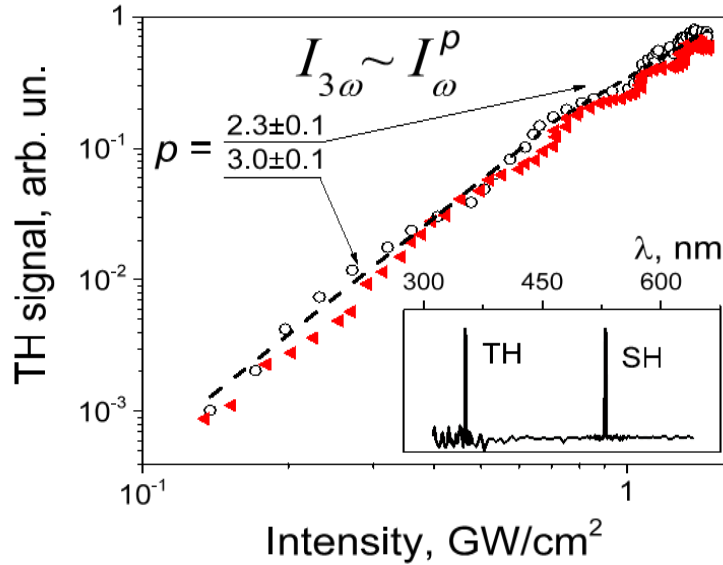


Fig. 3.4 THG intensity at the interface of colloid/glass vs peak intensity under *ns* laser excitation at 1064 nm. (\blacktriangleleft) – ethanol, (\circ)– ZnO colloidal suspension. The inset shows the excitation spectrum at 1064 nm for the colloid/glass interface [108].

3.2.3 Interface scanning technique on ZnO suspensions

Fig. 3.4 shows the dependence of the THG intensity on the interface of colloid/glass vs excitation intensity for ethanol and low-concentrated ZnO in ethanol. It is shown that the THG intensity at the interface has a cubic dependence of $I_{3\omega} \sim (I_{\omega})^3$ in the range up to ~ 1 GW/cm², that is chosen for measurements. At higher excitation intensities, manifestations of higher order nonlinearities are observed, that are more complex to analyze and interpret. To increase the accuracy of the measurements, the scanning was performed for each NPs concentration at three different pumping intensities 0.3, 0.6 and 1 GW/cm².

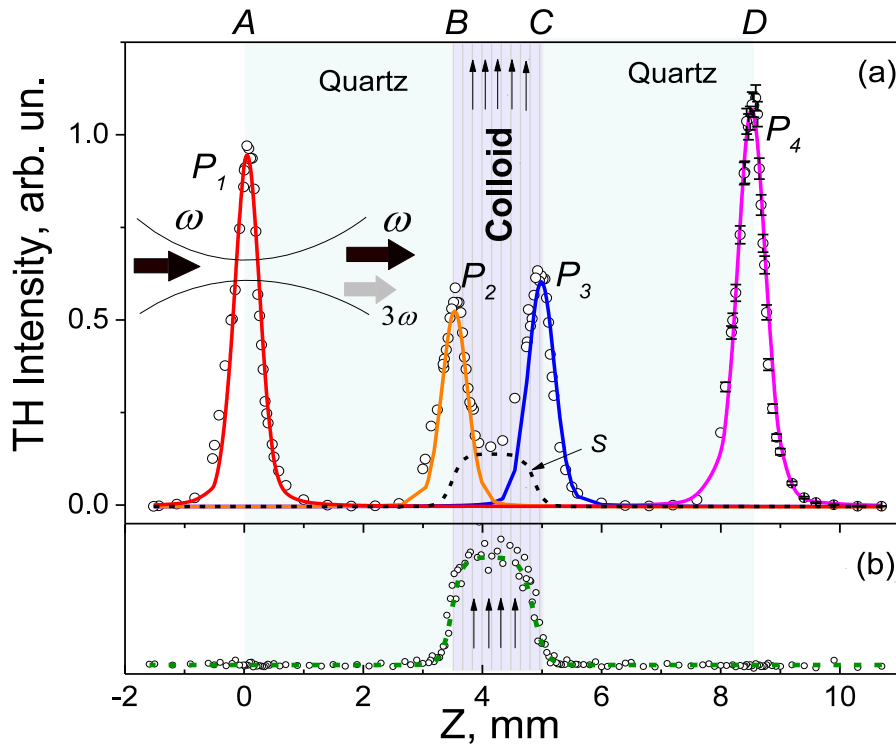


Fig. 3.5 (a) THG scan signal for a colloidal suspension of ZnO NPs with a concentration 1.4×10^{-2} mg/ml in ethanol [77]. (\circ) - experimental data of the TH signal; P_1, P_2, P_3 , and P_4 are the peaks of the TH signal from the interfaces A, B, C, D respectively. S is the plateau of the scattering signal from the volume of the colloidal suspension. Typical errors for 300 laser pulses are presented for peak P_4 . (b) Forward second harmonic signal from a colloidal suspension of harmonic nanoparticles (BiFeO_3) in ethanol for the plateau parameters evaluation from the formula $S(z) = S_{2\omega}(z)^{3/2}$.

An example of a TH signal obtained by scanning the flow cell filled with a ZnO colloidal suspension is presented in Fig. 3.5a. The graph clearly shows the four expected THG peaks at the air/glass, glass/colloid, colloid/glass and glass/air interfaces. Also, in addition to the signals from the interfaces, there is a manifestation of forward Third Harmonic Scattering (THS) from the volume of the colloidal suspension. We can recall here that the main experimental parameter used to derive the effective third-order susceptibility of the colloid is the ratio between the THG at the colloid/glass interface and the THG at the glass/air interface (see eq. 2.5 – 2.11). Unfortunately, the THS signal partially hinders the correct evaluation of the interface THG intensity.

To separate both contributions, the following formula was proposed to fit the measured signal $I(z)$:

$$I(z) = A_0 + P_1(z) + P_2(z) + S(z) + P_3(z) + P_4(z), \quad (3.1)$$

where A_0 – background signal, $P_i(z) = A_i PV(z)$ – pseudo-Voigt distribution function [111], that describes the actual peaks of the THG signal on the i -th interface. The amplitudes A_i are used to estimate cubic susceptibility. The peak width (FWHM) allows to estimate the value of the effective confocal parameter for each interface.

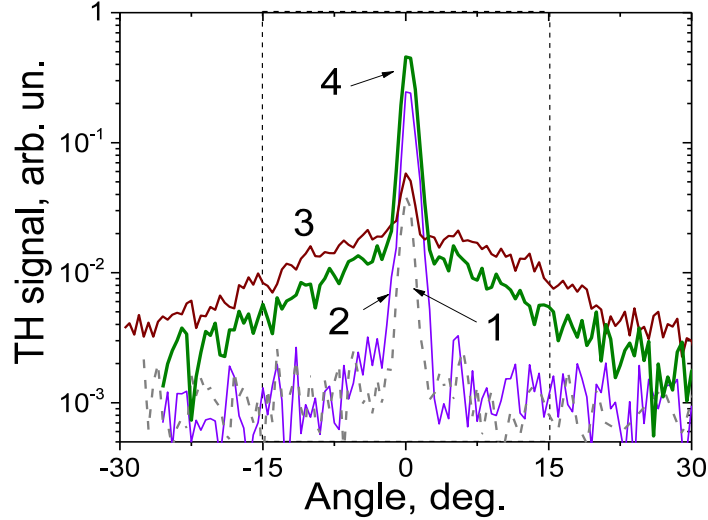


Fig. 3.6 Angular distribution of HRS at TH in forward hemisphere: 1 – scattering from the center of the cell with ethanol (corresponds to the TH peaks overlapping from the interfaces B and C in Fig. 3.4); 2 – scattering from the interface ethanol/glass; 3 – scattering from the center of the cell with ZnO1 colloidal suspension; 4 – scattering from the interface of ZnO1 colloidal suspension and glass. The registration of the signal was carried out through the 1.2 mm diaphragm. The rectangle indicates the area of the signal capture in a standard setup with lens and the photomultiplier without diaphragm.

The following phenomenological expression was used to describe the TH scattering from volume of the cell:

$$S(z) = S_0 \left[1 - \left(1 + \exp\left(\frac{z-\mu_1}{\sigma_1}\right) \right)^{-1} - \left(1 + \exp\left(-\frac{z-\mu_2}{\sigma_2}\right) \right)^{-1} \right], \quad (3.2)$$

where $(\mu_2-\mu_1)$ – forward THS scattering plateau width, σ_i – width of the edge of the plateau, S_0 – amplitude of the THS. It should be noted that determining the exact value of the parameters in $S(z)$ is a very complex task, because at the interface colloid/glass of the plateau $S(z)$ is overlapping with the peak of the signal from the interface $P_i(z)$.

One way to separate the contribution of scattering from the signal at the interface is to measure the indicatrix of the TH signal. Fig. 3.6 shows the angular distribution of the TH intensity for the center of the cell and for the colloid/glass interface. The graph clearly shows that the level of the TH scattering signal (see range $\theta > |5^\circ|$ on curves 3 and 4) is almost two orders of magnitude lower than the peak of the third harmonic signal (see peaks in range $\theta < |5^\circ|$), but it is an order of magnitude higher than the background signal (curves 1 and 2 in range $\theta > |5^\circ|$). Since the changes of the THG signal at the interface usually do not exceed 20% when increasing concentrations of NPs, the contribution of the scattering signal cannot be neglected. This approach (TH scattering indicatrix) gives a lot of information, however, it takes a lot of time for signal averaging and cannot be used without significant optimization.

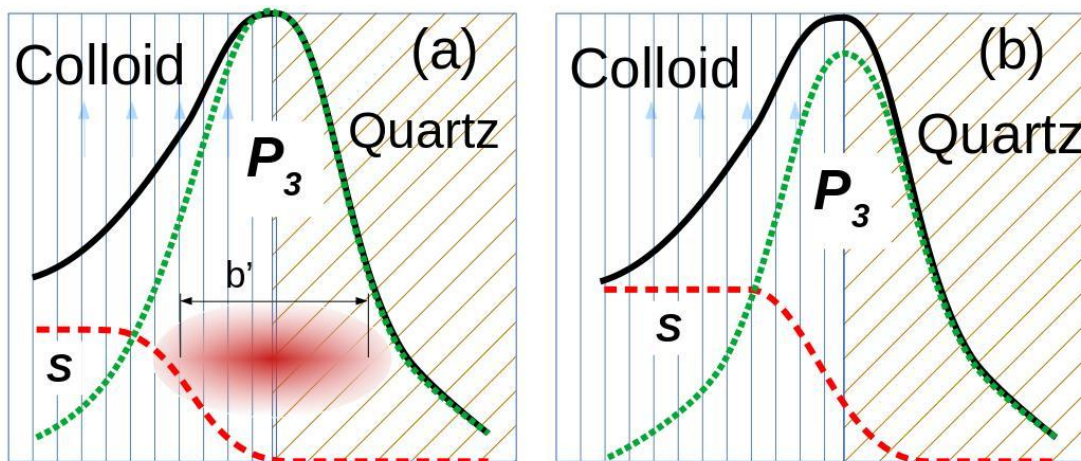


Fig. 3.7 Schematic representation of two extreme cases for analysis of the TH signal on the colloid/glass interface C (a) the dominant contribution to the resulting TH signal (black solid line) is TH from the P_3 interface (green dotted line)[77]. (b) both contributions (TH scattering from the volume and signal from the interface) exist: the parameters of the scattering plateau $S(z)$ (red dashed line) are estimated from the SH scattering signal measurements (see Fig. 3.5b).

Another approach is based on the modeling of the $S(z)$ plateau scattering, that depends only on the size of the beam waist and the distance between the walls (see Fig. 3.7). In this case, its parameters μ_i and σ_i can be estimated by the following tip. The cell with colloidal suspension was also scanned using an interference filter at 532 nm in front of the detector (see Fig. 3.5b). In that case,

the second harmonic scattering signal from the volume of colloid is dominant and depends on the geometry of the system. From approximation of the $S_{2\omega}(z)$ signal profile, we can estimate μ_i and σ_i and use them as fixed values in the $I(z)$ approximation (see Eq. 3.1).

This approach however has some limitations, and we then assume two limiting cases to derive the third-order susceptibility of NPs (i) the contribution of the TH scattering to the THG signal at the interface is simply neglected (Fig. 3.7a) (ii) TH scattering profile is evaluated from the second harmonic measurement as previously explained (Fig. 3.7b). The application of both approaches allows us to estimate a range of $\langle \chi_{NPs}^{(3)} \rangle$ values.

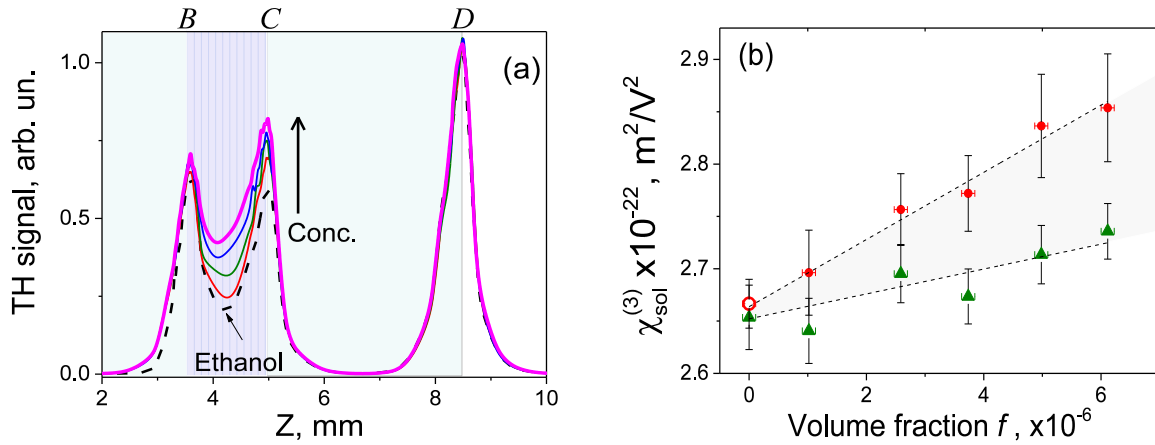


Fig. 3.8 (a) Example of TH scan signal variation with increasing NPs concentration for a ZnO1 sample in ethanol. The concentration range from 0 (ethanol) to 2.8×10^{-2} mg/ml. (b) Estimated effective cubic susceptibilities $\chi_{sol+NPs}^{(3)}$ obtained by two data fitting approaches: (●) dominant contribution of THG from the interface (see Fig. 3.7a), (▲) - joint contribution of THS from volume and THG from the interface (see Fig. 3.7b). (○) - verification measurement for ethanol after concentration measurements [77].

An example of TH scans for different ZnO1/ethanol based colloids with concentrations ranging from 0 to 2.8×10^{-2} mg/ml is shown in Fig. 3.8a. The asymmetric amplitude of the signals from the internal cell interfaces B and D is due to the linear extinction at TH wavelength. To minimize this effect, only signals from interfaces C and D are used in the analysis.

For each concentration of nanoparticles, measurements were made at

three excitation intensities. Also, each point of the curve was corrected by the corresponding value of the signal from the reference silicon photodiode [108], in order to minimize the effect of the laser power oscillation.

The obtained TH signals ratio at the *C/D* interfaces was then used to calculate the effective cubic susceptibility of the colloidal suspension $\chi_{sol+NPs}^{(3)}$ using equation (3.5). The linear increase of $\chi_{sol+NPs}^{(3)}$ with the volume fraction f is showed in Fig. 3.8b and corresponds to the expected trend given by the nanocomposite effective susceptibility model:

$$\chi_{sol+NPs}^{(3)} = f \left(\frac{3\epsilon_{sol}^{3\omega}}{\epsilon_{NPs}^{3\omega} + 2\epsilon_{sol}^{3\omega}} \right) \left(\frac{3\epsilon_{sol}^{\omega}}{\epsilon_{NPs}^{\omega} + 2\epsilon_{sol}^{\omega}} \right) \chi_{NPs}^{(3)} + \chi_{sol}^{(3)}. \quad (3.3)$$

To check the reproducibility of the results, each time a control measurement was carried out: after several cycles of measurements with increasing NPs concentration, the colloidal suspension was removed from the circulation system and the main reservoir was filled with ethanol. The correct ethanol third-order susceptibility value was measured again (Fig. 3.8b), indicating that there is no influence of sticking of the NPs on the glass after long-duration measurements.

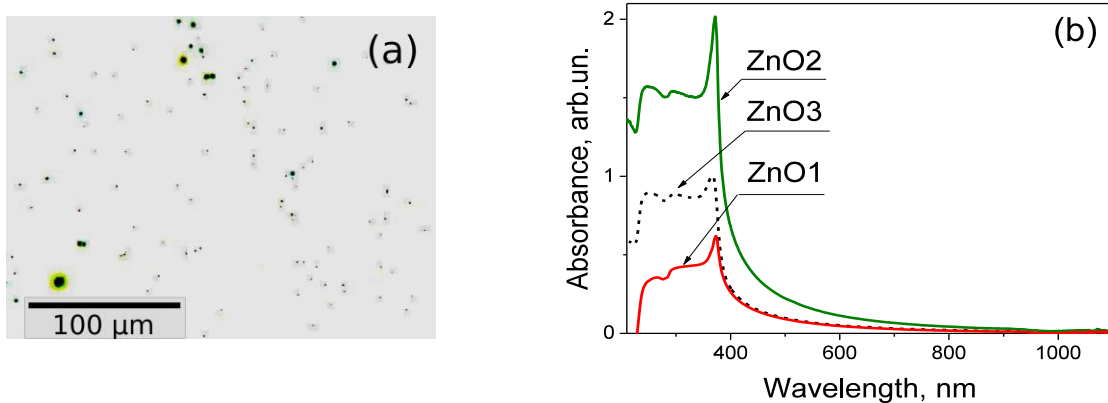


Fig. 3.9 (a) Optical image of internal surface of the flow cell after prolonged pumping of colloidal suspension. (b) Absorption spectra for ZnO nanoparticles with different sizes in ethanol.

This potential drawback was also studied by imaging the cell walls in dark field mode (see Fig. 3.9). This image was obtained after 30 minutes of pumping with a concentrated colloidal suspension of ZnO nanoparticles through the cell. In this picture it is clearly seen some nanoparticle islands on the surface,

but the average distance between them is less than the diameter of the waist. The duration of the real measurements with set of concentrations did not exceed 15 minutes, and at the end of each measurement, the cell was re-scanned with a corresponding solvent to verify the reproducibility of the response.

Table 3.2 Comparison of orientation-averaged cubic susceptibility for ZnO NPs with different sizes, obtained by HRS@TH and IS@TH experimental techniques [77].

Sample	Solvent	$D_{(TEM)}$, nm	D_n , nm	$\langle \chi_{NPS}^{(3)} \rangle$, $10^{-18} \text{ m}^2/\text{V}^2$		$\langle \chi_{NPS}^{(2)} \rangle$, pm/V
				IS@TH*	HRS@TH	HRS@SH
ZnO1	Ethanol	145	143	$(1.4-4.3) \pm 0.3$	1.3 ± 0.7	6.0 ± 1.0
ZnO2		100	137	$(1.3-3.7) \pm 0.4$	1.9 ± 0.8	5.8 ± 0.9
ZnO3		40	110	$(0.6-2.1) \pm 0.3$	0.9 ± 0.4	2.4 ± 0.4
ZnO1M	Methanol	145	136	2.1 ± 0.4	-	-
ZnO2M		100	127	1.0 ± 0.2	-	-
ZnO3M		40	141	2.0 ± 0.5	-	-

$D_{(TEM)}$ –NPs size, obtained from TEM images, D_n - size, estimated by DLS; * range of $\langle \chi_{NPS}^{(3)} \rangle$ corresponds to the two fitting approaches described in text.

The approximation of the linear dependencies of $\chi_{sol+NPS}^{(3)}$ vs the volume fraction f of nanoparticles using equation (3.3) allows us estimate the value of the effective orientation-averaged susceptibility $\langle \chi_{NPS}^{(3)} \rangle$ for individual nanoparticles. The obtained values for the different samples of ZnO nanoparticles in ethanol are shown in Table 3.2. This approach was also used for methanol based colloidal suspensions. However, the concentration of stable suspensions in this solvent is almost an order of magnitude smaller, so the estimation of cubic susceptibility for these samples was only carried out according to the assumption presented in Fig. 3.6a. The results obtained for this series of methanol based colloids are presented here to demonstrate the independence of the IS@TH technique from the type of solvent.

We found high values of ZnO cubic susceptibility, which are in good agreement with the reference data $\chi^{(3)} = 3.5 \cdot 10^{-18} \text{m}^2/\text{V}^2$ for bulk ZnO [112] and with the values obtained by HRS@TH. Indeed, this former method has also been used for the same set of ZnO samples (see reference [77] for experimental details) and the measured susceptibilities also lie in the $10^{-18} \text{m}^2/\text{V}^2$ range. However, as developed in Ref. [77], a direct comparison between the two experimental $\langle \chi_{NPS}^{(3)} \rangle$ values obtained from HRS@TH and IS@TH experiments is not fully pertinent because both of them are averaging the different component $\chi_{ijkl}^{(3)}$ of the third-order susceptibility tensor due to the specifics of the experiment geometries.

The high measured ZnO third order susceptibility value can be attributed to a resonant interaction, the TH wavelength being in the absorption band as seen from the extinction spectra (Fig. 3.9) and it will be confirmed by nonlinear spectroscopy on individual particles with multiphoton microscopy in the next section.

To summarize, the main advantages of the implemented interface scanning technique are:

- 1) it allows estimate the absolute magnitude of cubic NLO susceptibility using well characterized fused silica windows as reference material;
- 2) the circulation system for colloidal suspension was designed to minimize effects of agglomeration/sedimentation in order to obtain stable NPs concentration with optimized flow rate to readout the THG signal from a new set of NPs per each laser shot;
- 3) reproducibility of the measurement for the solvent before and after experiment with NPs colloidal suspension and comparison with the reference data provides correct calibration and monitoring of the potential NPs sticking effect;
- 4) THG efficiency at the interfaces in forward direction is higher in comparison to the HRS@TH that allows to apply lower pump intensities and prevent the

damage of HNPs in colloidal suspensions;

5) for HRS@TH, the intensity in the area of the waist should be precisely measured. It should be noted that the average NPs size, obtained from the data of dynamic light scattering, must also be known for HRS@TH. However, this method has a benefit as the HRS intensity increase is proportional to the NPs concentration.

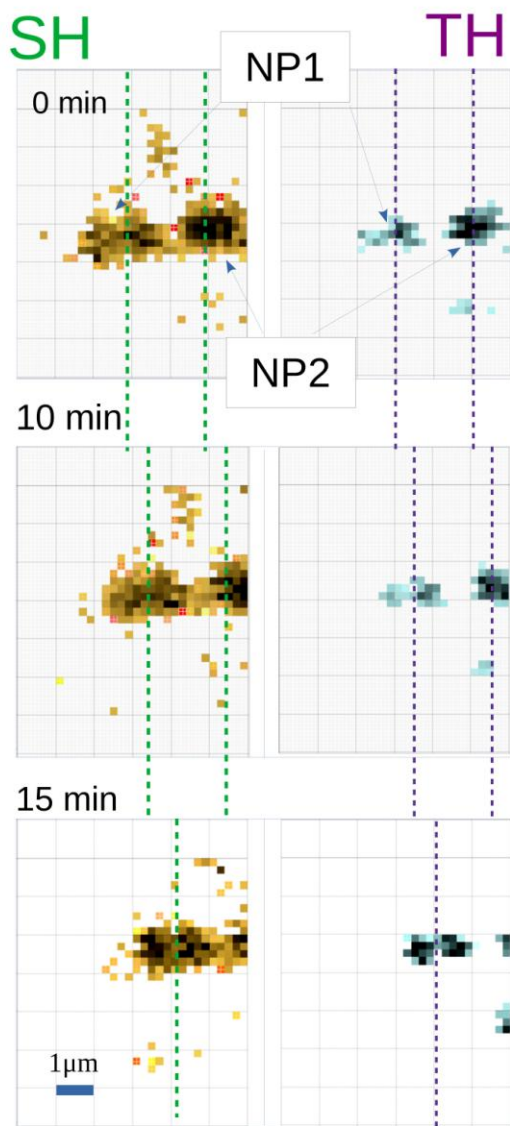


Fig. 3.10 Thermal drift of the set of NPs: 2D scan after 0, 10 and 15 min. Left frames – SHG. Right frames – THG. Frame size $10 \times 10 \mu\text{m}^2$.

3.3. Multiphoton microscopy of single ZnO nanoparticles

The IS@TH and HRS@TH for colloidal suspension of HNPs are effective tools for analysis of the macroscopic response of ensembles of NPs that allow to analyze new nanomaterials immediately after their synthesis stage.

Multiphoton microscopy allows to analyze the microscopic NLO response at the single NP scale, by readout the signals of the second, third and higher harmonics, as well as luminescence. This is a very promising spectroscopy tool; however, it was firstly designed for bioimaging tasks where readout is realized by fast photodetectors with fixed set of bandpass filters for a

specific type of response. In order to realize nonlinear spectroscopy of a single HNP, where pumping and response readout should be realized in a wide wavelength ranges, we used a high sensitive CCD camera for the signal readout

and a tunable *fs* laser (710 – 1300 nm) for the excitation.

During the microscope development phase, we quickly encountered two experimental issues. Firstly, as we do not use galvanometric mirrors but a 3-axis piezoplatfrom to scan the sample, we had to develop a fast-readout mode to get a reasonable acquisition time for individual NPs localization task. This was solved by using visualization saw called “on fly” mode that will be described in the next section. Secondly, we observed an important drift of the images, related to the temperature fluctuation in the laboratory (within 3 °C). In that conditions, the drift is in the range of ~ 1µm (see Fig. 3.10) for long measurements (~ 1 hour), due to thermal expansion of the mechanical parts of the microscope and the piezoplatfrom. Stabilization of the temperature to the range of 1 °C allows to decrease the “thermal drift” at about 300 nm/h. However, for long-duration measurements (for multiple NPs with pump wavelengths range 710 – 1300 nm for instance), this factor is still critical and was solved by developing a special acquisition algorithm (see section 2.4.2)

3.3.1 Visualization “on fly”

In multiphoton microscope, an image is realized by a step-by-step translation of the sample (or beam scanning with galvanometric mirrors) and response readout from the volume of the beam waist. Typical frame acquisition time with photomultipliers and bandpass filters for an area of 100×100 µm² with 1µm resolution can reach tens of minutes.

Practically, an important initial procedure when starting measurements, is the localization of individual NPs on the substrate. Indeed, typical samples for microscopy are obtained by drying a drop of a low concentrated NPs suspension onto a glass substrate. At the end, the sample consists of different areas with agglomerated and dispersed NPs. Selecting the optimal area for the observation can take a long time. For example, re-scanning the area and incremental increasing of the resolution can sometimes take up to 30 minutes. This approach cannot be accepted due to the always possible thermal drift of the frame.

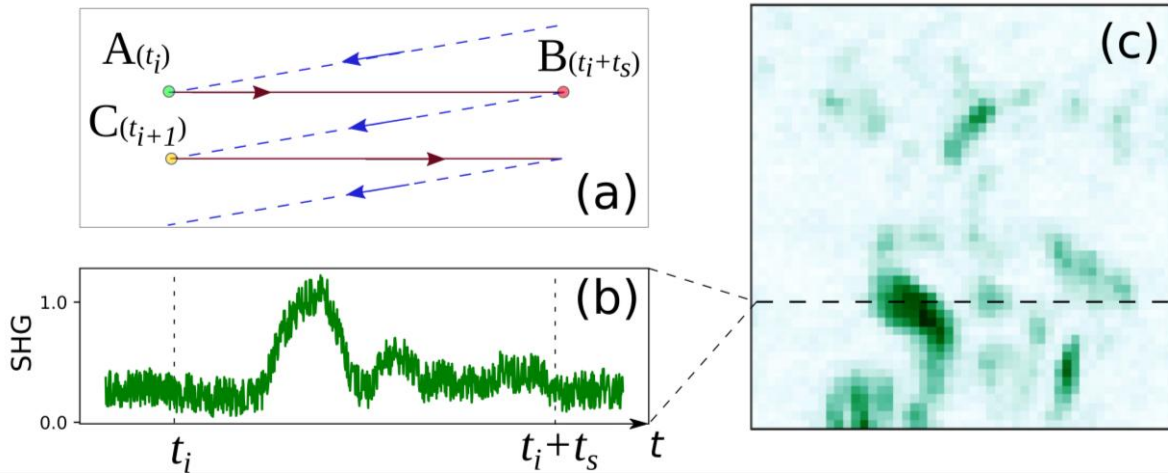


Fig. 3.11 (a) Schematic representation of the visualization by "on fly" procedure. (b) SHG signal of the single stage of the procedure. (c) Reconstructed image SHG signal from KTiOPO₄ HNPs . Scanning area $50 \times 50 \mu\text{m}^2$ with resolution $1 \mu\text{m}$.

To solve this problem, the procedure of visualization "on fly" was developed (see Fig. 3.11). It is based on the principle of simultaneous mechanical translation and signal readout (in contrary to the step by step process). In this algorithm, the translation is realized by a zigzag path from point A to point B (see Fig. 3.11a) with parallel acquisition of the signal and recording the timestamps for each data sample. If translation from point A started at t_i and finished after scanning time t_s at point B at $t_i + t_s$, the captured signal (see Fig. 3.11b) can be cropped to selected time range and resized by downsampling with averaging to the required resolution. Data processing is realized due to the translation from point B to the initial point C of the next row. This procedure allows decrease the scanning time from minutes to seconds with acceptable reproducibility.

Theoretical acquisition time for a scanning area $100 \times 100 \mu\text{m}$ and a spatial resolution $1 \mu\text{m}$ with this method is about 30 s with averaging of about 2.7×10^5 shots per $1 \mu\text{m}$ range. However, it requires advanced synchronization of the translation stage and the acquisition hardware that are not implemented in the present algorithm. Typical capturing time for the same area and resolution with the current technique is about 1 minute, that about 10 times faster than a step-by-step approach. It should be noted that the efficiency of the

reconstruction is decreasing for areas smaller than $10 \times 10 \mu\text{m}$ due to the variable acceleration and closed loop position optimization of the translation stage for small scales. However, in practice, even in this case the resulting image is efficient enough to select the optimal scanning area. Next steps are realized by step-by-step approach for higher precision.

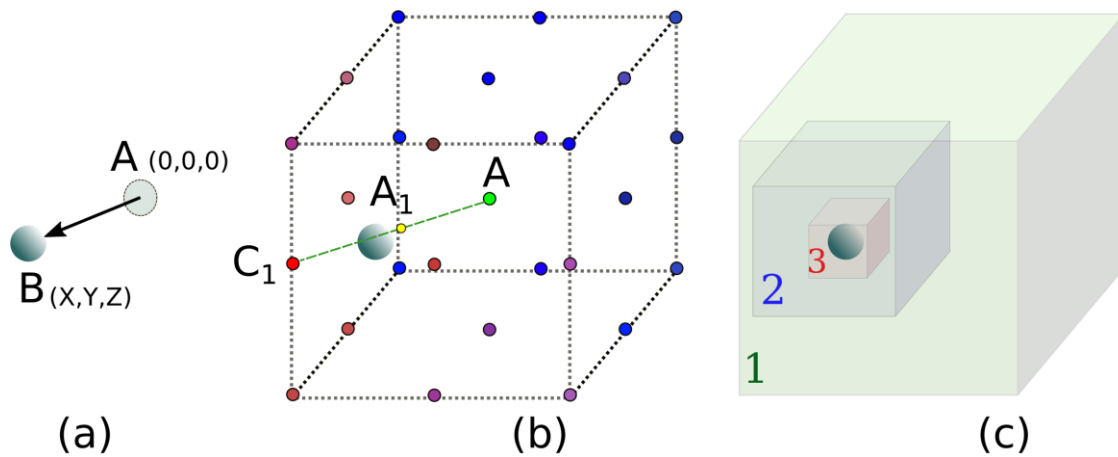


Fig. 3.12 (a-c) Stages of the "thermal drift" effect compensation algorithm for long-duration measurements.

3.3.2 Coordinate system optimization with tracking of nanoparticles

To improve the stability of the measurements which is limited by thermal drift, an algorithm for optimizing the frame coordinate system was implemented (see Fig. 3.12). It is based on the determination of the coordinates of one bright nanoparticle, which serves as an anchor (point **A** in Fig. 3.12 a). If the position of the anchor NP shifted from point **A**(0,0,0) to point **B**(x,y,z) next recursive procedure of 3D search can be applied [113,114]. At the first stage of the algorithm, a distribution of the signal intensity is measuring at each point of the grid around initial point **A** with low exposure for speed up the search. A point **C**₁ (see Fig. 3.12 b) with a highest magnitude of the signal is used to define a temporary coordinate system shift direction.

New temporary coordinate system will be positioned at the midpoint **A**₁ of **AC**₁. On the next stage the size of the scanning grid is divided by 2 and the same search is repeated (see Fig. 3.12 c) until the one half of the spatial resolution at current wavelength is reached. At the end of the iteration the center

of the coordinate system is shifting to the last defined maximum of the signal. Exposure level is automatically adjusted when each point of scanning grid has a signal lower than a threshold level. Periodic scanning of the position of anchor NP during a measurement and correction of the zero position for the whole coordinate system allows to significantly increase the precision and reproducibility of measured response.

Maintenance of a stable temperature in the laboratory and active optimization of the frame coordinate system can significantly improve the accuracy of measurements and it allows to realize an analysis in whole excitation range (710 – 1300 nm), that usually takes from 1 to 2 hours.

3.3.3 Polarization response of single nanoparticle

The next step after “anchoring” the frame and determination of the NPs coordinates is to analyze the polarization response for each NP, by changing the polarization of the pump beam. Indeed, it is not always possible to distinguish individual NPs from small agglomerates due to the diffraction limited resolution of the microscope. Polarization measurement allows to identify individual NP (or group of NPs with the same orientation) by comparison with theoretical response (see Fig. 3.13). In case of the agglomerate the intensity of the signal can be high but it does not depend on the input polarization.

The resulting polarization response of each particle is then analyzed to determine the optimum excitation polarization for a particular NP. In the next steps, this information is used to optimize the polarization for each particular particle.

3.3.2 Spectral response corrections

The multiphoton microscope setup, described in chapter 2, is based on a tunable *fs* laser and includes multiple optical elements such as objectives and lenses, shortpass and long range bandpass filters, optical fiber, etc. Due to the complexity of the system, a proper correction of the sensitivity should be provided.

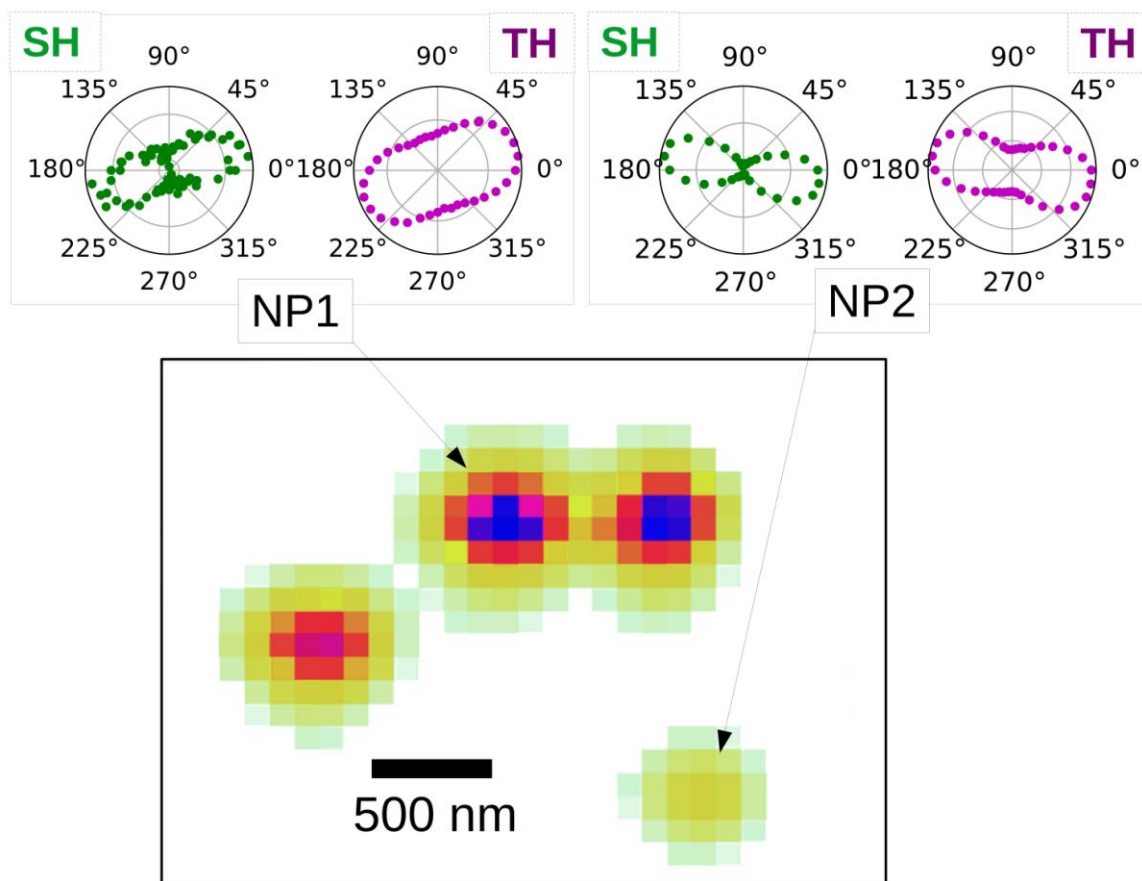


Fig. 3.13 Polarization response of separate ZnO1 NPs (NP2) and aggregates (NP1) with different orientation on glass substrate.

For this purpose, the global sensitivity was estimated by using the following procedure (see Fig. 3.14). At the first stage, the transmittance spectra from an optical diffuser positioned in the working area of the microscope and illuminated by a tungsten halogen lamp with continuous spectra was measured. At the second stage, the transmittance spectrum was measured for the same diffuser positioned in front of the spectrometer. It was illuminated by the lamp at some angle in order to avoid a saturation of the CCD. The resulting correction curve obtained by dividing this two spectra is shown in Fig. 3.14a., together with the spectral sensitivity of the CCD camera. Normalizing the spectral response of the experiment by using these two curves provides a correct representation of the signal magnitude at specific wavelength.

Also important is the correction of the input intensity variations with wavelength. Firstly, variation of the input power vs pump wavelength was measured by a power meter positioned in front of the input objective at a

distance 5 mm from the waist in order to avoid damage of the sensor and collect all the signal. Then, it should be noted that laser beam radius is also slightly varying vs wavelength. It means that excitation intensity is also wavelength-dependent even if the input power is controlled. In order to compensate this effect, an interface scanning of a bulk crystal (see similar approach in section 2.2) was measured for each pumping wavelength. Fitting the THG peak from the interface allows to estimate the spectral dispersion of the waist parameters (see Fig. 3.14b) and thus, the peak intensity of the laser beam.

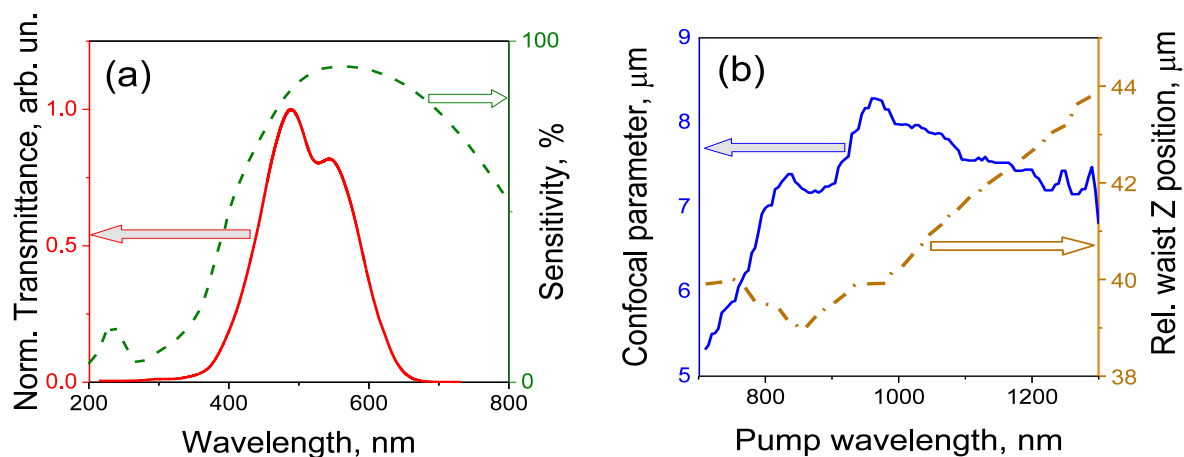


Fig. 3.14 (a) CCD camera spectral sensitivity (dashed curve) and optical system transmittance compensation curve (solid). (b) Confocal parameter (FWHM) (solid line) and waist position variation (dashed line) vs pumping wavelength.

3.3.4 Spectral response of single nanoparticle

After determining the coordinates of nanoparticles and their polarization response, nonlinear spectroscopy of single NPs can be performed. It consists of the measurement of the different emission spectra while shifting the pump wavelengths from 710 to 1300 nm. For ZnO with a band gap of ~ 3.4 eV, such a wide pumping range allows us to study the effect of resonance enhancement of the second and third harmonics generation efficiency by involving real energy levels to the process of harmonics generation.

Fig. 3.15 shows typical emission spectra at different pumping wavelengths for a ZnO1. The spectra clearly show two characteristic peaks corresponding to the second and third harmonics, as well as a two-photon excited luminescence peak at 378 nm when excitation wavelength is below 1000

nm.

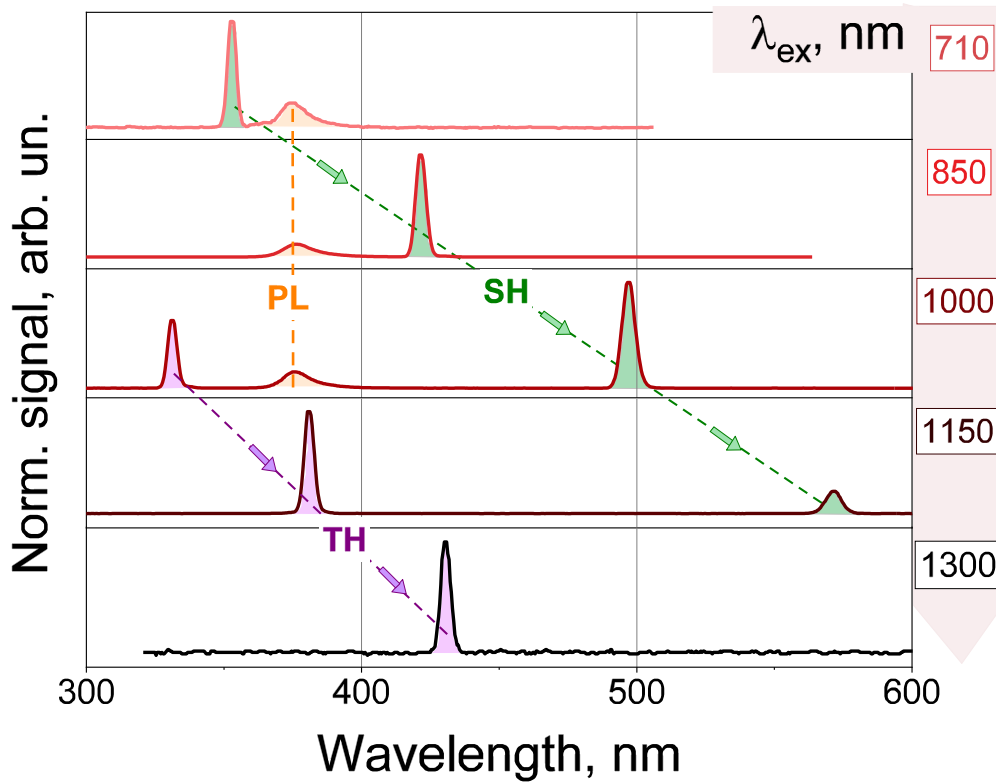


Fig. 3.15 Spectral response of ZnO1 HNP under different excitation wavelengths λ_{ex} .

The spectra in Fig. 3.15 clearly demonstrate the tuning of the harmonic NPs response: variation of the pump wavelength leads to a shifting of the spectral narrow harmonic peaks, while the wide luminescence signal stays at the same wavelength. This makes it possible to clearly identify the harmonic NPs in biological tissues.

By integrating the corresponding peaks and calibrating the signal levels taking into account the correction of the microscope spectral sensitivity (see previous section), one can obtain dependencies of the harmonics generation efficiency and luminescence vs the pump wavelength.

Fig. 3.16 shows the normalized signals of the second and third harmonics, as well as the luminescence peak (~ 378 nm) vs the pump wavelength for a ZnO1 sample. It should be noted that the peaks of the second and third harmonics are shifting, when the wavelength of the excitation changes, because the process of harmonic generation is realized through virtual levels. In the case

of PL, the peak remains at the same wavelength because the radiation always comes from specific real energy states.

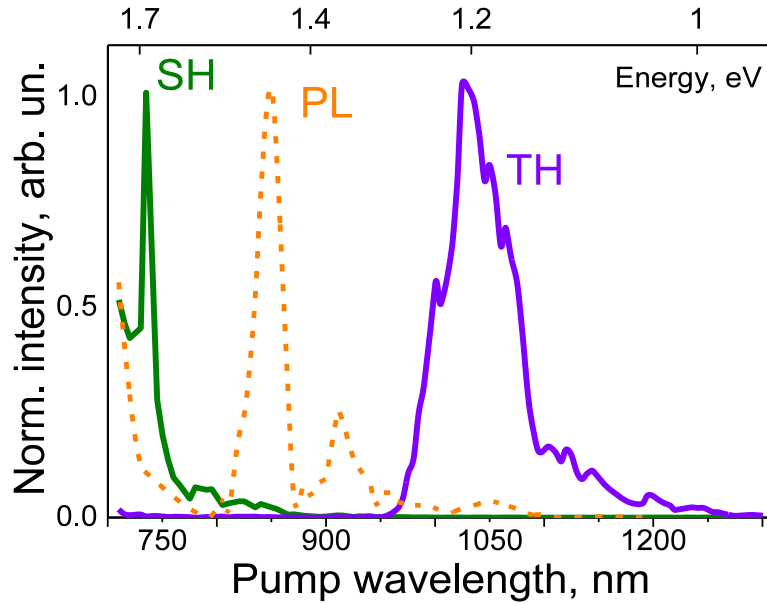


Fig. 3.16 Normalized second and third harmonic signals and PL at about 378 nm vs pump wavelength.

The position of the peaks on excitation spectra are 735 nm for SH ($\lambda_{2\omega}=367$ nm), 850 nm for PL and 1025 nm for TH ($\lambda_{3\omega}=342$ nm). For the second and third harmonics, these values are consistent with the exciton resonance near the bandgap[115,116], and are also close to the wavelength of maximum of absorption (see Fig. 3.9b). Peak of PL corresponds to efficient two-photon excited luminescence from shallow traps (see Fig. 4.12). The obtained data demonstrate the effect of a resonance enhancement of the harmonic generation efficiency by involving real defects states. One can note that this specific second harmonic response for ZnO nanoparticles was also observed from ensemble measurements using a wavelength-tunable second harmonic scattering experimental setup [117].

Also, these data confirm the results of the analysis of colloidal suspensions under *ns* excitation at 1064 nm using the interface scanning technique as described in the previous section. Indeed, the detected resonance at 1025 nm is close to 1064 nm and this explains why such high ZnO third-order susceptibility has been measured.

Conclusions to the chapter 3

1) For the first time an interface scanning technique, being primarily designed to study nonlinear response of liquids and gases, was applied for the third harmonic generation efficiency analysis of HNPs colloidal suspensions,

2) This technique was applied to analyze the third harmonic generation efficiency of ZnO HNPs colloidal suspensions with nanosecond pulsed laser excitation at 1064 nm. The validity of the technique was verified by comparison of solvent nonlinear experimental response with reference data. The non-degenerate orientation-averaged cubic nonlinear optical susceptibility of the ZnO NPs with sizes in range 40–150 nm has been estimated at about $\langle |\chi_{NPs}^{(3)}(3\omega = \omega + \omega + \omega)| \rangle \sim 10^{-18} \text{ m}^2/\text{V}^2$.

3) The excitation spectra of the second and third optical harmonics and the photoluminescence of individual ZnO NPs was studied by multiphoton microscopy under *fs* laser excitation in the spectral range $\lambda_{\text{ex}} = 710\text{--}1300 \text{ nm}$. For ZnO NPs with a size $<150 \text{ nm}$ it was shown specific excitation ranges with high efficiency for the different processes: $\lambda_{\text{ex}} < 800 \text{ nm}$ for SH, $800 < \lambda_{\text{ex}} < 950 \text{ nm}$ for PL, and $950 < \lambda_{\text{ex}} < 1200 \text{ nm}$ for TH. Excitation of the ZnO HNPs in one of these ranges allows to work mainly with one type of response and to improve the accuracy of the identification of NPs in biological tissues.

Chapter 4 Characterization of different types of ZnO based nanostructures and bulk crystals

In this chapter, we present linear and nonlinear optical characterizations of ZnO based nanostructures and bulk crystals. We first focus on the response of very small ZnO nanoparticles, prepared by a wet chemical route. The response from ZnO/ ZnO raspberry like nanostructures (prepared using the previous small NPs) is then presented and finally, the one from ZnO bulk crystals. This chapter is focused on searching of the correlation between the linear and nonlinear optical properties and the defects structure of bulk crystal obtained from very precise and complementary observations that were found very useful for the interpretation of the experimental results.

4.1 Studied materials

4.1.1 Small ZnO NPs

A set of small ZnO NPs has been prepared by our colleagues from Taras Shevchenko National University of Kyiv. To obtain small ZnO NPs [118], a wet chemical method was developed that is based on the stabilization of ZnO by Triethanolamine (TEA) in the presence of small amounts of a hydrolytic agent and an excess of hydrolytic dissociation of zinc acetate (ZnAc_2). Excess zinc acetate plays the role of a stabilizing agent, restricting the growth of large oxide nanoparticles. A set of samples was prepared using different absolute solvents: acetonitrile (MeCN), ethanol (EtOH), isopropyl alcohol (*i*-PrOH) and propylene glycol (PPG).

Consistent with previous studies [107,119–121], it was observed that the core of ZnO was stabilized with TEA in absolute (*abs.*) solvents, *i*-PrOH, EtOH, PPG, and acetonitrile (MeCN), at the early stages of ZnAc_2 hydrolysis. The high concentration of ZnAc_2 together with TEA leads to the growth of ZnO NPs. Protecting ZnO NPs core with adsorbates together with increasing solution viscosity is sufficient to prevent the NPs from the coagulation.

A study using transmission electron microscopy (TEM) was done. The obtained TEM images are shown in Fig. 4.1. One can see that the NPs size is ~ 2 nm that correlate to the estimated from the spectroscopy data (see Table 4.1).

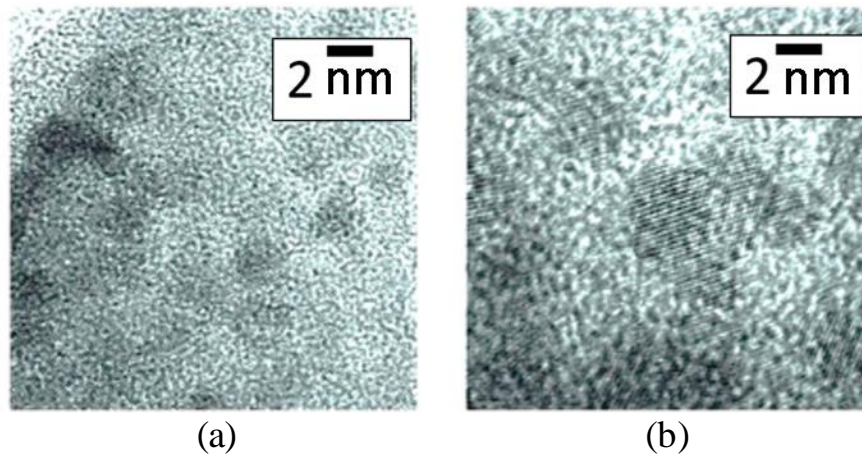


Fig. 4.1 TEM images of solid precipitates obtained from colloids of ZnO NPs in (a) EtOH and (b) *i*-PrOH.

4.1.2 ZnO/ ZnO raspberry-like nanoparticles

Raspberry-like nanoparticles were synthesized to study the effect of ZnO nanocrystal surface functionalization on the efficiency of the optical harmonics generation (see Fig. 4.2). As raw materials the nanopowder of ZnO1 samples with size (~ 150 nm) studied in the previous chapter was used. The surface of large ZnO1 NPs was functionalized by small ZnO NPs (<10 nm). Functionalization of the surface of NPs at the first stage was realized by hydrolysis in the presence of TEA. Obtained result of hydrolysis was infiltrated with the ZnAc₂/EtOH solution and treated at 1-3 atm with the vapor of N,N-Diethylaniline (PhNEt₂). The technique provides the interface between large and small NPs. It should be noted that small NPs have a crystalline structure due to the application of high pressures and temperatures during the synthesis process.

4.1.3 Bulk ZnO crystal with different concentration of defects

In order to analyze the response of ZnO NPs, so-called “green” ZnO single crystals with a high content of intrinsic defects [122,123] were studied. Among the ZnO crystals in the mentioned papers, we selected two samples, being denoted as ZnO-II and ZnO-III. Their neutron diffraction (ND) patterns

were indexed based on hexagonal unit cells in the space group of high $P6_3mc$ symmetry. However, both patterns exhibit extra diffraction peaks indicating that these crystals have atoms ordered other than stated [123]. The presence of such peaks was also detected by X-ray diffraction taken from micro-fragments and powdered single crystals [122].

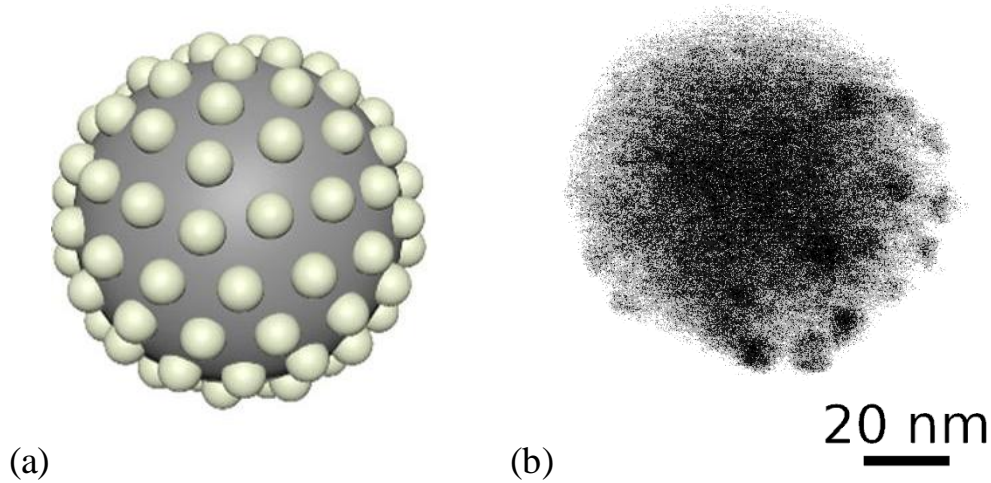


Fig. 4.2 (a) Schematic representation and, (b) TEM images of large raspberry-like ZnO NPs functionalized by small ZnO NPs (<10nm).

In general, these peaks contain information about the lowering of the crystal symmetry. The crystals have similar structures derived from the ND data, namely, both have zinc and oxygen vacancies in the same positions. We suggested that the obtained results for the single crystals with close stoichiometry and similarity of the structural features provide a basis for future studies of the impact of the vacancy types and their content on the various kind of the optical response including the NLO one.

According to [123], the indexing of extra peaks could be done in a lower symmetry Laue group of $P3$. Based on the coexistence of two phases, ND analysis revealed that the content of the low symmetric phase was 15.45% and 16.12% in the crystals of ZnO-II and ZnO-III, correspondingly. Based on this refinement, it was suggested on the formation of a "bulk defect" [123]. From the crystallographic point of view, the origin of the "bulk defect" formation in the wurtzite crystal structure can be an ordering of vacancies and interstitial atoms.

This ordering can include doubly charged zinc V_{Zn} and neutral oxygen V_O vacancies, but interstitials should be zinc atoms Zn_i only.

On this background, it will be reasonable to consider modern vision on the crystal growth and the defects genesis. Study on the crystal growth of ultrafine ZnO has shown that neighboring V_{Zn} and V_O vacancies can appear simultaneously [124]. They remain in a close vicinity of each other at the growth stage. Separate $V_{Zn}-V_O$ pairs can agglomerate into a defect-like $(V_{Zn})_m-(V_O)_n$ ($m \approx n$) complex during annealing at moderate temperatures [125] with the formation of nanoscale voids [126,127]. Coalescence of two open volume defects with a similar size reduces the energy of the system. The open volume enlargement provides voids showing a high stability even at temperatures above 300 °C [128,129]. Presence of the defect-like $(V_{Zn})_m-(V_O)_n$ complex, even for small values of $m = 1$ and $n = 1, 2$, can induce the local lattice relaxation [130] with the formation of Zn_i species. It was shown experimentally for the irradiated ZnO that displaced Zn atoms ($< 0.1 \text{ \AA}$) can be the source of Zn_i [131]. Their appearance has caused a drastic drop in the resistance down by seven orders of magnitude.

Concerning the crystals under study, the refined composition of the ZnO-II and ZnO-III crystals is close derived from the performed ND analysis [123]. The reported structural formula of the ZnO-II crystal is $[(Zn(1)_{0.438} \square_{0.062})(Zn(2)_{0.500})][(O(1)_{0.500})(O(2)_{0.440} \square_{0.060})]$ and that of the ZnO-III crystal is $[(Zn(1)_{0.452} \square_{0.048})(Zn(2)_{0.500})][(O(1)_{0.500})(O(2)_{0.449} \square_{0.051})]$. In both solved crystal structures, the zinc and oxygen vacancies are in Zn(1) and O(2) positions. It was shown that the ZnO-II crystal has the highest content of all zinc and oxygen vacancies. As shown in [123], the refined compositions correlate with interatomic distances. For both crystals, the concentration of oxygen vacancies is in the negative correlation with the bond length of Zn–O(2). The significant shortage of such bonds, 1.970 Å (ZnO-II) against 1.982 Å (ZnO-III), was found with a growth of the oxygen vacancies number. It indicates on a

rising of the virtual transitions contribution into enhancement NLO refractive response of the ZnO-II in transparency range [132].

4.2 Influence of the synthesized ZnO nanoparticles size on the nonlinear optical response

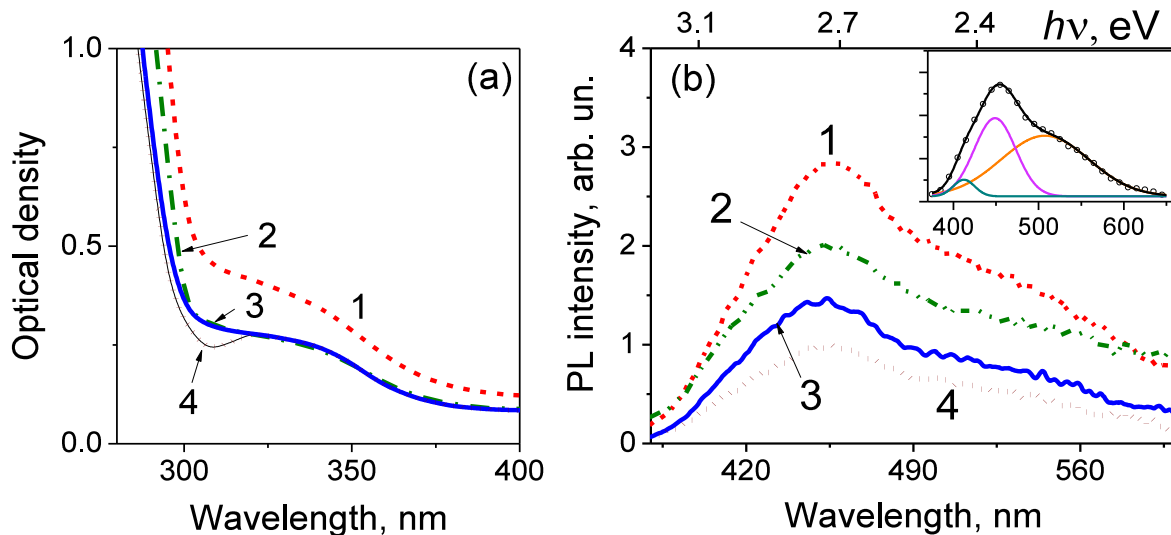


Fig. 4.3 (a) UV-Vis of ZnO NPs in different solvents: EtOH (1), i-PrOH (2), MeCN (3), PPG (4); (b) PL spectrum of ZnO NPs in different solvents; insert demonstrates the PL spectra deconvolution for ZnO NPs in EtOH [118].

This section deals with very small ZnO NPs prepared through the wet chemical method. Fig. 4.3a shows UV-Vis spectra of the resulted ZnO NPs in different solvents. Typically, ZnO NPs size reduction causes an overall UV absorbance decrease and a broadening of the exciton-related peak at 360–370 nm [133]. In the presented spectra, we observe smoothed adsorption peaks with a reduced uniform absorption over the UV range and a blue spectral shift to ~330–350 nm. According to an approximation in [134], this characteristics can be attributed to the presence of spherical particles with average diameter D of ~1.5–2.0 nm range. The impact of the different viscosity of the solutions could be a reason of the observed dispersion in the D values. Also, one should take into account that the absolute quantity of water is different in the used *abs.* solvents.

The ZnO NPs were also analyzed by excitation-emission spectrofluorimetry technique. PL spectra of ZnO NP in different solvents show a

broad emission ranging from 400 to 600 nm with an emphasis in the violet-blue range, Fig. 4.3b. The PL spectra were deconvoluted into Gaussian peaks at about

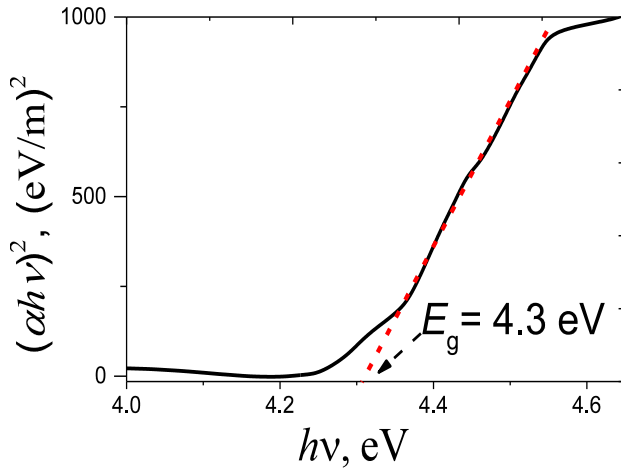


Fig. 4.4 Tauc plot of $(ahv)^2$ versus photon energy hv for residual ZnO NPs in abs. EtOH solution.

2.3 eV, 2.8 eV, and 3.0 eV (539, 443 and 413 nm respectively). PL properties of ZnO, in general, are very sensitive to defects. The most probable explanation of observed PL spectra is the presence of many energy levels. Typically, these levels originate from various defects, including vacancies and interstitials.

The high intensity of the PL emission (see Fig. 4.3b) indicates a high density of extended defects in ZnO structure. This fact once again indicates a non-equilibrium character of the NPs formation process.

Optical density spectra (see Fig. 4.3a) were interpreted using an empirical equation for the average particle radius in nm [134]:

$$r = \left(0.3049 - \left(-26.23012 + \frac{10240.72}{\lambda} \right)^{1/2} \right) \left(6.3829 - \frac{2483.2}{\lambda} \right)^{-1}, \quad (4.1)$$

where λ corresponds to the peak position.

The optical band gap energy (E_g) was estimated from Tauc plots [135] (Fig. 4.4). To estimate the band gap shift with the NP size one can use the cluster size equation from Jortner's work [136]. In the case of ZnO NPs, we used the modified form of the equation proposed in [137]:

$$E_g = 3.35 + 100 \cdot (18.1 \cdot d^2 + 41.4 \cdot d - 0.8)^{-1}. \quad (4.2)$$

The NLO response of solid precipitates, obtained from *i*-PrOH, EtOH, and MeCN, were studied within the self-action of picosecond laser pulses (42 ps FWHM, repetition rate 15 Hz) at 1064 nm [87,98]. The precipitates were placed into the bed with $\varnothing \sim 8$ mm in the Teflon® film positioned between two glass

microscope slides (Marienfeld, 76×26×1 mm³). The film thickness $d = 340 \mu\text{m}$ was chosen to provide optical homogeneity in the solid sample layer and sufficient transparency for the registration transmittance level. This approach is described in details for the carbon material bulk particles NLO diagnostics [138].

Table 4.1 Optical band gap energy (E_g), estimated diameter of NPs, total transmittance (T_0), real and imaginary parts of the cubic degenerate NLO susceptibility $\chi^{(3)}(\omega = \omega + \omega - \omega)$ [118].

Solvent	E_g , eV	d , nm	NLO parameters		
			T_0 , %	$\text{Re}(\chi^{(3)})$, $\times 10^{-9}$ esu	$\text{Im}(\chi^{(3)})$, $\times 10^{-11}$ esu
EtOH	4.3	~1.5–2.0	1.7	2.4	1.4
<i>i</i> -PrOH	4.1		1.0	−4.2	0.7
MeCN	4.5		0.2	2.9	0.5
ZnO1	3.4	<150	40.5	−7.1	0.4

It should be noted that the NLO characterization of the ZnO NPs precipitates was done at the wavelength 1064 nm (1.17 eV). The laser quanta 1.17 eV can induce resonant two-photon absorption transitions into the V_O band with a peak at about ~2.4 eV. The precise peak position and the area obtained from the Gaussian decomposition of the PL spectra are presented in Table 4.1.

Fig. 4.5a presents the photoinduced variations of the total transmittance of the solid precipitates, obtained from *i*-PrOH, EtOH, MeCN, and HD. The total transmittance variation in the studied peak intensity range is rather low. At the initial $I \leq 2 \text{ MW/cm}^2$ range, the total transmittance is approx. constant (T_0) that corresponds to the linear regime of the optical transmittance. The T_0 magnitude significantly depends on the solvent, see Table 4.1. In the range of used solvents, the magnitude reduces in following order $\text{EtOH} > i\text{-PrOH} > \text{MeCN}$. To derive the photoinduced effects manifestation from the linear response background, we normalized the obtained dependencies (Fig. 4.5a) with the

linear transmittance T_0 . The results are shown in Fig. 4.5b as smoothed curves with the relative error of about $\pm 0.2\%$ [138].

Analysis of the presented data reveals non-monotonic photoinduced total transmittance variations in the samples. For the peak intensity range $> 100 \text{ MW/cm}^2$, the efficient photodarkening for all studied samples can be attributed to the two-photon resonant excitation of the V_O oxygen vacancies. For this range, from the obtained dependencies, the imaginary part of the cubic NLO susceptibility $\text{Im}(\chi^{(3)})$ was estimated within the approach described in [19]. The results are presented in Table 4.1. One can see the $\text{Im}(\chi^{(3)})$ magnitudes decrease in the following order $\text{EtOH} > i\text{-PrOH} > \text{MeCN}$.

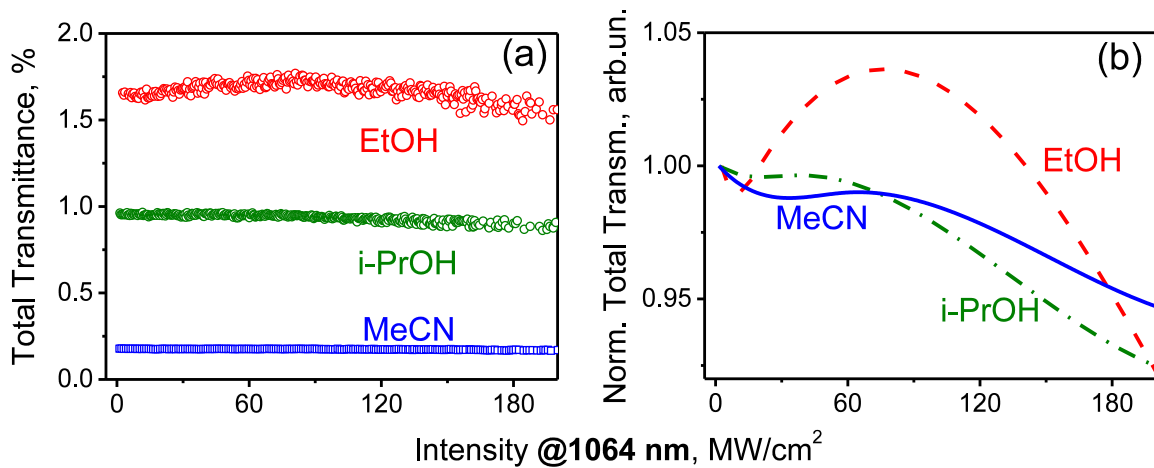


Fig. 4.5 The photoinduced variations of the total transmittance due to the self-action of the picosecond laser pulses at 1064 nm for the ZnO NPs precipitates, obtained from different solvents: (a) the total transmittance versus the peak laser intensity; (b) the same smoothed total transmittance dependencies that were normalized on T_0 (see Table 4.1) – the transmittance in a linear regime [118].

The on-axis transmittance dependencies reveal the different sign of the refractive NLO response for the ZnO NPs precipitates, obtained from different solvents (see Fig. 4.6). A photoinduced self-focusing effect was observed for MeCN and EtOH while a self-defocusing one – for $i\text{-PrOH}$. From the obtained dependencies, the real part of the cubic NLO susceptibility $\text{Re}(\chi^{(3)})$ was estimated [138]. The observed $\text{Re}(\chi^{(3)})$ positive magnitudes for the ZnO NPs precipitates, obtained from MeCN and EtOH can be explained by the two-photon resonant excitation of the oxygen vacancies. The two quanta energy 2.33 eV does not exceed the V_O band spectral position (see Table 4.1) that determines

the positive refractive NLO response of the trapped carriers [139]. Here, a more efficient refractive response of ZnO NPs in MeCN is attributed to better overlapping of the V_O band position with the two-photon laser quanta energy.

The manifestation of the self-defocusing effect ($\text{Re}(\chi^{(3)}) < 0$) for the ZnO NPs precipitate obtained from *i*-PrOH solutions requires more detailed study.

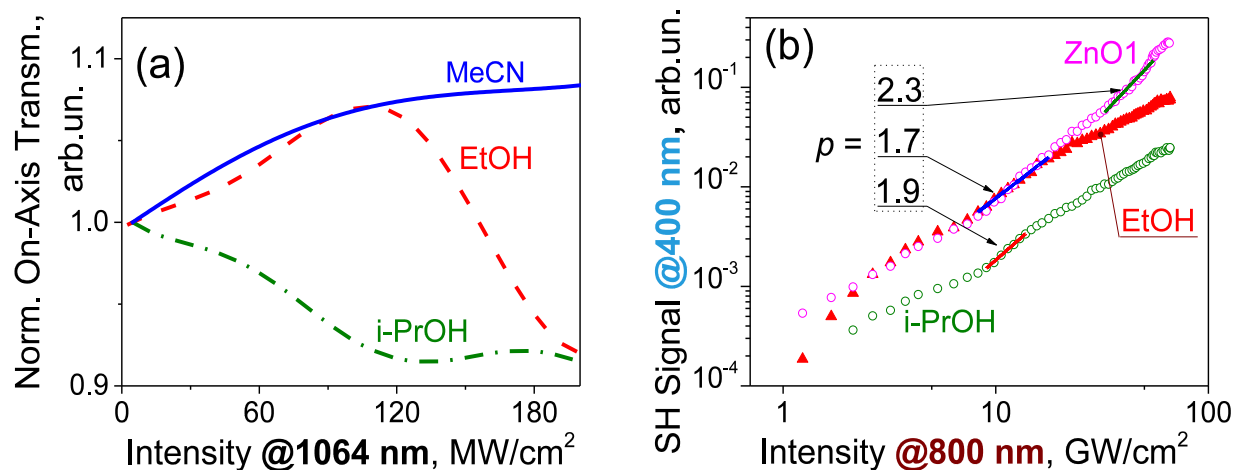


Fig. 4.6 (a) The photoinduced variations of the on-axis transmittance due to the self-action of *ps* laser pulses at 1064 nm for the ZnO NPs precipitates, obtained from different solvents; (b) The SHG signal in ZnO NPs solutions and colloidal suspension (commercial bulk ZnO) versus the peak intensity of the pump *fs* laser pulses at 800 nm.

The measurements of the SHG signal in the ZnO NPs suspensions were performed within the excitation of femtosecond laser pulses (200 *fs* FWHM, repetition rate 1 kHz) at 800 nm. The scheme of the experimental setup is similar to the HRS measurements described in chapters 2 and 3. The samples were positioned at a distance of 14.5 cm from the focusing lens with a focal length of 11 cm. The scattered second harmonic (SH) signals readout was realized at 90° from the laser beam axis by Atik 16IC CCD camera. In order to cut the fundamental radiation and extract SH signal, bandpass (BP, 405 nm, 10 nm FWHM) filter was positioned in front of the CCD camera. The energy of the incident pump pulses was measured by a photodiode.

Measurements were done for ZnO NPs in EtOH and *i*-PrOH and the results were compared with a colloidal suspension of large ZnO NPs in EtOH (based on ZnO1 samples studied in chapter 3). For this last-mentioned sample,

the average particle size is about 100 nm and for such large NPs, the HRS signal is known to be proportional to the square of the NP volume and to the NPs concentration (see eq. 2.3). Here, the SH signal dependencies are presented in Fig. 4.6b in a log–log scale.

In order to compare the results, we analyzed the SHG intensity in different excitation ranges. The effective order p of the NLO response $I_{2\omega} \sim (I_{\omega})^p$ was then estimated. At peak intensity range 10–13 GW/cm², a maximal $p = 1.9$ was obtained for the *i*-PrOH solution containing ZnO NPs. The synthesized in EtOH and large ZnO NPs demonstrated a lower $p = 1.7$. For $I_{\omega} > 15$ GW/cm², we have observed a higher slope for the larger NPs with $p = 2.3$. It can be explained by a macroscopic cubic NLO response of the suspension and a similar effect was observed in KDP single crystals with incorporated TiO₂ NPs [56].

It should be noted that all the samples were prepared with the same initial concentration and were placed in an ultrasonic bath before measurements. However, it is not possible to monitor agglomeration and/ or sedimentation that can lead to variation of the NPs concentration, so a direct comparison of the absolute SHG intensity between the samples is not easy. Nevertheless, the SHG signal from the small (~2 nm) ZnO NPs is close to the one from the large NPs and this probably demonstrates a higher efficiency than the one theoretically predicted by eq 2.3. For very small NPs, the surface SHG contribution is not anymore negligible.

In order to increase this surface contribution, we designed a specific raspberry-like nanostructure which will be presented in the next section.

4.3 Multiphoton microscopy of raspberry-like ZnO NPs

Analogically to the approach used in chapter 3, it was studied the efficiency of optical harmonics generating from individual ZnO NPs (90–200nm) with surface functionalized by small ZnO NPs (<10nm) (see paragraph 4.1.2), using the multiphoton microscopy.

For that, signals from functionalized particles were normalized by the

response of raw NPs. Fig. 4.7 shows this normalized response which was calculated by averaging the measurements of 10 NPs with optimized input polarization (see chapter 3). It should be noted that due to the unknown individual size of each probed NPs, it is not possible to directly compare the absolute intensities. However, the relative ratio can be used to describe some efficiency modification within a specific pumping range.

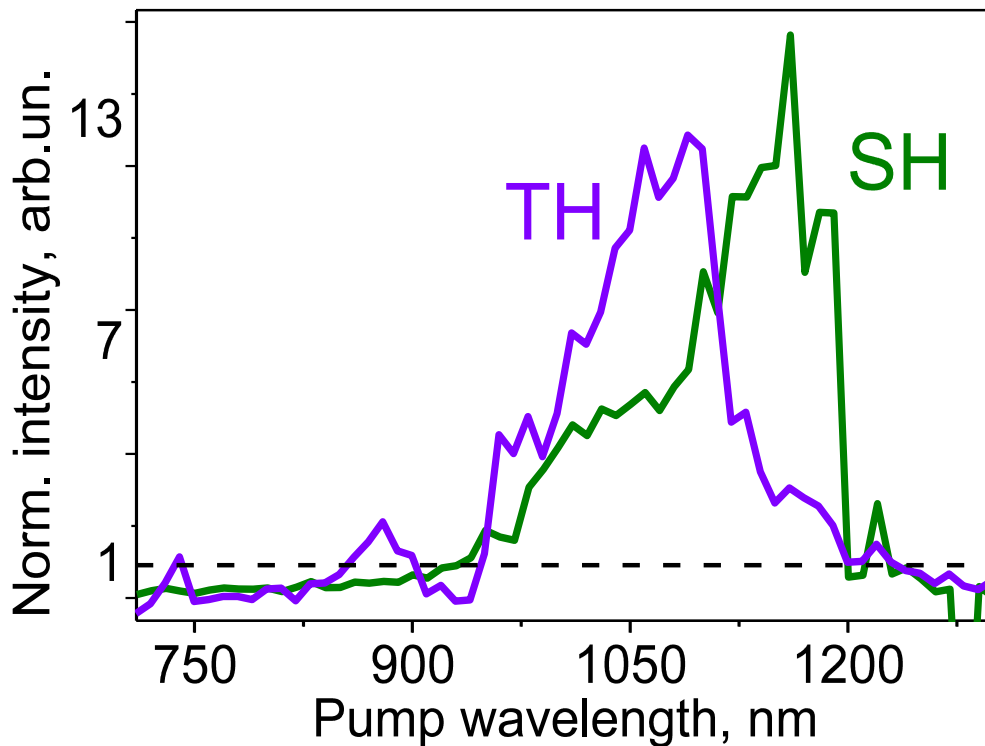


Fig. 4.7 Normalized signals of the second and third harmonics vs pump wavelength for ZnO NPs with a functionalized surface by N,N-diethylaniline.

Fig. 4.7 shows that NPs functionalization significantly increases the second and third harmonics signals in the 900-1200 nm pumping range. The exact origin of this enhancement is still difficult to interpret but can be explained by a modification of the energy levels structure of raspberry-like NPs with appearance of additional surface levels. More detailed analysis of the energy levels structure of ZnO bulk crystals and influence of defects will be presented in the next section.

4.4 Analysis of the energy structure and nonlinear optical response of bulk ZnO crystals with different content of intrinsic defects

4.4.1 PL spectra analysis

The detailed study of the photoluminescence of the ZnO crystals within three regimes of excitation was performed. Fig. 4.8a presents the PL response *via* an interband excitation (I type) with quanta energies 3.8, 4.8, 5.2, and 5.4 eV. One can see a drastic reduction of the PL response efficiency within a decrease of the excitation photon energy from 5.6 eV to 3.5 eV.

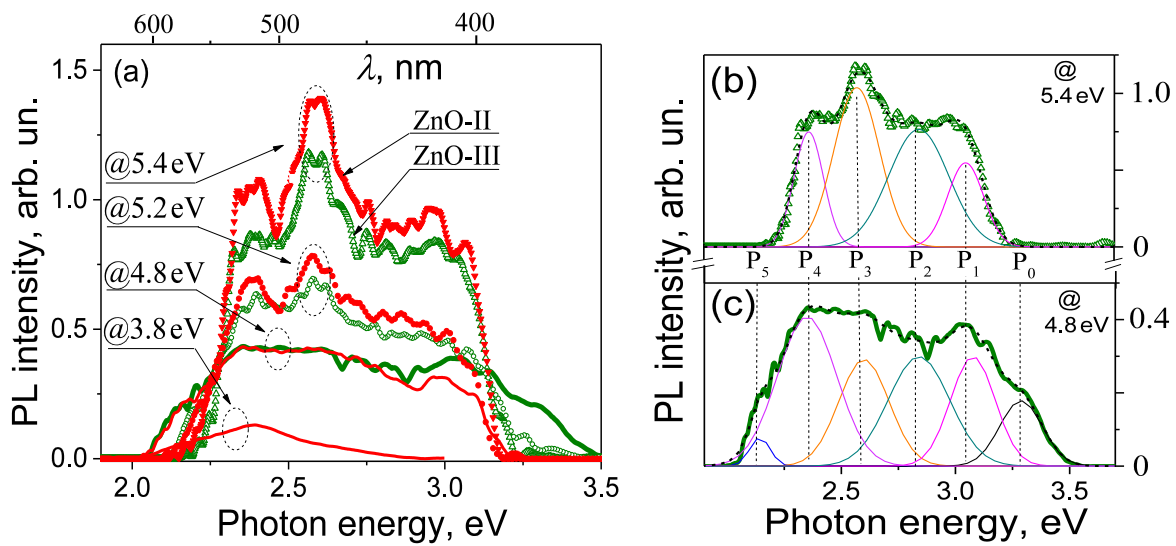


Fig. 4.8 (a) Selected room temperature PL spectra of the ZnO-III (green line) and ZnO-II (red line) crystals; the typical Gaussian decomposition of the PL spectra for the ZnO-III crystal, the PL spectra are excited at (b) 5.4 eV (4 peaks P_1 – P_4) and (c) 4.8 eV (6 peaks P_0 – P_5).

For both samples, we have approximated the PL spectra with four Gaussian components centered at 3.04 eV (P_1), 2.80 eV (P_2), 2.57 eV (P_3) and 2.35 eV (P_4). These components provide an appropriate fitting of the spectral profile without an account of a fine structure impact. The mentioned deconvolution is presented in Fig. 4.8b for the ZnO-III PL spectra excited at 5.4 eV (230 nm). Reduction of the excitation quanta energy below 5.3 eV, which corresponds to the electron work function in the pristine ZnO [140], reveals extra two components centered at 3.32 eV (P_0) and 2.15 eV (P_5), see Fig. 4.8b. It was showed the last components manifestation *via* the significant spreading of

the PL spectra in the excitation range 4.3–5.2 eV in the ZnO-III. The UV P_0 band has the smallest area among all the other components, which is commonly observed in the ZnO crystals with a low content of defects [141]. The blue P_2 and P_3 peaks in the 430–500 nm range provide the main contribution into the PL spectra. The area of yellow P_5 band reaches the maximum at $h\nu = 4.8$ eV. This band contribution rapidly decreases within the $h\nu$ detuning.

We have observed the transformation of the complex multi-peak PL

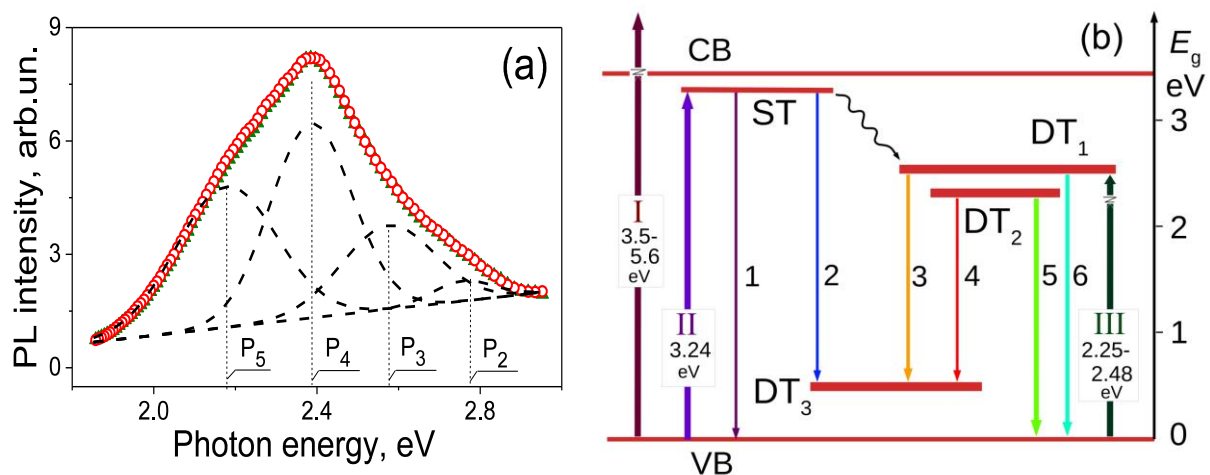


Fig. 4.9 (a) Room temperature PL spectra excited at 3.24 eV (383 nm) for the ZnO-III (triangles) and ZnO-II (circles) crystals; dashed curves represent the deconvolution into a set of Gaussian components; (b) scheme of the electronic transitions in the bulk ZnO: ST – shallow traps, DT₁, DT₂, DT₃ – deep traps, CB and VB – conduction and valence bands.

profiles into a smoothed "tilted triangle-like" ones for $h\nu \leq 3.8$ eV, see Fig. 4.9a. The same spectral response was obtained for the II type sub-bandgap excitation from the VB into the ST state, see Fig. 4.10a. The reduction of the intensity of P_2 and P_3 peaks within the pronounced contribution of the green P_4 and the yellow P_5 bands determines the observed shape of the PL spectra. We have not observed any significant difference in the PL spectral profiles for both crystals.

There are multiple explanations of the visible PL bands in the ZnO related to several intrinsic defects contribution [141–149]. A scheme of the observed radiative transitions is proposed (see Fig. 4.9b) suggesting the involvement of V_O , V_O-V_{Zn} and Zn_i and their complexes.

Upward absorptive transitions correspond to the three types (I – interband $h\nu > E_g$, II – sub-bandgap $h\nu \leq E_g$, III – intragap $h\nu < E_g$) of the PL excitation. Downward vertical radiative transitions numbered from 0 to 6 correspond to the $P_0 - P_6$ bands experimentally observed by means of PL spectroscopy. We have taken into consideration conduction CB and valence VB bands, two kinds of shallow traps $ST_{0,1}$ and 3 kinds of the deep traps DT_{1-3} in the gap.

The proposed scheme is enough to explain the main PL response of the ZnO samples without a detailed description of the fine structure near the edge. The UV near band edge emission P_0 (3.3 eV) is attributed to the radiative recombination into VB from the ST_0 that can be assigned to the bounded excitons [143]. The red-shifted P_1 band centered at 3.0 eV corresponds to the $ST_1 \rightarrow VB$ recombination from Zn_i clusters defects, being associated with structural $V_{Zn}-V_O$ complexes/voids [150]. The ST_1 location depth corresponds to the conductivity activation energy ~ 0.3 eV in the similar ZnO crystals [123].

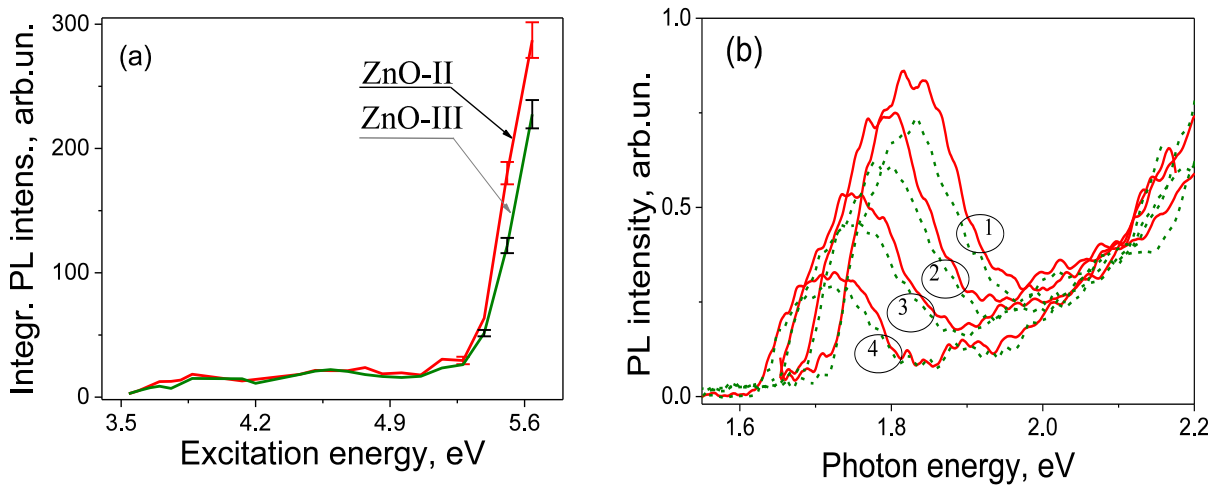


Fig. 4.10 (a) Cumulative area of blue P_2 and P_3 bands emission against the excitation energy for the ZnO-III and ZnO-II crystals; (b) room temperature PL spectra of the ZnO-III (dashed lines) and ZnO-II (solid line) crystals at the excitation of 1 – 2.48, 2 – 2.40, 3 – 2.33, and 4 – 2.25 eV.

The processes (3) and (4) are related to the transitions from deep traps states DT_1 and DT_2 into the VB, peaks P_3 and P_4 , correspondingly. The deep trap DT_1 is suggested to be related to the vacancy cluster $V_{Zn}-V_O$ [149,151] or singly positively charged oxygen vacancy V_O^+ [152], but the last one is thermodynamically unstable. In reference data, the DT_1 state could be also

attributed to doubly positively charged oxygen vacancy V_O^{++} [144,145] or to V_{Zn} [146,147]. From our point of view, they are located at about 0.6 eV above the VB top as the DT_3 state [153]. In the recent publications, the DT_2 state is assigned to the neutral oxygen vacancy V_O^0 [141,154].

Based on obtained results and reference data there are 3 radiative transitions into the DT_3 state can be proposed: (i) $ST_1 \rightarrow DT_3$, (ii) $DT_1 \rightarrow DT_3$, and (iii) $DT_2 \rightarrow DT_3$. The PL bands that are corresponded to these transitions are the blue P_2 band centered about 2.8 eV above the VB top, the orange P_5 band (2.1 eV), and the red P_6 band (2.1 eV), correspondingly. We have observed P_2 and P_5 bands within the interband and sub-bandgap excitations (types I and II), while the P_6 band was observed only with the resonant defects excitation (type III).

Table 4.2 Analysis of PL spectra of the ZnO-II and ZnO-III crystals. E_{ex} - excitation energy, E - peak position, ΔE - its width, $h\Delta\nu$ - the difference in the excitation energy and the peak position.

Excitation, E_{ex} , eB (λ , nm)	$E / \Delta E$, eV	$h\Delta\nu$, eV	Peak area, arb. un.		Ratio II/III
			ZnO-III	ZnO-II	
2.48 (500)	1.82 / 0.11	0.66	91	107	1.18
2.40 (516)	1.79 / 0.11	0.61	76	77	1.01
2.33 (532)	1.74 / 0.10	0.59	41	49	1.20
2.25 (550)	1.71 / 0.10	0.54	37	37	1.00

Analysis of the P_2 and P_3 peaks efficiency in the range 430–500 nm has revealed a significant difference between the response of the studied crystals, which is observed at the excitation quanta $h\nu > 5.3$ eV (see Fig. 4.8a). In the excitation range $3.9 < h\nu < 5.1$ eV, the blue band areas are similar. About 50% enhancement of the blue emission for the ZnO-II crystal was achieved when the $h\nu$ exceeded the electron work function 5.3 ± 0.1 eV of the pristine ZnO that grown by hydrothermal method [140]. The effect can be explained by the ionization of the Zn_i with consequent grating relaxation and carriers

redistribution between the deep defects states DT_1 and DT_3 attributed to the singly and doubly charged oxygen vacancies, being determined by the precursor defects content.

PL response of the ZnO crystals was studied within the excitation of the intrinsic defects in the gap (III type, see Fig. 4.10b). The observed emission band in 1.6–2.2 eV range has the peak position at ~ 1.7 – 1.8 eV and the bandwidth $\Delta E \sim 0.1$ eV (see Table 4.2 for details) that are similar for both crystals within the experimental error. We attributed the PL band to the radiative transitions $DT_{1,2} \rightarrow DT_3$ from the neutral V_O and/or the single charged oxygen vacancy in V_O-V_{Zn} complex into the double charged V_O state.

The observed redshift $h\Delta\nu$ of the PL peak can characterize the position of the DT_3 state ~ 0.6 eV above the top of the VB. Under the resonant excitation conditions, in the tail of the P_2 band at 500 nm or at the peak of the P_1 band at 532 nm, the PL efficiency is about 20% higher in the ZnO-II crystal against that of the ZnO-III that corresponds to their oxygen deficiency y ratio 1.18 (see Table 4.2).

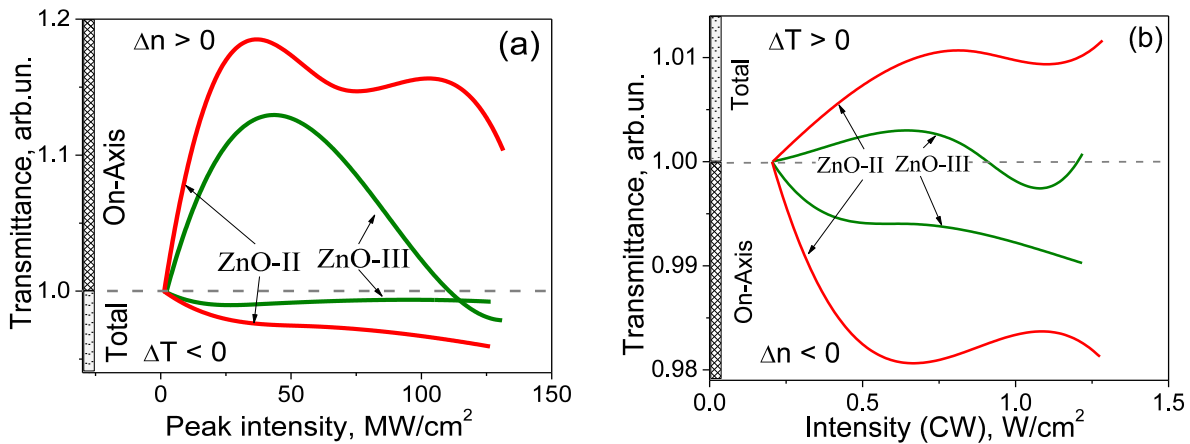


Fig. 4.11 Photoinduced variations of the normalized total and the on-axis transmittance against the intensity in the pulsed (a) and CW (b) excitation regimes at 532 nm.

4.4.2 Nonlinear optical response via self-action of laser radiation

The normalized total transmittance T_t and the on-axis transmittance in the far field T_a , that attributed to the absorptive and refractive NLO responses manifestation, are presented in Fig. 4.11 for the ps range pulsed (a) and the CW

(b) excitation regimes. The total transmittance was normalized to the corresponding spectral one at 532 nm, the on-axis transmittance in the far field – on the corresponding total transmittance. This normalization was done to remove the impact of weak absorption/bleaching effects on the pronounced self-focusing/defocusing effects manifestation in the far field.

It was shown that the observed photoinduced effects are of an opposite sign in the CW and pulsed excitation regimes: the pronounced self-focusing ($\Delta n > 0$) with the on-axis transmittance variation magnitude about 20% at the pulsed regime (a) switched to the self-defocusing ($\Delta n < 0$) with magnitude less than 2% at the CW (b) regime; while photoinduced absorption with the total transmittance variation ($\Delta T < 0$) magnitude $< 4\%$ (a) switched to the photobleaching ($\Delta T > 0$) and the corresponding variation is $< 1\%$ (b). The mentioned distinction reflects the different origin of the NLO responses for the pulsed and CW excitation regimes, but for both cases, the NLO effects manifestation evidently enhances with the rise of the intrinsic defects content.

In the pulsed excitation regime, it was obtained a drastic enhancement of the on-axis transmittance in the far field (see Fig. 4.11a) at moderate peak intensities $I < 50 \text{ MW/cm}^2$ due to the self-focusing effect of the laser beam in the studied crystals. The observed dependencies are not monotonic with the local extremes – 19% and 13% gain – at the peak pulse intensity at about 37 and 44 MW/cm^2 for the ZnO-II and ZnO-III crystals, correspondingly. At the higher peak intensities, the self-focusing effect saturates and turns to the self-defocusing one.

The pronounced self-focusing effect is accompanied by the photodarkening one. The efficiency of the photoinduced absorption is most pronounced in the initial range $I \leq 25 \text{ MW/cm}^2$ with a total transmittance reduction of $\Delta T \sim 2\%$ (ZnO-II) and 1% (ZnO-III). The effect is monotonic in the ZnO-II; while it saturates and turns to the slight photobleaching in the ZnO-III.

In order to characterize the efficiencies of the refractive and absorptive NLO responses, the real $\text{Re}(\chi^{(3)})$ and the imaginary $\text{Im}(\chi^{(3)})$ parts of the effective

NLO susceptibility were estimated in the peak intensity range below the saturation manifestation threshold of the self-focusing and photodarkening effects. The obtained results are presented in Table 4.3; the data were derived according to the route described in [87].

To compare the partial contribution of the refractive and absorptive NLO responses efficiencies we utilized the conventional optical quality parameter – a figure of merit $FOM = \Delta n/(\lambda\Delta\alpha)$ – at the laser wavelength $\lambda = 532$ nm [87]. It was shown that the ZnO-II crystal with the higher intrinsic defects content is characterized by the higher refractive/absorptive NLO response manifestation; the $FOM \sim 40$ is the same as for the ZnO-III one. It is due to a simultaneous enhancement of both the real and imaginary parts of the effective cubic NLO susceptibility $\chi^{(3)}$ (see Table 4.3), being typical for the resonant origin of the response:

$$| \text{Re}(\chi^{(3)})_{\text{ZnO-II}} / \text{Re}(\chi^{(3)})_{\text{ZnO-III}} | \sim | \text{Im}(\chi^{(3)})_{\text{ZnO-II}} / \text{Im}(\chi^{(3)})_{\text{ZnO-III}} | \sim 1.6 .$$

Table 4.3 The comparison of the refractive $\text{Re}(\chi^{(3)})$ and absorptive $\text{Im}(\chi^{(3)})$ NLO responses efficiency with parameters obtained from FTIR and PL spectral data[67].

Sample	^{1,2} $\text{Re}(\chi^{(3)})$, esu		^{1,2} $\text{Im}(\chi^{(3)})$, esu		FTIR		³ PL
	P, $\times 10^{-9}$	CW, $\times 10^{-3}$	P, $\times 10^{-12}$	CW, $\times 10^{-4}$	S_{Σ} , arb. un.	S_2 , arb. un.	$S_{P2}+S_{P3}$, arb. un.
ZnO-II	5.5	-4.2	3.5	-1.0	10114	8140	180
ZnO-III	3.3	-2.0	2.3	-0.3	6598	5105	122
Ratio II/III	1.7	2.1	1.5	3.3	1.5	1.6	1.5

^{1,2} Data obtained at the pulsed (P) and continuous wave (CW) excitations; ³PL was excited at 5.51 eV.

The origin of the efficient photoinduced refractive index variation is dealing with the resonant condition of the laser quanta 2.33 eV with the DT_2 defect band position vs. the VB. We should take into account not only the direct transition of the electron from the VB into the DT_2 , but also the excitation of the

trapped carriers from the DT_2 and DT_1 states into the CB with further non-radiative recombination through the ST into DT_1 and DT_2 states. Each step of the excitation and trapping of the electrons at the gap states leads to an essential lattice reconstruction and a fast polarizability changes in the vicinity of the defect site comparing to the typical times of radiative recombination in ZnO, that exceed 60 ps for the ultra-fast PL channel [155].

The NLO response can be interpreted with the following assignment of the DT_2 band to the neutral oxygen vacancy V_O and DT_1 band to the complex of the singly charged V_O with the V_{Zn} defect that is thermodynamically stable at room temperature [152].

According [141], the V_O formation results in the two electrons from the removed O anion becoming trapped at the vacancy site and occupying a hydrogenic state in the band gap with a strong cation relaxation inwards with the most pronounced Zn ion shifts along the c axis by 0.25 Å. On ionization, this effect is reversed and now all four nearest neighbor Zn ions move away from the vacancy, being in line with the residual electron occupation of strongly localized s-like orbital in the vacancy. Accumulation of the electrons at the DT_1 and DT_2 localized states across the 30 ps single laser pulse excitation provides the efficient self-focusing response ($\Delta n > 0$) of the trapped carriers while the energy quanta are slightly less by energy the peak P_4 of radiative transition at 2.35 eV [139]. It dominates over the self-defocusing response of the delocalized carriers observed under the CW irradiation at the same wavelength.

The obtained NLO refractive index efficiency $\text{Re}(\chi^{(3)}) \sim 10^{-9}$ esu together with high magnitudes of the FOM parameter for both samples shows the high potential of the ZnO single crystals for the photonics application with pulsed resonant excitation of the intrinsic defects.

Contrary to the pulsed excitation regime, we have observed a reduction of the on-axis transmittance in the far field versus I for the CW laser excitation regime (Fig. 4.12b) that corresponds to the self-defocusing effect ($\Delta n < 0$). It is

typical for delocalized carriers, due to the incident field screening – so-called Drude-like response.

The interstitial Zn_i is the main intrinsic source of n -type conduction in the ZnO [141]. It is known V_{Zn} defects act as the compensating acceptors, and they increase the electric resistance. While the vacancy clusters remove the isolated V_{Zn} and decrease the resistance [149]. Here, we revealed that the oxygen vacancies, showing an emission peak at ~ 2.4 eV, acted as a deep donor under the optical excitation.

For the case of the CW excitation, we should also suggest the impact of the Zn_i and V_O migration in the ZnO bulk. As it was shown in Refs. [152,153], the Zn_i are the fast diffusers with the migration barrier ~ 0.57 eV. The calculated migration barrier for the neutral V_O is ~ 2 eV that also can be activated within quanta 2.33 eV [156]. The diffusion process can cause the crystal lattice reconstruction with the pronounced polarizabilities modification in the vicinity of the defect sites.

Obtained results show about two times more efficient refractive NLO response in ZnO-II vs. ZnO-III (see Table 4.3) that corresponds to about 2% and 1% reduction of the on-axis transmittance in the far field (Fig. 4.11b) for the CW laser intensity $I \sim 0.6$ W/cm² with further saturation of the effect. The efficiency of the refractive NLO response is six orders of magnitude higher in comparison with the pulsed excitation regime. The observed refractive effects are accompanied with a slight photoinduced bleaching effect $< 1\%$ that was more efficient for the ZnO-II crystal, with ratio II/III for $Im(\chi^{(3)})$ of about 3.3 (see Table 4.3). It can be explained by the contribution of multiple mechanisms into the refractive and absorptive NLO responses.

The high efficiency of the NLO response $|Re(\chi^{(3)})| \sim 10^{-3}$ esu in the resonant CW excitation mode at 532 nm was obtained. However, studied samples demonstrate low saturation threshold resulted only in about 1–2 % photoinduced variations for the on-axis transmittance in the far field. The small magnitude of the observed effect can be a drawback for the practical application

of the mentioned technique for the remote diagnostics of intrinsic defects in ZnO.

We have found correlations among the different optical diagnostics techniques data (see Table 4.3) with probing in the different (far-IR, UV, and VIS) spectral ranges. The observed different optical properties of studied samples with different concentration of defects can be explained by the contribution of the deep defect states into each given kind of the studied response.

It was shown that the rise of the defects content provided almost the same enhancement of the ZnO-II vs. the ZnO-III responses both for the integrated intrinsic vibrations bands in the IR range ($400\text{--}640\text{ cm}^{-1}$) and for the visible PL blue band ($430\text{--}500\text{ nm}$), being excited with the UV photon energy $h\nu = 5.51\text{ eV}$. The mentioned $h\nu$ magnitude corresponds to the highest difference in the blue PL band areas. Both kinds of the responses – absorptive in the infrared and radiative in the visible range have the same origin *via* the main contribution of the clustered defects complexes. The 1.5 times S_{Σ} enhancement also coincides with the rise of the photoinduced absorption efficiency in ZnO-II vs. ZnO-III within the picosecond range pulsed laser excitation at 2.33 eV (532 nm).

The highest II/III ratios of 2.1 and 3.3 were obtained for the refractive and absorptive NLO response efficiencies under CW laser excitation at 2.33 eV . We have observed the typical self-defocusing response of the carriers from the shallow traps and that excited from the deep traps with the optical absorption saturation manifestation. The high efficiency of both kinds of the response compensated with the manifestation of weak effects *via* a low saturation threshold of the photoinduced effects.

From the practical point of view, the most promising is the refractive NLO response efficiency readout with the picosecond range under a single pulse excitation regime. Its efficiency is 3 orders of magnitude higher than the absorptive one $|\text{Re}(\chi^{(3)})| \sim 10^3 |\text{Im}(\chi^{(3)})|$, see Table 4.3. Obtained ratio II/III = 1.6 for $\text{Re}(\chi^{(3)})$ is close to the FTIR component S_2 enhancement centered at 475

cm^{-1} . The corresponding band DT_1 , which is attributed to the clustered $V_{Zn}-V_O$ structure with the associated framework of Zn_i , has the crucial impact on processes of the excitation of electrons from the deep donors, their recombination pathway, trapping, radiative recombination, and optical absorption with account for the crystal lattice relaxation.

4.4.3 Elastic light scattering analysis of ZnO crystals

CW laser beam extinction *via* the elastic scattering effect at wavelength 532 nm was studied in order to estimate the impact of the intrinsic defects concentration on the modification of the profile of optical scattering indicatrix in the ZnO crystals. For the transmitted, reflected, and scattered lights, the spatial distribution cross-section in the forward and backward hemispheres is presented in a polar plot in logarithmic scale (Fig. 2.3b).

Table 4.4 Optical parameters of ZnO crystals: total transmittance T , total reflection R , absorption coefficient α , and scattering losses into the forward ε_F and backward ε_B hemispheres at $\lambda = 532$ nm.

Sample	^a Composition $Zn_{1-x}O_{1-y}$		Optical parameters				
	x	y	T , %	R , %	α , cm^{-1}	ε_F , %	ε_B , %
ZnO-II	0.062	0.060	51.7	8.3	5.1	22.7	5.9
ZnO-III	0.048	0.051	59.3	6.2	4.2	18.5	5.1
Retio. II/III	1.29	1.18	0.87	1.34	1.21	1.23	1.16

^aNote: x and y are concentrations of vacancies refined from the results of ND analysis [123].

The measurements were done at the normal incidence with a collimated Gaussian laser beam with divergence $\Delta\theta = 24'$. We applied a wide beam spot at the sample plane of about 1.5 mm to provide a representative scattering signal readout with a proper spatial averaging.

It was observed a pronounced manifestation of a laser beam self-defocusing effect in the forward direction with a rise of the laser beam power/intensity (see Fig. 2.3b). One can see 1.4 times spreading of the beam

FWHM angular divergence in the far field from $\Delta\theta = 3^\circ 30'$ at $I = 0.37 \text{ W/cm}^2$ to $4^\circ 50'$ at 0.78 W/cm^2 in the ZnO-II. The dashed line represents the reference freely propagating laser beam. The incident laser beam power was controlled within neutral optical filters. The further rise of the laser intensity leads to the saturation of the self-defocusing effect manifestation. Similar divergence enhancement with I rise was also observed for the reflected in the backward direction beam. We attributed the self-defocusing effect to the response of Drude-like delocalized carriers (both the intrinsic and photoinduced ones from the deep traps) response, being discussed in the section dealing with the NLO response analysis under the CW laser excitation.

Analysis of the angular resolved scattered signal distribution – the elastic scattering indicatrix – was performed (see Fig. 2.3) with the CW laser intensity $I = 1.53 \text{ W/cm}^2$ that provided (i) enough level for the scattered signal acquisition in an almost perpendicular direction to the incident beam within a dynamic range at about 8 orders of magnitude and (ii) a saturated self-defocusing effect contribution to avoid the impact of small laser power/intensity fluctuations.

Both crystals have higher scattering losses in the forward direction in comparison with the backward one. We have observed the higher scattering efficiency of the ZnO-II vs. the ZnO-III for the wide-angle θ ranges $30^\circ < |\theta| < 60^\circ$ in the forward hemisphere and $100^\circ < |\theta| < 135^\circ$ in the backward one. From the data of the angular resolved scattered signal distribution, we estimated the total reflection R in the backward hemisphere, the total transmittance in the forward hemisphere T that almost coincides with the spectral transmittance at 532 nm obtained with the integrated sphere. It gives a possibility to calculate the effective absorption coefficients for the crystals $\alpha = -\ln(T/(1-R))/d$, where d is the thickness of the crystal. We have also estimated the scattering losses into the forward/backward $\varepsilon_F/\varepsilon_B$ hemispheres extracting from the total transmittance/reflectance data the measured signals along the ballistic incident/reflected beam trajectories according to the route described in [98].

A comparison of the presented optical parameters is given in Table 4.4. It is shown that a rise of the defect content causes an enhancement of the elastic scattering losses magnitudes in both hemispheres with about 4 times higher contribution of the effect in the forward direction for both crystals. We have also observed an enhancement of the total reflection R that corresponds to the reflectance spectral data obtained with the integrated sphere. An enhancement of the optical absorption in the transparency range at about 20% for the ZnO-III correlates with the rate of the molar oxygen vacancies content y , while the ϵ_F enhancement is intermediate between the rise of the molar content of zinc vacancies x and oxygen vacancies y . The last can be explained by the contribution of both acceptors (V_{Zn}) and deep donors (V_O) in the response of delocalized carriers under the CW laser irradiation. The rate II/III for the total reflection R agrees with that for the V_{Zn} content x .

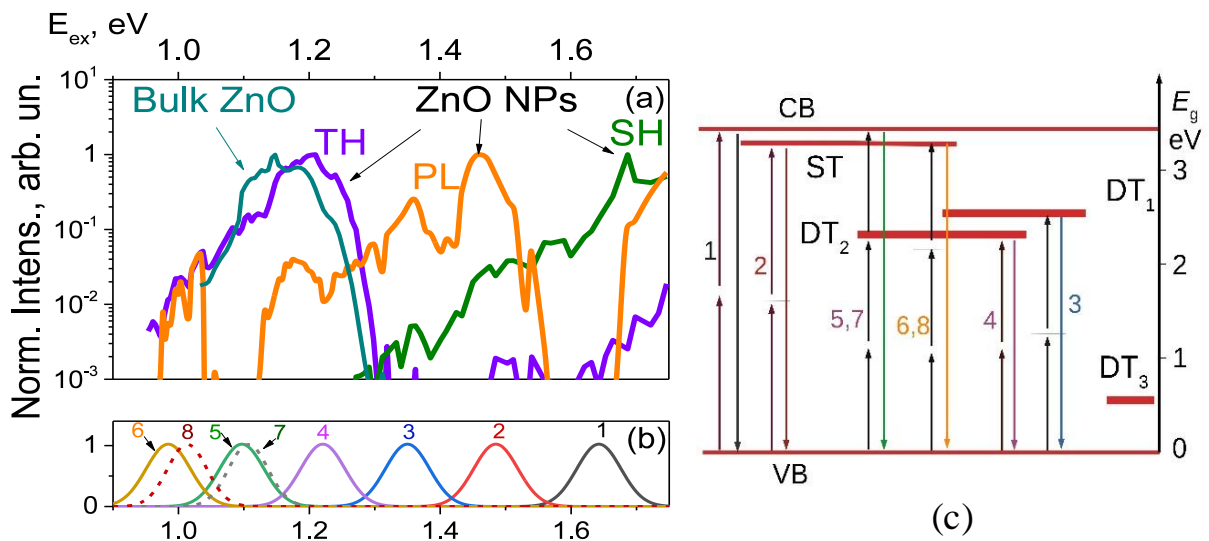


Fig. 4.12 (a) Normalized signals (log scale) of the second, third harmonics and PL vs pump wavelength for ZnO HNPs (~150 nm) and THG signal for bulk ZnO-III for comparison. (b) The positions of the peaks P_0 - P_5 obtained from the PL analysis in bulk ZnO crystals (see Fig. 4.9b) and can be excited by two (solid lines) or three (dashed lines) photons. (c) Schematic representation of mechanisms of resonant amplification of the efficiency of generation of harmonics.

These results show the positive correlation of the elastic optical scattering and the Vis-NIR spectroscopy data with the defects content in the ZnO bulk crystals. This is promising for the crystals diagnostics due to the high

polarizabilities of the defect states and the efficient refractive response of the photoinduced delocalized carriers.

4.4.4 Comparison of spectral response of ZnO NPs and bulk crystals

The spectral analysis of bulk ZnO crystals with different concentration of defects, described in the previous paragraph, was used to clarify the wavelength-dependence efficiency of the various signals emitted by ZnO nanoparticles under femtosecond excitation. The idea is to interpret the observed SHG, THG and PL responses (see Fig. 3.16 in chapter 3) using the reconstructed energy level diagram of bulk ZnO. We thus assumed a similar structure of defects for both bulk crystals and NPs. We show (see Fig. 4.12b) the different luminescence peaks, that can be excited by two or three photons, together with the SH, TH and PL responses of ZnO NPs (Fig. 4.12a)

Optical harmonics generation occurs through virtual levels, and the probability of this process depends on the intensity of the excitation. If the position of virtual levels coincides with the position of real energy levels, then the probability increases significantly, as shown in references [116,157].

In Fig. 4.12a, three ranges of wavelengths are distinguished, for which the enhancement of signal is observed: (1) $\lambda < 1000$ nm (1.24 eV), (2) 1000 nm (1.24 eV) $< \lambda < 1100$ nm (1.13 eV), (3) $\lambda > 1150$ nm (1.08 eV). In the range (1), second harmonic generation and PL are promoted due to two-photon excitation of the band gap and through real levels of defects (see Fig. 4.12c). The band (2) is characterized by high efficiency of third harmonic, due to direct three-photon excitation of the band gap and through intermediate real levels. In the (3) range, the third harmonic is amplified due to three-photon excitation of levels near the bottom of the conduction band. We thus observed a very interesting correlation between the real levels structure of ZnO NPs and nonlinear optical response. These first data needs further confirmation but it shows the interest of the developed experimental set-up, which can perform nonlinear optical spectroscopy of individual nano-object.

Conclusions to the chapter 4

- 1) Characterization of synthesized ZnO NPs was carried out by the method of self-action of ps laser pulses at 1064 nm. It was shown that the efficiency of the refractive $\text{Re}(\chi^{(3)})$ and the absorption $\text{Im}(\chi^{(3)})$ of the NLO responses depends on the type of solvent used for the synthesis of the NPs. It was shown the correlation between the value of $\text{Im}(\chi^{(3)})$ and the area of the PL band about 2.34-2.41 eV, which corresponds to the response of oxygen vacancies in ZnO.
- 2) The efficiency of the second harmonic generation was studied under *fs* laser excitation at 800nm. A noticeable SHG signal was detected for these very small (2 nm) NPs.
- 3) Analysis of the optical harmonics generation efficiency of commercial ZnO NPs (~ 150 nm) with surface functionalized by small crystalline ZnO NPs (2 nm) was performed. It was shown that such functionalization could enhance the second and third harmonics intensity within a certain excitation wavelength range.
- 4) For decoding the mechanisms of the different observed NLO responses, a diagnostic of bulk ZnO single crystals with different concentration of intrinsic defect was performed. It is shown that there is a correlation between the values of the real and imaginary parts of the cubic NLO susceptibility with the data of PL and IR spectroscopy in the area of defective bands, the efficiency of elastic optical scattering - with the concentration of defects.

Chapter 5 Analysis of the optical harmonics generation efficiency of composite materials based on single crystals of KDP

Potassium dihydrogen phosphate (KDP) crystals are a well-known and a widely-used commercial NLO material widely used in information technology, laser physics, and nonlinear optics. A wide range of its applications is due to the relatively simple and cheap technology of growing from aqueous solution, a high threshold of laser destruction and the ability to create wide-aperture elements on its basis. However, relatively low values of the nonlinear coefficient d_{36} (KDP) = 0.4 pm/V stimulate the search for new approaches to improve the efficiency of the second and the third harmonics generation.

A promising way to enhance the NLO response of known bulk materials is to create composites based on incorporation of nanosized subsystems. In this work, KDP single crystals with incorporated TiO_2 , $\text{Al}_2\text{O}_3 \cdot n(\text{H}_2\text{O})$ nanoparticles and L-arginine molecules are studied. It is shown that the incorporation of nanoparticles allows to amplify the NLO response of the system and substantially increase the efficiency of the generation of optical harmonics.

5.1 Composites based on KDP single crystals

Crystals with extremely high structural and optical perfection makes it possible to produce wide-aperture frequency multipliers of laser radiation and Pockels cells for powerful laser setups [47,158].

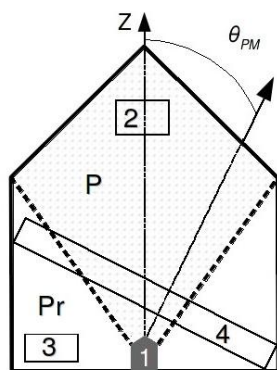


Fig. 5.1 The schematic representation of KDP crystals with pyramidal (P) and prismatic (Pr) sectors of growth, θ_{PM} is the angle of synchronism. 1 - initial crystal, 2,3 - samples of Z-cut of P and Pr of growth sectors, 4 - typical cut with maximum aperture.

Usually, to create wide-aperture elements based on KDP, the cut of the crystal is maximized (see 4 in Fig. 5.1). As a result, the final product includes

parts from different growth faces. It was shown that such an approach is destructive, since the properties of each face differ [48,57].

Since the crystals of the KDP group contain a developed network of hydrogen bonds, they can effectively capture impurity centers of different nature. This facilitates their application as model objects for new data processing elements, nonlinear and active laser environments.

In this work, KDP crystals and composites are grown in the Institute of Single Crystals of the National Academy of Sciences of Ukraine.

5.1.1 KDP single crystals with incorporated TiO₂ NPs.

Nominally pure KDP and KDP:TiO₂ with incorporated TiO₂ NPs were grown by the method of lowering the temperature in the crystallizer [48]. The final size of the grown crystals was 60×60×70 mm³, the average growth rate was ~ 3 mm·day⁻¹ in both directions [001] and [100]. No effect of TiO₂ concentration on the pH of the solution, saturation temperature and crystalline morphology was found. More detailed information on the growth of crystals and their characterization is described in [48,57].

Table 5.1 Concentration of TiO₂ nanoparticles in the growth solution and concentration of TiO₂ nanocrystals in a KDP:TiO₂ single crystal.

Sample	TiO ₂ conc, wt. %	Conc of NPs, 10 ¹⁰ cm ⁻³
P	-	-
P5	10 ⁻⁵	3.2
P4	10 ⁻⁴	33
Pr	-	-
Pr5	10 ⁻⁵	1.6
Pr4	10 ⁻⁴	16
Pr3	10 ⁻³	160

Experimental samples were cut from a different growth sector in the form of thin plates 10 × 10 × 0.8 mm³ (see Fig. 5.1) perpendicular to the optical axis (Z-cut). The designation of the samples, their concentration of NPs in the growth solution and the concentration of NPs in the grown crystals are presented in Table 5.1. One can see that the NPs is mainly attracted to the pyramidal (P) sector of growth, due to different surface

charges of various sectors of growth [159]. Also, NPs form a layered structure in the crystal (see Fig. 5.2). Spectrum of transmission are presented in Fig. 5.3a.

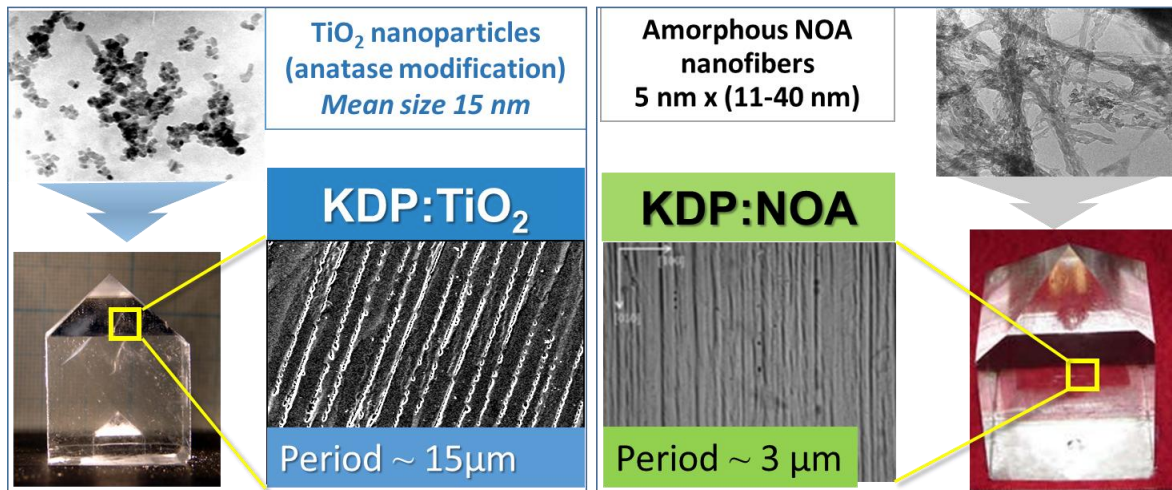


Fig. 5.2 Layered structure in composites based on the KDP matrix with incorporated TiO_2 NPs and NOA nanofibers [48].

Previously, a study of "thick" (~ 1 cm) crystals of KDP: TiO_2 was carried out under phase matching conditions of and excitation with picosecond laser pulses at 1064 nm. It was demonstrated [69] an increase of about 70% of the efficiency of SHG. The effect was due to the internal self-focusing in nanocomposites, which is produced by a giant cubic NLO response of anatase nanocrystals embedded in the matrix, and its effect on the proton subsystem of the KDP crystal. For "thin" (~ 0.8 mm) samples, a significant change in the quadratic nonlinear coefficient due to the inclusion of the NPs was not shown, which also did not change with the concentration of the NPs [160]. The resulting reduction in the efficiency of SHG approximately 2 times for the Pr4 crystal in comparison with the pure Pr was explained by the resonance absorption of the energy at SH wavelength and the two-photon pump absorption by the TiO_2 NPs.

5.1.2 KDP single crystals with incorporated nanofibers of nanostructured oxyhydroxide of aluminum

Nominally pure KDP crystals and KDP:NOA with incorporated nanostructured oxyhydroxide of aluminum (NOA) with different concentrations of nanofibers (NF) of NOA were grown from aqueous solutions by reducing the temperature on seed crystals with dimensions of $10 \times 10 \times 10$ mm³. As raw material, a potassium dihydrogenphosphate salts with impurities (Fe, Cr, Sb, Bi, Cu, Hg, Ag, Pb) of less than 10^{-5} wt.%, $\text{Al} \leq 10^{-4}$ wt.%. NOA NF was prepared

by oxidation of aluminum in a humid atmosphere through mercury film at room temperature [161].

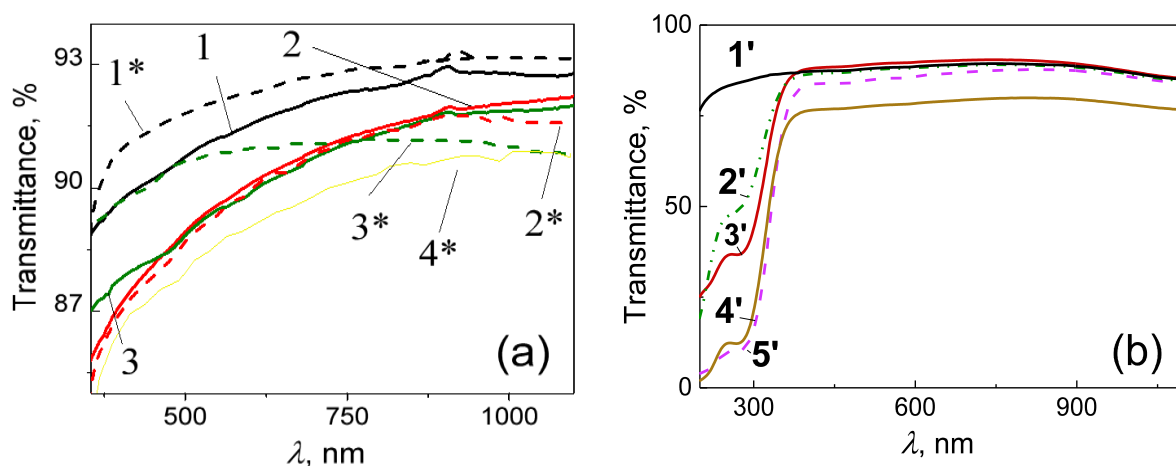


Fig. 5.3 a) Transmittance spectra for KDP:TiO₂ from pyramidal and prismatic growth sectors. 1/1* – P/Pr; 2/2* – P5/Pr5; 3/3* – P4/Pr4; 4* – Pr3[48]. b) Transmittance spectra for KDP:NOA: 1' - P, 2' - Pr, 3' - Pr5, 4' - Pr4, 5' - Pr3[161].

The resulting material consists of amorphous NF with diameter of ~ 5 nm and a length of ~ 150 nm and with high porosity ($\sim 99\%$) and low density ($0.02\text{--}0.04$ g/cm³) [161]. The concentration of NOA NF varied from 10^{-5} to 10^{-3} wt.% in the growth solution. The process of growth of crystals KDP: NOA is described in detail in [162].

For experiments, optically polished Z-cut of $5 \times 5 \times 0.7$ mm³ plates from pyramidal (R) and prismatic (Pr) sectors of growth were used. The designation of the samples, their concentration of NF in the growth solution and the concentration of NF in the grown crystals are presented in Table 5.2.

An absorption band with a peak position at $\lambda = 270$ nm was observed for samples cut from the growth sectors of Pr. The transmission coefficient in the UV range at $\lambda \leq 350$ nm significantly decreases (Fig. 5.3b) with an increase in the concentration of Al³⁺ (Table 5.2). This means that the absorption band in prismatic sectors of growth $\{1\ 0\ 0\}$ can be caused by the inclusion of NOA in the crystal KDP. The absorption effect of the NOA NF fraction due to their own transitions in the visible range [163] can provide an insignificant contribution to the decrease in transmittance.

Table 5.2 Concentration of NOA NF in growth solution and concentration of NF in a KDP:NOA single crystal.

Sample	Conc. of NF in solution, wt. %	Conc. of Al in crystal $\cdot 10^{-4}$ wt. % [162]
P	-	1
P5	10^{-5}	2
P4	10^{-4}	2
P3	10^{-3}	2
Pr	-	10
Pr5	10^{-5}	15
Pr4	10^{-4}	30
Pr3	10^{-3}	100

A comparison between spectra of KDP:NOA and KDP:TiO₂ [164] demonstrates a correlation between the inclusion of metal oxides and the variation of the transmission of composite crystals. Namely, for KDP:TiO₂ Pr and crystals KDP:NOA P, the impurity NPs / NF in the solution does not significantly affect the transmittance. At the same time in different growth sectors - KDP:TiO₂ P and KDP:NOA Pr, the effective reduction of transmittance is observed and can be explained by scattering losses.

5.1.3 KDP doped by L-arginine molecules

Along with the studying of composites based on KDP matrix and metal oxides NPs/NFs it was grown a KDP:L-arg crystals, that have been doped with amino acid L-arginine (L-arg). They were grown from aqueous solutions on spot seed, by the method of lowering the temperature [165]. The occurrence of L-arg molecules (1.4 wt% in the mother solution and 0.1 wt% in the crystal) in the crystal was confirmed by the ninhydrin reaction [165]. The nominally pure and doped L-arg crystals of KDP are characterized by X-ray diffractometry, it is shown that the structural perfection of doped crystals corresponds to a pure KDP [165]. It was established that the occurrence of L-arg molecules leads to the formation of additional hydrogen bonds in the lattice and the disappearance of proton vacancies associated with the presence of aliovalent impurities.

5.2 Nonlinear optical response of KDP single crystal with incorporated TiO₂ nanoparticles

5.2.1 Elastic optical scattering indicatrices at 1064 nm

In order to study the optical quality of the KDP:TiO₂ crystals we measured the elastic optical scattering indicatrices at 1064 nm. The chosen wavelength is in the range of the TiO₂ NPs resonant excitation.

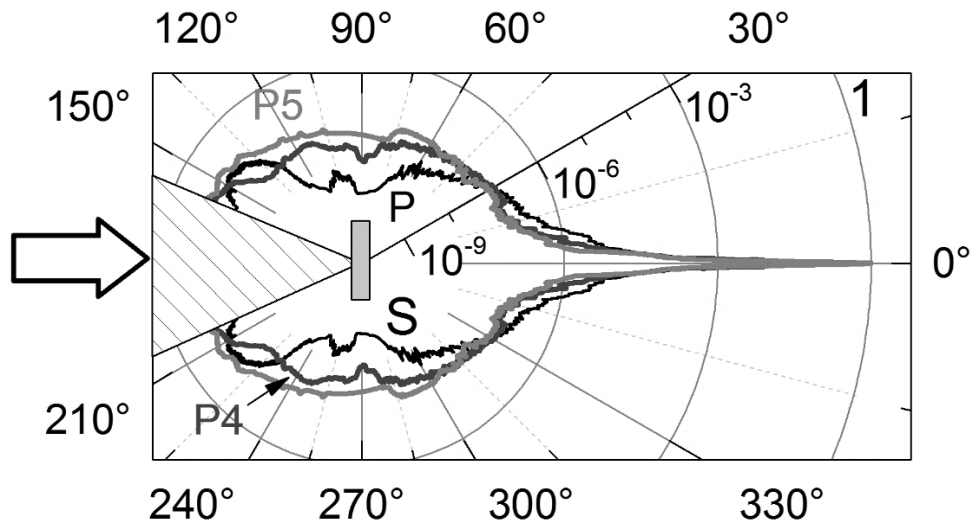


Fig. 5.4 Scattering indicatrix cross-section for KDP:TiO₂ single crystals cut from pyramidal growth sector under resonant excitation of TiO₂ NPs by CW laser radiation at 1064 nm wavelength: P, – nominally pure KDP (P); P5, P4 – KDP with incorporated TiO₂ 10⁻⁵ wt.% and 10⁻⁴ wt.% correspondingly.

The typical scattering indicatrices cross sections for the samples cut from pyramidal (P) growth sector are presented in Fig. 5.4 in logarithmic scale. Propagation direction of the incident laser beam is shown with empty arrow. The sample is positioned in the center for better clarity. All data were normalized on the maximum scattering intensity magnitude for the nominally pure P crystal, that occurs at the 0 scattering angle. It can be seen that scattering indicatrices profiles are strongly dependent on TiO₂ NPs concentration. From the obtained dependencies the scattering losses $\varepsilon_{\text{scat}}$ into forward hemisphere were estimated according to the approach described in [69].

The obtained results are presented in Table 5.3 and compared with the ones obtained for the same crystals at 532 nm [68]. One can see that the

incorporation of TiO₂ NPs results in scattering efficiency reduction for the crystals from P growth sector at 1064 nm (see Table 5.3). This effect can be explained by a lower incorporation of non-controlled impurities in the crystals thanks to titanium dioxide NPs [54]. In contrast, it is observed an increase of ϵ_{scat} for the case of the resonant excitation of the KDP matrix intrinsic defects at 532 nm.

Table 5.3 Samples notation, thicknesses, TiO₂ NPs concentration in growth solution, integral scattering losses ϵ_{scat} into forward hemisphere for the KDP:TiO₂ single crystals under the resonant excitation of the NPs defect states at 1064 nm and KDP crystalline matrix intrinsic defects at 532 nm. Typical error of thickness measurement is 10 μ m.

Sample	TiO ₂ conc., wt. %	Thickness, mm	ϵ_{scat} (1064 nm), %	ϵ_{scat} (532 nm), %	$\frac{\epsilon_{\text{scat}}(1064 \text{ nm})}{\epsilon_{\text{scat}}(532 \text{ nm})}$
P	-	0.81	0.5	1.0	0.50
P5	10 ⁻⁵	0.75	0.3	1.7	0.18
P4	10 ⁻⁴	0.76	0.4	2.5	0.16
Pr	-	0.83	0.6	1.1	0.54
Pr5	10 ⁻⁵	0.78	1.2	1.7	0.71
Pr4	10 ⁻⁴	0.75	0.8	1.3	0.62
Pr3	10 ⁻³	0.81	0.7	2.8	0.25

For the samples cut from Pr growth sector the scattering efficiency increase versus the nominally pure KDP crystal was shown. The rise of the NPs concentration results in ϵ_{scat} reduction that can arise due to the waveguide effect between the NPs layers (see Fig. 5.2).

A possible explanation of the mentioned effect can be following. Due to the specific layered structure [48] the studied samples and effective self-focusing refractive response of the incorporated NPs [57] we can observe photoinduced waveguide array effect manifestation contribution. For the conventional case of homogeneous distribution of NPs in the dielectric matrix a

rise of the NPs concentration produces higher optical elastic scattering losses [164]. For the Z-cut crystals cut from the prismatic growth sector laser beam propagation direction coincides with photoinduced waveguide array originated via resonant excitation of the TiO₂ NPs and the consequent formation of the spontaneous polarization domains [55] with higher refractive index along the NPs layers (see Fig. 5.2). The mentioned photoinduced waveguides suppress the scattering losses [68].

For the Z-cut crystals cut from the pyramidal growth sector the laser beam passes through a set of TiO₂ NPs layers. It provides a similar scattering losses for the KDP:TiO₂ crystals with different concentration of the NPs in mother liquor [68,164].

In general, the obtained scattering losses at 1064 nm do not exceed 1% that indicates high optical quality of the studied nanocomposites. The ratio $\varepsilon_{\text{scat}}(1064 \text{ nm})/\varepsilon_{\text{scat}}(532 \text{ nm})$ remains less than 0.71 for the studied samples (Table 5.3).

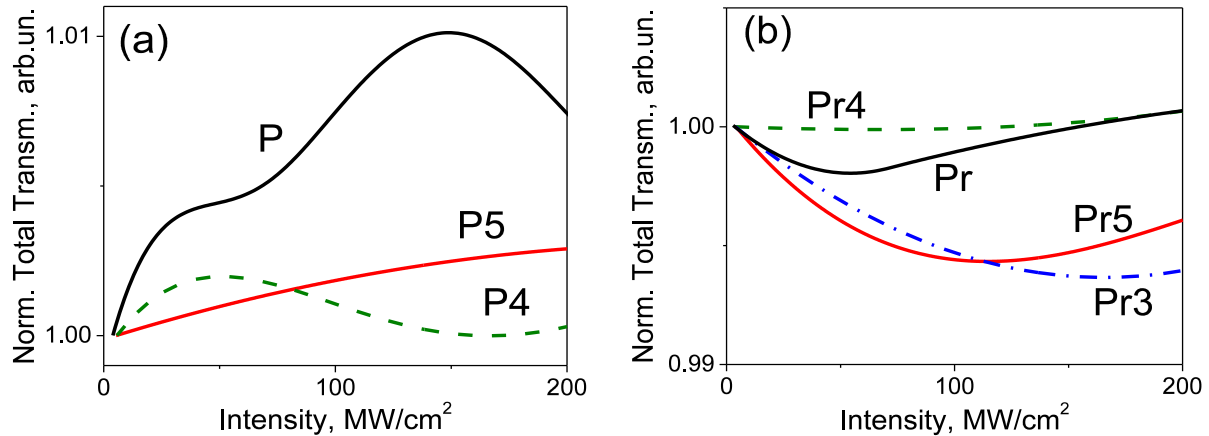


Fig. 5.5 The photoinduced variations of the total transmittance for the KDP:TiO₂ single crystals from pyramidal - (a) and prismatic (b) growth sectors. The excitation was performed by the picosecond laser pulses at 532 nm. Samples notation is presented in Table 5.1.

5.2.2 Self-action of picosecond laser pulses at 532 nm

The NLO properties of the KDP and the KDP:TiO₂ single crystals were studied within the self-action of picosecond laser pulses at 532 nm. The

excitation wavelength is overlapped with the intrinsic defects bands of localized and self-trapped hole polarons in the nominally pure KDP crystals [52].

The photoinduced variations of the normalized total transmittance for the samples are presented in Fig. 5.5. One can see that even the nominally pure KDP matrix exhibit different NLO response in P and Pr growth sectors. For the sample P a photoinduced optical bleaching $\Delta\alpha(P) < 0$ was observed versus a photoinduced darkening $\Delta\alpha(Pr) > 0$ for the Pr one. The incorporation of the TiO_2 NPs into the KDP crystal results in the reduction of its absorptive NLO response efficiency in P growth sector. The effect can be explained by a lower concentration of non-controlled impurities (intrinsic defects) in the KDP: TiO_2 nanocomposites. For the Pr growth sector, a significant photoinduced absorption efficiency reduction was observed only for the Pr4 crystal.

In general, the photoinduced variations of the total transmittance for all studied samples do not exceed 1%. It is less versus the previously observed 3% within the picosecond laser pulses excitation at 1064 nm that corresponds to the resonant excitation of the TiO_2 NPs [57].

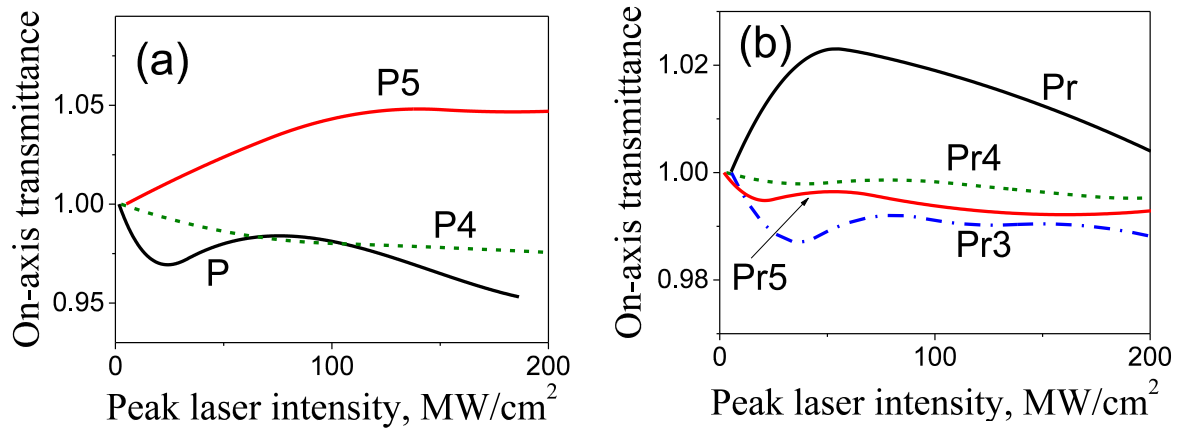


Fig. 5.6 The photoinduced variations of the on-axis transmittance for the KDP: TiO_2 single crystals cut from pyramidal (a) and prismatic (b) growth sectors. The excitation was performed by the picosecond laser pulses at 532 nm.

In comparison to the photoinduced absorption, the photoinduced variations of the on-axis transmittance are more efficient. The dependencies are presented in Fig. 5.6 for the samples cut from P and Pr growth sectors correspondingly. For the nominally pure KDP matrix it was observed about 4%

self-defocusing effect in P growth sector $\Delta n(P) < 0$ versus the 2% of the self-focusing one $\Delta n(Pr) > 0$ in the Pr growth sector. The observed different sign of the $\Delta\alpha$ and the Δn in different growth sectors can be used for monitoring of the grown KDP crystals quality. It should be noted that the mentioned effects saturate at about 60 MW/cm².

In the case of the P growth sector the incorporation of TiO₂ NPs results in a refractive NLO response sign change to the self-focusing for the sample P5 and significant reduction of the pronounced self-defocusing effect efficiency for the sample P4. For the Pr growth sectors, the self-defocusing effect was observed for all crystals with TiO₂.

Table 5.4 The real and imaginary parts of the cubic nonlinear optical susceptibility $\chi^{(3)}$ for KDP:TiO₂ single crystals with different TiO₂ NPs concentration measured under *ps* laser excitation at 532 nm.

Sample	Re($\chi^{(3)}$), $\times 10^{-11}$ esu	Im($\chi^{(3)}$), $\times 10^{-13}$ esu
P / Pr	-3.1 / 1.1	-3.2 / 1.1
P5 / Pr5	0.9 / -0.3	-1.2 / 1.3
P4 / Pr4	-0.6 / -0.1	-0.3 / 0.1
- / Pr3	- / -0.8	- / 1.8

The Im($\chi^{(3)}$) and Re($\chi^{(3)}$) magnitudes for the peak intensity range < 30 MW/cm², calculated using the approach described in [69], are presented in Table 5.4. One can see that in general the TiO₂ NPs incorporation results in a reduction of the cubic NLO response of the KDP matrix. The effect can be attributed to the reduction of the intrinsic defects concentration in the KDP:TiO₂ nanocomposites. The most efficient reduction was observed for the crystals P4 and Pr4.

5.2.3 Optical harmonics generation

The studies of the second harmonic generation were performed. The SH signal dependencies (without phase matching conditions) for the “thick” (~ 1

cm) nominally pure crystals (P, Pr) and KDP:TiO₂ (P4, Pr4) under femtosecond laser excitation at 800 nm are presented in Fig. 5.4 in double logarithmic scale. The measurements were provided for chosen peak laser intensity range 0.4 – 4 GW/cm² that was below the experimentally obtained supercontinuum generation threshold ~ 5 GW/cm² in KDP single crystals at 800 nm.

It was shown that the incorporation of anatase nanoparticles into KDP crystalline matrix leads to a SHG efficiency modification. For the KDP:TiO₂ samples it enhances at about 60% for P and 35% for Pr growth sectors versus the pure KDP crystals within 0.4 – 1.3 GW/cm² pump peak intensity ranges and 0.8 – 2.3 GW/cm² correspondingly (see Fig. 5.7). The difference between P and Pr growth sectors of KDP:TiO₂ crystals can be related to the different TiO₂ NPs concentration (See Table 5.3) [159].

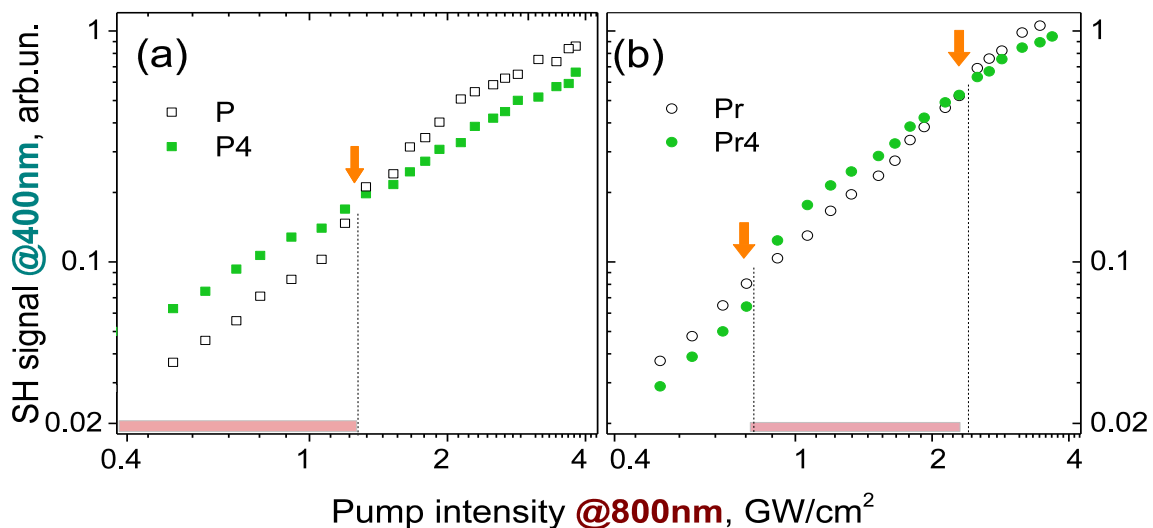


Fig. 5.7 The SHG signal in KDP:TiO₂ single crystals cut from pyramidal (a) and prismatic (b) growth sectors versus the pump peak intensity of femtosecond laser pulses at 800 nm.[68] The dependencies are presented in log-log scale.

The previous SHG studies for the “thick” (~ 1 cm) KDP:TiO₂ crystals within phase-matching conditions under the excitation of picosecond (42 ps) laser pulses at 1064 nm demonstrated [69] about 70% of the SHG efficiency enhancement [56,166]. The effect was explained by the observed internal self-focusing effect in the nanocomposite produced by the giant cubic NLO response of the anatase nanocrystals incorporated into the matrix and its impact on the proton subsystem of the KDP crystal. For the case of the excitation at 800 nm,

the SH wavelength corresponds to the energy state of the KDP matrix intrinsic electronic defects that are related to the interstitial hydrogen atoms H^0 [52]. Observed SHG efficiency enhancement for the P4 and Pr4 crystals can be attributed to the resonant excitation of the defects, being effected by interaction with TiO_2 NPs.

More detailed studies of the spectral response of KDP crystals were performed using a multiphoton microscope (see Chapter 2). At each pumping wavelength the crystals were scanned by the waist of the laser beam. For comparison the signal from the interface air/crystal is used. The emission spectra showing mainly second and third harmonics signals, at different pump wavelengths are presented in Fig. 5.8.

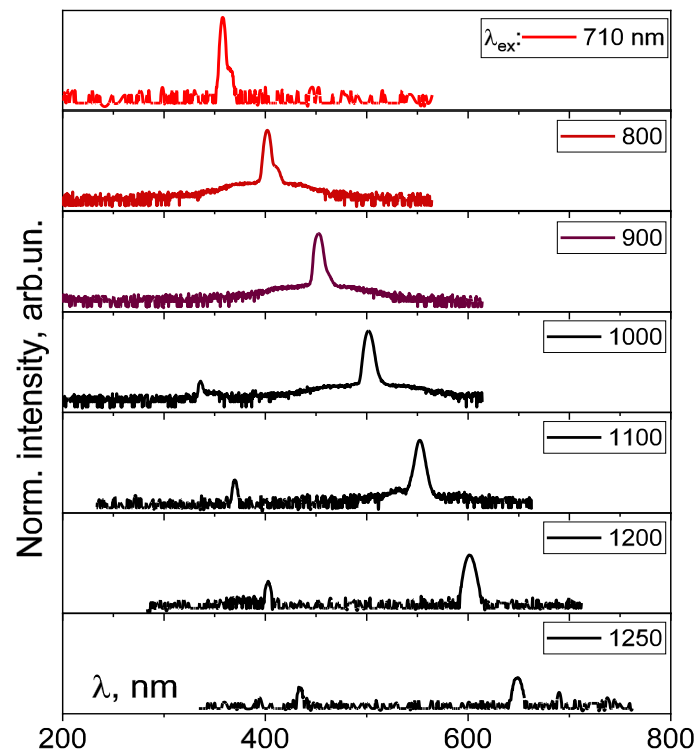


Fig. 5.8 Spectral response of KDP single crystals with incorporated TiO_2 NPs under fs laser excitation at different pump wavelengths(log-scale by intensity).

The studied crystals show high efficiency of second harmonic generation. After normalization of the second harmonic response of the composite crystals by the response of a nominally pure one, we can obtain the spectral efficiency of the harmonic generation enhancement (Fig. 5.9).

Both Pr4 and Pr5 crystals show an enhancement over a wide range of pump wavelengths versus the nominally pure one. Sample with a concentration of 10^{-4} wt.% (Pr4) shows higher efficiency in the excitation range of $\lambda_{\text{ex}} < 850$ nm, whereas sample with a concentration of 10^{-5} wt.% (Pr5) demonstrates a higher SHG efficiency (up to two times) in the range $\lambda_{\text{ex}} > 1000$ nm. Similar difference in NLO response efficiency was observed with self-focusing effect in the mentioned crystals within picosecond pulsed excitation at 1064nm [57]. We suggest that the observed enhancement can be explained by the impact of two factors: (i) manifestation of the efficient photoinduced non-local refractive response of the TiO_2 NPs with perturbed KDP crystal shell domains [55]; (ii) contribution of the intrinsic defects excitation in UV range [52]. The last one is similar to the intrinsic defects contribution into optical harmonics generation enhancement in ZnO bulk crystals (see chapter 4).

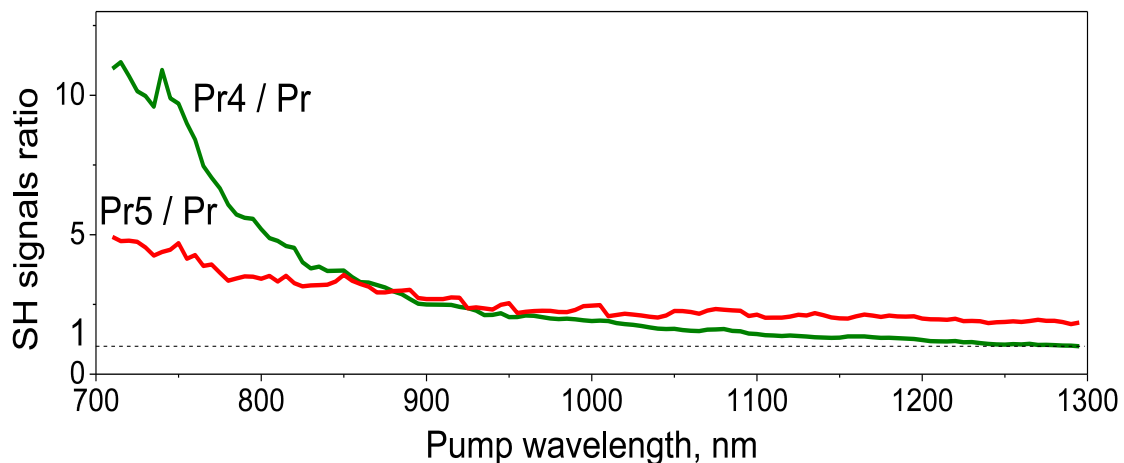


Fig. 5.9 SHG signals ratio for KDP: TiO_2 (samples Pr4 and Pr5) normalized on the response of nominally pure KDP (Pr).

In general, the obtained data show that by optimization of the incorporated NPs concentration it is possible to grow crystals with higher efficiency of harmonics generation in a certain range of wavelengths, that is very important for a practical applications and requires further research.

5.3 Influence of $\text{Al}_2\text{O}_3 \cdot n\text{H}_2\text{O}$ nanofibers incorporation in KDP single crystal on the nonlinear optical response

5.3.1 Elastic optical scattering indicatrix at 532 nm

In order to monitor the impact of the incorporated NOA NFs on the optical quality of the KDP:NOA crystals, the elastic optical scattering indicatrix and extinction losses at 532 nm were studied.

The typical scattering cross-section for nominally pure P and P4 crystals are shown in Fig. 5.10 with solid and dashed lines correspondingly. The propagation direction of the incident laser beam is shown by bold arrow. The sample (S) is located in the center and depicted with dashed rectangle. It can be seen that incorporation of NOA NFs effects on the shape of scattering indicatrix.

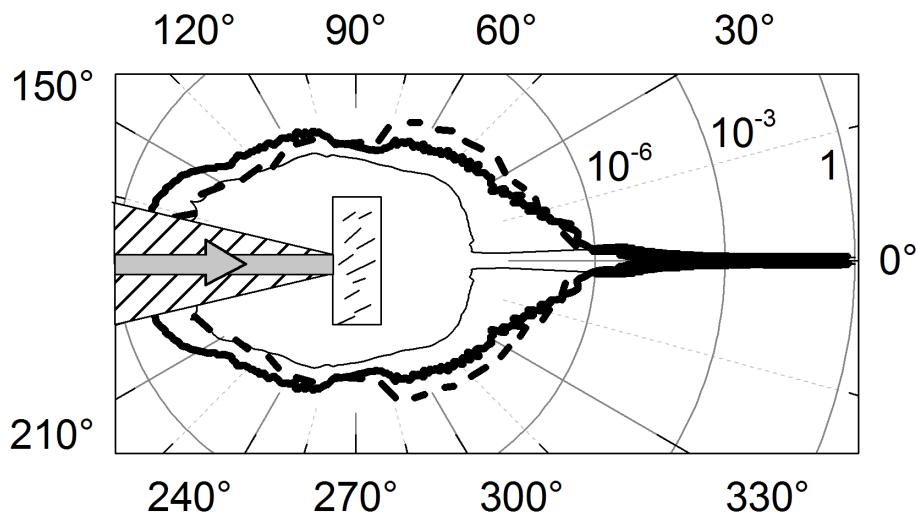


Fig. 5.10 Comparison of the elastic scattering indicatrices at 532 nm for the nominally pure single crystal KDP (P, solid line) with the KDP:NOA (P4, dashed line) one with incorporated NOA nanofibers. Both crystals were cut from the pyramidal growth sector. The indicatrix for the freely propagating laser beam (thin solid line) presented as reference. Hatched area corresponds to the “blind zone” for the data acquisition.

The calculated magnitudes of scattering losses coefficient ε_{scat} for studied single crystals in forward and backward hemispheres are presented in Table 5.5. It is shown that the samples of nominally pure KDP crystal from P and Pr sectors demonstrate different scattering losses. This can be explained by the different impurities concentration in the samples.

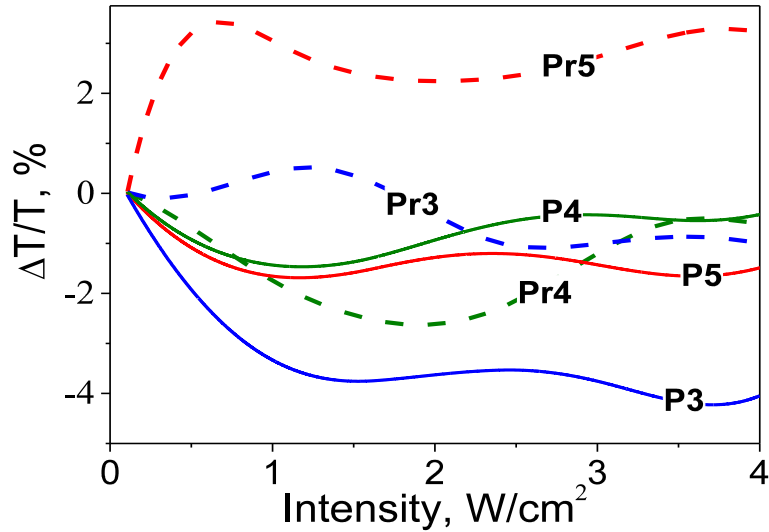


Fig. 5.11 The normalized $\Delta T/T$ photoinduced variations of the on-axis transmittances measured through the finite aperture in the far field for the KDP:NOA crystals cut from pyramidal (P, solid lines) and prismatic (Pr, dashed lines) growth sectors with different concentration of incorporated NOA nanofibers under CW laser excitation at 532 nm.

The incorporation of the NOA NFs results in slight ε_{scat} decrease for the P crystals and significant rise for Pr ones. The obtained magnitudes of scattering losses coefficient in forward hemisphere for P4/Pr4 and P5/Pr5 correlate with the Al concentration in this crystals (see Table 5.5). The observed higher scattering by the samples cut from Pr growth sector can be explained due to the preferential trapping of the NFs by prismatic growth faces. Also there is a slight decrease in backward scattering efficiency in both pyramidal and prismatic growth sectors.

Table 5.5 Scattering losses of the KDP single crystals with incorporated NOA nanofibers cut from different growth sectors in forward and backward hemisphere under CW laser excitation at wavelength 532 nm.

Sample	Conc. Al, $\times 10^{-4}$ wt. %	Forward, %	Backward, %
P / Pr	1.0 / 1.0	0.7 / 1.1	0.2 / 0.5
P5 / Pr5	2.0 / 1.5	0.6 / 1.5	0.1 / 0.3
P4 / Pr4	2.0 / 3.0	0.6 / 3.3	0.2 / 0.5
P3 / Pr3	2.0 / 10.0	1.7 / 3.6	0.2 / 0.3

The obtained results demonstrate the high sensitivity of elastic optical scattering indicatrices at 532 nm to the incorporated NOA NFs concentration in the crystalline matrix. This technique for the KDP:NOA diagnostics in the transparency range has an essential advantage versus the UV range spectral analysis due to the absence of the polyvalent metals impurities contribution to the scattering response.

A similar general tendency was observed for the scattering extinction at 532 nm in the KDP:TiO₂ single crystals with incorporated TiO₂ NPs [164]. The main difference between the KDP:TiO₂ and the KDP:NOA crystals is that the TiO₂ NPs incorporated preferentially into the P growth sector [57] while the NOA NFs – into the Pr one. An increase of the incorporated metal oxides causes a rise of the scattering losses in the forward hemisphere. The extinction is higher for the KDP:NOA crystals due to the more efficient incorporation of the NOA NFs versus TiO₂ NPs and form factor of NOA NFs.

Table 5.6 The real and imaginary parts of the cubic nonlinear optical susceptibility $\chi^{(3)}$ and the *FOM* parameter for nominally pure KDP and KDP:NOA single crystals under CW laser excitation ($\lambda = 532$ nm). The relative error of the $\chi^{(3)}$ magnitude estimation does not exceed 5%.

Sample	Re($\chi^{(3)}$), $\times 10^{-4}$ esu	Im($\chi^{(3)}$), $\times 10^{-4}$ esu	<i>FOM</i>
P / Pr	8.1 / 7.1	0.26 / 0.22	0.8 / 0.9
P5 / Pr5	2.1 / 17.0	0.03 / 0.02	1.8 / 22.5
P4 / Pr4	2.7 / 3.1	-0.02 / 0.01	3.5 / 8.2
P3 / Pr3	-3.2 / 7.2	-0.08 / -0.02	1.1 / 9.5

5.3.2 Self-action of the CW laser radiation at 532 nm

The NLO diagnostics of the KDP:NOA crystals was performed by studying of the self-action of the CW laser radiation at 532 nm (2.33 eV) that is in resonance with native defects of the nominally pure KDP matrix [52].

The normalized photoinduced on-axis transmittance variations $\Delta T/T = (T - T_0)/T_0$ (where T is the on-axis transmittance of KDP:NOA sample and T_0 is the on-axis transmittance of nominally pure KDP crystal) of the KDP:NOA crystal under CW laser excitation ($\lambda = 532$ nm) are presented in Fig. 5.11. The rate $\Delta T/T$ characterizes the contribution of the NOA NFs subsystem to the photoinduced refractive index variations Δn of the nanocomposite.

It is shown that the presented dependencies are not monotonic: the sign of the Δn vary within the laser intensity. The most efficient Δn variations were observed for the range 0.1-1.1 W/cm². NOA incorporation in the P growth sector causes a decrease of the refractive NLO response magnitude in comparison with nominally pure crystal. In the case of the crystals cut from Pr growth sector the sign and magnitude of the Δn significantly depends on the NOA NFs concentration. It leads to the increase of the refractive NLO response magnitude for the samples Pr5 and Pr3, and decrease for the Pr4 in comparison with pure KDP.

In order to characterize the observed NLO response of nominally pure KDP and KDP:NOA crystals the $\text{Im}(\chi^{(3)})$ and $\text{Re}(\chi^{(3)})$ magnitudes were calculated and summarized in Table 5.6. One can see that for the nominally pure KDP crystal the NLO parameters are ~15 % higher in P growth sector. For the samples P5 and P4, a correlation between $\text{Re}(\chi^{(3)})$ and the NOA concentration (see Table 5.2) was observed.

It should be noted that the $\text{Re}(\chi^{(3)})$ magnitudes are about two order higher versus the $\text{Im}(\chi^{(3)})$ that indicates high optical quality of the nanocomposites. The estimated figure of merit for studied samples – the rate of the photoinduced refractive index variations to the absorptive ones at the given wavelength $FOM = \Delta n/\lambda\Delta\alpha$ - are presented in Table 5.6. One can see that FOM for nanocomposites KDP:NOA exceeds the corresponding magnitudes for nominally pure KDP crystals. The highest FOM was observed for the Pr5 sample with 10⁻⁴ wt% of the NOA NFs.

The obtained results agree with the ones observed for the KDP:TiO₂ nanocomposites under CW excitation at 532 nm [167]. As in KDP:NOA, the incorporation of the TiO₂ NPs resulted in a photoinduced refractive index reduction for the crystals from P growth sector and a Δn rise for the Pr ones. This similar trends for the same growths sectors in spite of the different NPs/NFs incorporation indicate a dominant impact of the crystal growth sector on the macroscopic NLO response of the nanocomposite systems under CW laser excitation. This effect can be explained by the excitation of the KDP crystal native defects and their interaction with the incorporated nanostructured metal oxides subsystem.

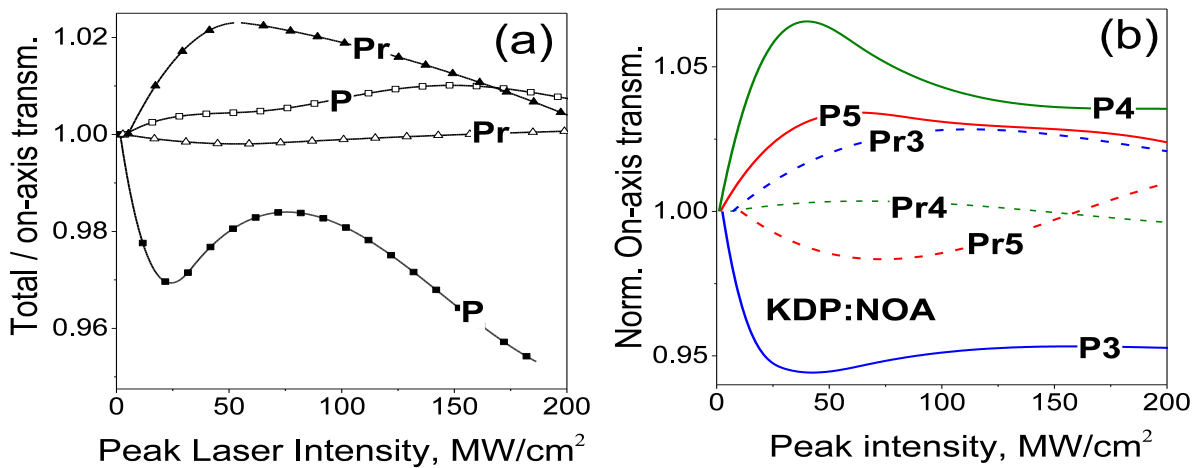


Fig. 5.12 (a) The photoinduced variations of the total (white scatters) and on-axis (black scatters) transmittances of the nominally pure KDP matrix under pulsed laser excitation ($\tau = 30$ ps, $\lambda = 532$ nm) [4], where closed circles and solid line corresponds to the crystals cut from pyramidal (P) growth sector, open circles – from the prismatic (Pr) one; (b) the photoinduced variations of the on-axis transmittance for KDP crystals cut from pyramidal (P, solid lines) and prismatic (Pr, dashed lines) growth sectors with different concentrations of incorporated NOA nanofibers under pulsed laser excitation ($\tau = 30$ ps, $\lambda = 532$ nm)

The experimental results show a correlation between the NOA NFs concentration and the CW radiation self-action effects efficiency. The proposed approach can be used as express method for KDP:NOA crystals diagnostics. Furthermore, the observed NLO parameters for the crystals from P growth sector are in a good agreement with the scattering losses coefficient ϵ_{scat} . It

indicates the interest of the simultaneous application of both methods for more precise KDP:NOA nanocomposites characterization.

5.3.3 Self-action of picosecond laser pulses at 532 nm

The NLO properties of KDP and KDP:NOA crystals were studied within the self-action of picosecond laser pulses at 532 nm. It was shown that even the nominally pure KDP matrix exhibit different NLO response in P and Pr growth sectors. As it can be seen from the on-axis transmittance dependencies in Fig. 5.12a for the sample P the self-defocusing effect $\Delta n(P) < 0$ was observed versus the self-focusing one $\Delta n(Pr) > 0$ in the Pr one. The effects were accompanied by a slight photoinduced variations of the optical absorption $\Delta\alpha(Pr) > 0$ and $\Delta\alpha(P) < 0$. Also it is very important to take this distinct response into account during the fabrication of wide aperture frequency converters. In order to prevent laser beam spatial and phase profiles distortion, the converter should be cut from the same growth sector.

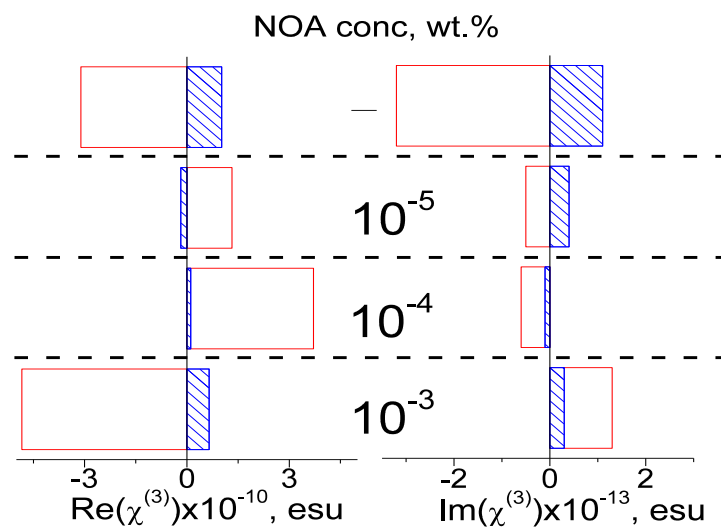


Fig. 5.13 Comparison of the cubic NLO susceptibility real $\text{Re}(\chi^{(3)})$ and imaginary $\text{Im}(\chi^{(3)})$ parts magnitudes versus the NOA nanofibers concentration in mother liquor for P (blank bars) and Pr (hatched bars) growth sectors of the KDP single crystals under pulsed laser excitation ($\tau = 30$ ps, $\lambda = 532$ nm) [4].

It should be noted that the observed on-axis transmittance dependencies are not monotonic and can be characterized by the value of the peak laser intensity I_s that corresponds to the refractive NLO response sign change. The I_s values for the studied crystals are shown in Table 5.7.

The incorporation of the NOA NFs into to the KDP matrix effects in significant the NLO response modification (Fig. 5.12b). The efficiency of the processes significantly depends on the NOA NFs concentration. From the obtained dependencies, the $\text{Re}(\chi^{(3)})$ and $\text{Im}(\chi^{(3)})$ magnitudes were estimated for the peak laser intensity range $I < I_s$. The results are presented as a bar diagram in Fig. 5.13.

One can see that in general $\text{Re}(\chi^{(3)})$ for the P samples are about 4 times higher versus the ones from Pr growth sector. The incorporation of NOA NFs leads to the decrease of the refractive NLO response for the Pr crystals and significant enhancement in P crystals. The most efficient positive $\Delta n \sim 10^{-4}$ ($\text{Re}(\chi^{(3)}) \sim 3.7 \cdot 10^{-10}$ esu) was observed for the sample P4 with the NFs concentration 10^{-4} wt% in the growth solution. This effect leads to a strong laser beam self-focusing in bulk KDP:NOA crystal that could result in SHG efficiency enhancement. It can be similar to the observed SHG efficiency increase in nanocomposite KDP:TiO₂ single crystals [56].

Table 5.7 Real and imaginary parts of the cubic nonlinear optical susceptibility and *FOM* parameter for KDP:NOA crystals under picosecond laser excitation ($\lambda = 532$ nm). The relative error of the NLO response data is about 10%.

Sample	I_s , MW/cm ²	$\text{Re}(\chi^{(3)})$. $\times 10^{-11}$, esu	$\text{Im}(\chi^{(3)})$ $\times 10^{-13}$, esu	<i>FOM</i>
P / Pr	24.4 / 55.3	-30.1 / 10.0	-3.2 / 1.1	25.8 / 24.6
P5 / Pr5	61.8 / 72.7	13.0 / -2.0	-0.5 / 0.4	70.0 / 1.2
P4 / Pr4	40.2 / 66.1	37.0 / 1.0	-0.6 / -0.1	163.9 / 29.2
P3 / Pr3	42.5 / 112.2	-48.0 / 7.0	1.3 / 0.3	98.7 / 57.4

The calculated $\text{Im}(\chi^{(3)})$ and $\text{Re}(\chi^{(3)})$ magnitudes and FOM parameter for the range $I < I_s$ are summarized in the Table 5.7. One can see that NFs incorporation results in a reduction of $\text{Im}(\chi^{(3)})$ for the KDP:NOA crystals in the range $I < I_s$. It should be stated that the absorptive NLO response efficiency is

higher for the P samples. It can be attributed to a lower number of impurities in nominally pure matrix and lower NOA NPs concentration in the bulk of nanocomposites. For the range $I > I_s$ the NOA NPs incorporation results in a change of $\text{Re}(\chi^{(3)})$ sign for the P samples from and an increase for the Pr ones. In contrast to the $I < I_s$ range, the $\text{Im}(\chi^{(3)})$ magnitude increases for the crystals Pr5 and Pr4.

It is known that excitation wavelength 532 nm is overlapped with the native defects bands of (i) *F*-type centers in the NOA [168], and (ii) localized and self-trapped hole polarons in the nominally pure KDP crystals [52]. The pronounced refractive NLO response sign change could be due to the nonlocal response of the excited NFs interface states “dressed” with redistributed hydrogen bonds framework of the KDP smart matrix. It saturates with the excitation level increase. This assumption needs further verifications but was observed in KDP:TiO₂ at 1064 nm [4].

As in CW excitation regime, for the pulsed one the studied crystals demonstrate high *FOM* parameter (see Table 5.7). The magnitudes are similar for the nominally pure crystals. The highest *FOM* was observed for the KDP:NOA with 10⁻⁴ wt% NOA NFs cut from P growth sector. The obtained result along with the mentioned efficient refractive NLO response manifestation shows that this nanocomposite is very promising for frequency converters applications.

5.3.4 Second Harmonic Generation

A preliminary study of the SHG efficiency enhancement in Z-cut KDP:NOA single crystals P4 and Pr4 (NOA concentration 10⁻⁴ wt.% in the growth solution) versus the corresponding nominally pure KDP P and Pr crystals of the same thickness was performed at pumping wavelength of 1064 nm and 1ns pulses duration without phase matching conditions.

The 0.7 mm thin crystals were positioned in the waist of the focused pump beam and it was performed fine adjustment of the samples position and angle to get the maximum of the SH signal. It means that the measured SH

signal is determined by the intrinsic conversion efficiency in the crystal. The obtained results for the generated SH signals in the KDP:NOA versus the KDP crystals for the different pump peak intensities are presented in Fig. 5.14.

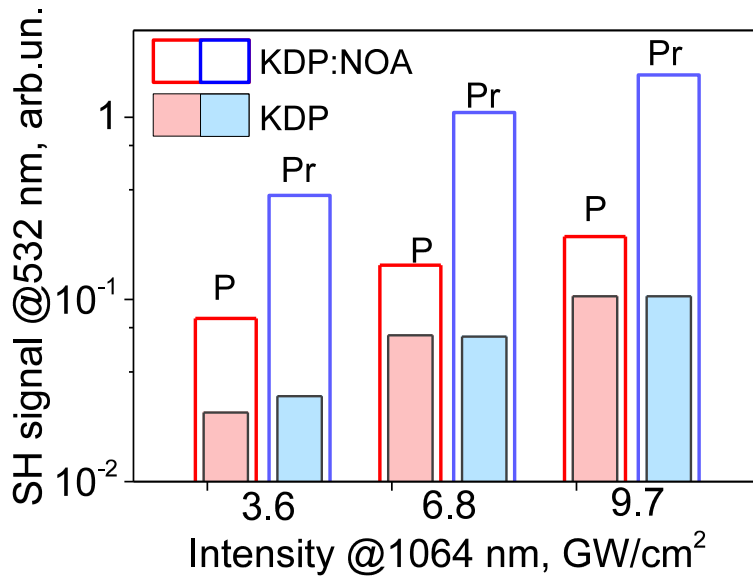


Fig. 5.14 The SHG signal in nominally pure KDP single crystal (filled bars) and KDP:NOA (blanc bars) cut from pyramidal (P) and prismatic (Pr) growth sectors at the different peak intensities of the pump laser pulses at 1064 nm. The NOA NFs concentration was 10^{-4} wt% in the growth solution [4].

Analysis of the data has shown an enhancement of the SHG process in the KDP crystals with incorporated NOA NFs versus the nominally pure KDP. The SH signal rise in Pr4 gained ~15-17 times vs Pr while in P4 it was ~2.0-2.5 vs P. The SH signal in the Pr4 was 5-8 times higher the similar in the P4 while it was about the same in the Pr and in the P nominally pure crystals. More efficient SH response in the prismatic growth sector versus the pyramidal one corresponded to the higher NOA concentration in the crystals bulk (see Table 5.5). These results are consistent with the observed efficient photoinduced refractive index variation $|\Delta n| \sim 10^{-4}$ due to the picosecond range pulsed laser radiation self-action at 532 nm.

5.4 Influence of KDP single crystals doping by L-arginine on NLO response efficiency

The NLO properties of KDP and KDP:L-arg single crystals were studied within the self-action of picosecond laser pulses at 1064 nm. The photoinduced

variations of the total and on-axis transmittances versus the peak intensity for the samples are presented in Fig. 5.15 a) and b) correspondingly.

It was shown that, in general, for the nominally pure crystals from P and Pr growth sectors the total transmittance variations do not exceed 0.5 %. For the initial peak intensity range both samples demonstrate slight photodarkening effect that is more pronounced for the one from P growth sector. For a definite laser intensity I_t the effect saturates (see Table 5.8) and turns to photobleaching. The observed higher I_t magnitudes for the crystal from Pr growth sector can be explained by its higher thickness. The incorporation of L-arginine dopant results in significant enhancement of the photodarkening efficiency and higher I_t . For composite crystals, I_t was determined as tangents intersection point (see Fig. 5.15a) that can be treated as a switching threshold from the initial effective response to a more saturated one.

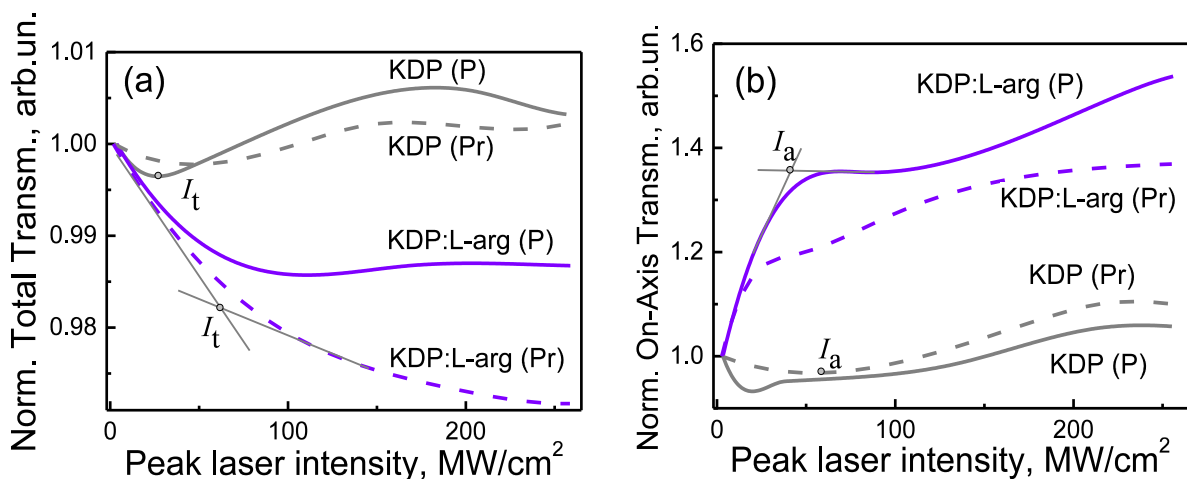


Fig. 5.15 Photoinduced variations of the total (a) and on-axis (b) transmittances of the KDP and the KDP:L-arg single crystals cut from pyramidal (P) and prismatic (Pr) growth sectors under pulsed laser excitation at 1064 nm.

The refractive NLO response of the crystals was studied by the on-axis transmittance dependencies measurements versus the peak laser intensity. It was shown that even for both nominally pure samples the magnitudes of the photoinduced on-axis transmittance variations are significantly higher versus the absorptive ones. The nominally pure matrices demonstrate the self-defocusing effect that saturates at peak intensity I_a . The L-arg doping results in one order of magnitude enhancement of the refractive NLO response and its sign change to

self-focusing effect that is more pronounced $\sim 50\%$ for the KDP:L-arg crystal from P growth sector versus the $\sim 30\%$ for the one from Pr growth sector. The saturation occurs at a lower peak intensity I_a in comparison to I_t observed with the total transmittance dependencies. It indicates the resonant origin of the studied processes in the crystals.

Table 5.8 Comparison of the refractive $\text{Re}(\chi^{(3)})$ and absorptive $\text{Im}(\chi^{(3)})$ cubic nonlinear optical responses efficiencies and the quality parameter FOM for the KDP:L-arg and the nominally pure KDP single crystals in the peak intensity range $I < 30 \text{ MW/cm}^2$. L - sample thickness, I_t and I_a – the saturation peak intensity and on-axis transmittance extremum position, see Fig. 5.15.

Sample	Growth Sector	L , mm	I_t/I_a , MW/cm^2	$\text{Re}(\chi^{(3)})$, 10^{-9} esu	$\text{Im}(\chi^{(3)})$, 10^{-12} esu	FOM
KDP	P	0.49	27 / 18	-2.9	1.2	64.0
	Pr	0.82	47 / 54	-0.7	0.3	61.8
KDP:L-arg	P	0.54	57 / 42	12.0	1.9	167.4
	Pr	0.54	63 / 23	11.0	2.0	145.8

From the obtained total and on-axis transmittance dependencies the imaginary $\text{Im}(\chi^{(3)})$ and real $\text{Re}(\chi^{(3)})$ parts of the cubic NLO susceptibility (see Table 5.8) were calculated according to the route described in chapter 2 for initial peak intensity range $I < 30 \text{ MW/cm}^2$. It is shown that doping the crystals with L-arg dopant results in a significant enhancement of the absorptive and refractive NLO responses: $|\text{Re}(\chi^{(3)})_{\text{KDP:L-arg}}| \sim 4.1 \cdot |\text{Re}(\chi^{(3)})_{\text{KDP}}|$ and $|\text{Im}(\chi^{(3)})_{\text{KDP:L-arg}}| \sim 1.6 \cdot |\text{Im}(\chi^{(3)})_{\text{KDP}}|$ for P growth sector; $|\text{Re}(\chi^{(3)})_{\text{KDP:L-arg}}| \sim 15.7 \cdot |\text{Re}(\chi^{(3)})_{\text{KDP}}|$ and $|\text{Im}(\chi^{(3)})_{\text{KDP:L-arg}}| \sim 6.7 \cdot |\text{Im}(\chi^{(3)})_{\text{KDP}}|$ for Pr growth sector. This $\text{Re}(\chi^{(3)})$ increase and sign change to self-focusing in comparison to the nominally pure KDP matrix is similar to the one observed in KDP:TiO₂ nanocomposites [48,56]. For the others ranges, the NLO response enhancement is lower due to the saturation of the aforementioned effects. The exception is the

KDP:L-arg crystal from P growth sector for which in the range 40-50 MW/cm² we obtained $|\text{Re}(\chi^{(3)})_{\text{KDP:L-arg}}| \sim 14.5 \cdot |\text{Re}(\chi^{(3)})_{\text{KDP}}|$.

For the initial range we also calculated the figure of merit $\text{FOM} = \Delta n / (\lambda \Delta \alpha)$, see Table 5.8. The parameter reflects the gain in photoinduced refractive index versus the resonant absorption losses at the corresponding wavelength. It was shown that for the L-arginine doped KDP crystals the FOM magnitudes are about 2.5 times higher. It means that KDP:L-arg are promising nonlinear optical material for the laser and photonics applications due to the obtained high FOMs magnitudes.

It is known that the doping of the KDP crystals with complex organic molecules like L-arginin and L-vanilin results in SHG efficiency enhancement up to 30-70% that proportionally rises with the concentration of the organic compounds in the KDP [169]. A SHG efficiency enhancement up to 30% in the KDP with 2 wt% of carbamide was shown in [2]. This effect was assumed to be related to the additional deformation of $(\text{PO}_4)^{3-}$ tetrahedron due to the hydrogen bonds formation between the amino group of carbamide and hydrophosphate group of the crystalline matrix. In recent studies it was demonstrated that organic compounds (carbamide, xelenole orange) result in significant enhancement of $(\text{PO}_4)^{3-}$ phosphate groups oscillations anharmonism of the KDP crystal and consequently in efficient rise of nonlinear coefficient d_{36} that determines high efficiency of quadric NLO response $\text{Re}(\chi^{(2)})$ [170].

To summarize, the observed efficient self-focusing effect due to the L-arg incorporation is similar to the one observed for KDP:TiO₂ nanocomposites [48,56]. It was shown that incorporation of metal oxide nanoparticles into the crystalline KDP matrix under definite excitation condition leads to the giant enhancement of the cubic NLO response $\text{Re}(\chi^{(3)})$. The effect results in intrinsic self-focusing of the pump laser beam that determines concentration of the laser radiation within an enhancement of the optical harmonics generation processes efficiency. Thus the KDP:L-arg crystal is promising medium for the laser frequency conversion due to the manifestation of both quadratic (direct impact)

and degenerate cubic refractive (indirect impact through the self-focusing effect) responses enhancement

Conclusions to the chapter 5

- 1) It was shown the reduction of the scattering losses at 1064 nm in forward hemisphere due to the TiO₂ NPs incorporation at concentrations 10⁻⁵-10⁻⁴ wt.% in pyramidal growth sector versus the nominally pure KDP matrix. The effect was explained by lower concentration of non-controlled impurities in the crystals with TiO₂ NPs.
- 2) A second harmonic generation efficiency enhancement was demonstrated for the KDP:TiO₂ crystals under *fs* laser excitation at 800 nm: up to 60% for pyramidal and 35% for prismatic growth sectors versus the nominally pure KDP matrix.
- 3) A correlation of the scattering losses at 532 nm with the NOA NPs concentration in the prismatic/pyramidal growth sectors of the crystals was shown. The observed higher scattering by the crystals from prismatic growth sector was explained due to the preferential trapping of the NPs by Pr growth sector.
- 4) One order of magnitude enhancement of the second harmonic generation efficiency was obtained in the KDP:NOA single crystals versus the nominally pure KDP ones within *ns* laser excitation at wavelength 1064 nm. It is correlated with the efficient photoinduced refractive index variation $|\Delta n| \sim 10^{-4}$ due to the picosecond range pulsed laser radiation self-action at 532 nm.
- 5) The enhancement of the nonlinear optical response was demonstrated for KDP single crystals with L-arg dopant under *ps* laser excitation at 1064 nm. It was showed that the L-arg dopant induces a self-focusing effect stronger than one observed for the nominally pure KDP matrix. The efficiency of the refractive NLO response $\text{Re}(\chi^{(3)}) \sim 10^{-8}$ esu is one order of magnitude higher for the KDP:L-arg single crystals. The observed efficient self-focusing effect can provide laser electric field concentration with consequent enhancement of the SHG yield.

General Conclusion

The main conclusions of the thesis as a result of research project are listed below:

1) For the first time an interface scanning technique for the third harmonic generation efficiency analysis was applied on HNPs colloidal suspensions, this technique being primarily designed to study nonlinear response of liquids and gases. Presented technique was applied to analyze the third harmonic generation efficiency of ZnO HNPs colloidal suspensions under nanosecond range pulsed laser excitation at 1064 nm. It was estimated the non-degenerate orientation-averaged cubic nonlinear optical susceptibility of the ZnO NPs with sizes in range 40-150 nm to be about $\langle |\chi_{NPs}^{(3)}(3\omega = \omega + \omega + \omega)| \rangle \sim 10^{-18} \text{ m}^2/\text{V}^2$. Comparison of the THG efficiencies was performed using two techniques (i) interface scanning at TH and (ii) hyper-Rayleigh scattering from the colloid bulk. It was shown consistency of both approaches and correspondence of the efficient $\langle \chi_{NPs}^{(3)} \rangle$ magnitudes to the bulk ZnO response.

2) In order to study the response of the individual HNPs, a prototype of multiphoton microscope was designed with a femtosecond laser excitation with a pump range of 710-1300 nm. For ZnO NPs with a size <150 nm it was shown specific excitation ranges with high efficiency for the different processes: $\lambda_{\text{ex}} < 800 \text{ nm}$ for SH, $800 < \lambda_{\text{ex}} < 950 \text{ nm}$ for PL, and $950 < \lambda_{\text{ex}} < 1200 \text{ nm}$ for TH. The mechanism of harmonics generation enhancement involves the contribution of intrinsic defects. These results are promising and shows the interest of single NP spectroscopy based on a multiphoton microscopy.

3) For the analysis of different types of optical responses of ZnO NPs, the NLO diagnostics of bulk ZnO single crystals with different content of defects was performed. It is shown that an obtained magnitudes of the real and imaginary parts of the cubic NLO susceptibility correlate with the data of PL and IR spectroscopy in the area of defective bands. Also it was demonstrated the sensitivity of the elastic optical scattering to the concentration of defects.

4) The prospects of enhancement of the optical harmonics generation efficiencies in KDP single crystals due to incorporation of metal oxides NPs were studied. In particular, it was shown that the incorporation of TiO_2 gives an increase of the SHG efficiency in KDP: TiO_2 crystals by 60/35 % for the pyramidal/prismatic growth sectors under *fs* laser pulses excitation at 800 nm. Also, a 10 times increase of the SHG was demonstrated for KDP:NOA in comparison with nominally pure KDP crystal under *ns* laser pulses excitation at 1064 nm.

5) A device for analyzing the cross section of the elastic optical scattering indicatrices under continuous laser excitation was designed. The device was tested on a wide class of objects, in particular for nominally pure KDP single crystals, it was shown that the elastic optical scattering losses at 1064 nm is lower than for KDP: TiO_2 crystals with incorporated TiO_2 NPs due to the lower concentration of uncontrolled impurities. It was shown that optical scattering losses in a KDP:NOA single crystal depends on NOA nanofibers concentration. For ZnO single crystals, high optical scattering sensitivity to defect content was shown due to high polarizability of defective states and an effective refractive response of photoinduced delocalized carriers.

Among the experimental results presented in this work, the most interesting were obtained with the multiphoton microscope designed during the last few months of my PhD. It allows to study the efficiency of SH, TH and PL from single NPs in wide spectral range of excitation.

Further work should be focused on the increasing of the precision of measurements for revealing of the full potential of this setup. First of all, a simultaneous analysis of the spectral response in forward and backward direction should be realized. It will allow to study the influence of size and shape of NPs on the harmonics generation efficiency. Additional studies of the elastic light scattering with this setup will simplify the task of the NPs agglomerates identification that will significantly improve the experimental

protocol and the quality of the data. It is also important to design an additional registration unit for the analysis of the photoinduced absorption impact on the data.

Another issue that has not been developed in this work is how to separate optical harmonics generation and PL under the resonant excitation, when both signals spectrally overlap. This can be done by the analysis of the signal response time, which is very different for PL and harmonics generation. For this, high-speed acquisition could be implemented using for instance a photon counting unit at the output of the spectrometer.

Using this improved experimental setup could help to perform nonlinear spectroscopy at the single NP level with better accuracy. Our preliminary results show the high sensitivity of this experimental technique to the energy levels structure of the studied materials. In the future, we hope to reconstruct this structure with higher precision than with conventional PL spectroscopy.

More generally, this experimental system will allow to characterize the nonlinear properties of new harmonic nanoparticles and provide feedback for their improvement and for designing advanced high-efficient materials for a wide range of practical applications.

Publications list

- 1*. Photoinduced refractive index variation within picosecond laser pulses excitation as the indicator of oxyorthosilicates single crystals composition modification / Uklein A. V., Popov A. S., Multian V. V., Brodyn M. S., Kononets V. V., Sidletskiy O. T., Gayvoronsky V. Ya. // *Nanoscale Research Letters*, 2015. Vol. 10., №. 1. P. 102 (7pp).
- 2*. Nonlinear optical response of nanocomposites based on KDP single crystal with incorporated $\text{Al}_2\text{O}_3 \cdot n\text{H}_2\text{O}$ nanofibriles under CW and pulsed laser irradiation at 532nm / Popov A. S., Uklein A. V., Multian V. V., Dantec R., Pritula I. M., Gayvoronsky V. Ya., Kostenyukova E. I., Bezkravnaya O. N. // *Optics Communications*, 2016. Vol. 379. P. 45–53.
- 3*. Characterization of oxidized carbon materials with photoinduced absorption response / Uklein A. V., Multian V. V., Diyuk V. E., Grishchenko L. M., Lisnyak V. V., Gayvoronsky V. Ya., Kozhanov V. O., Boldyrieva O. Y. // *Applied Physics B*. 2016. Vol. 122. P. 287-295.
- 4*. Optical properties of thin nanosilicon films / Buchenko V. V., Multian V. V., Rodionova T. V., Goloborodko A. A., Uklein A. V., Gayvoronsky V. Ya., Sutyagina A. S. // *Optical Materials*. 2016. Vol. 62. P. 612–620.
- 5*. Synthesis, characterization, luminescent and nonlinear optical responses of nanosized ZnO / Multian V. V., Uklein A. V., Zaderko A. N., Kozhanov V. O., Lisnyak V. V., Gayvoronsky V. Ya., Boldyrieva O. Y., Linnik R. P. // *Nanoscale Research Letters*. 2017. Vol. 12, №. 1. P. 164 (8pp).
- 6*. Nonlinear optical response of the KDP single crystals with incorporated TiO_2 nanoparticles in visible range: effect of the nanoparticles concentration / Popov A. S., Uklein A. V., Multian V. V., Pritula I. M., Khasanov O., Gayvoronsky V. Ya., Budnyk P. I. // *Functional Materials*. 2017. Vol. 24. P. 5–10.
- 7*. Effect of L-arginine additive on the growth and physical properties of potassium dihydrogen phosphate single crystals / Kostenyukova E. I., Uklein A. V., Multian V. V., Pritula I. M., Bezkravnaya O. N., Doroshenko A. G., Khimchenko S. V., Fedorov A. G., Levchenko A. N., Starikov A. I., Gayvoronsky V. Ya. // *Functional materials*. 2018. Vol. 25. P. 246–257.
- 8*. Multian V.V., Dantec R., Gayvoronsky V.Ya., Characterization of colloidal nanoparticle suspensions using the third harmonic generation at interfaces // *Ukrainian Journal of Physical Optics*. 2018. Vol. 19. P. 92–98.
- 9*. Nonlinear optical response of bulk ZnO crystals with different content of intrinsic defects / Uklein A. V., Multian V. V., Kuz'micheva G. M., Linnik R. P., Lisnyak V. V., Popov A. I., Gayvoronsky V. Ya. // *Optical Materials*. 2018. Vol. 84. P. 738–747.
- 10*. Averaged third-order susceptibility of ZnO nanocrystals from third harmonic generation and third harmonic scattering / Multian V. V., Riporto J.,

Urbain M., Mugnier Y., Djanta G., Beauquis S., Galez C., Gayvoronsky V. Ya., Dantec R. // *Optical Materials*. 2018. Vol. 84. P. 579–585.

11*. Second harmonic spectroscopy of ZnO, BiFeO₃ and LiNbO₃ nanocrystals / Riporto J., Multian.V.V., Gayvoronsky V.Ya., Dantec R. et al. // *Optical Materials Express*. 2019. Vol. 9. No. 4 P. 1955–1966

Conferences:

1**. The effect of sintering temperature on linear and nonlinear optical properties of YAG nanoceramics. Nanocomposites, Nanophotonics / Gayvoronsky V.Ya., Popov A.S., Brodyn M.S., Uklein A.V., Multian V.V., Shul'zhenko O.O. // *Nanobiotechnology, and Applications, Eddition Springer Proceedings in Physics 156, Chapter: 13, Publisher: Springer International Publishing Switzerland 2015, Eds: O. Fesenko, L. Yatsenko, 2014. – P.147-164.*

2**. New evidence of non-Rayleigh type of light scattering in silicon nanowire arrays formed by metal-assisted chemical etching / Efimova A. I., Tkachev A.V., Gonchar K.A., Osminkina L.A., Multian V.V., Gayvoronsky V.Ya. // *Porous Semiconductors - Science and Technology – Alicante-Benidorm (Spain) 2014. – P. 40.*

3**. Nonlinear optical characterization of the KDP single crystals with incorporated titania, alumina and zirconia nanoparticles / Uklein A.V., Popov A.S., Multian V.V., Dantec R., Brodyn M.S., Gayvoronsky V.Ya. // *NANO-2014, – Yaremche, Lviv (Ukraine) 2014. – P. 45.*

4**. Impact of point defects concentration in bulk-ZnO single crystals on self-action of picosecond laser pulses / Gayvoronsky V.Ya., Uklein A.V., Multian V.V., Kuz'micheva G.M., Moskina A., Eglitis R.I. // *The Fifth International Workshop on Advanced Spectroscopy and Optical Materials – Gdańsk (Poland) 2015. – P. 108.*

5**. Self-action effects manifestation in harmonic nanoparticles colloids / Multian V.V., Uklein A.V., Dantec R., Mugnier Y., Brodyn M.S., Gayvoronsky V.Ya. // *NANO-2015 – Lviv (Ukraine) 2015. – P. 337.*

6**. Effect of Aluminum Oxyhydroxide Nanoparticles Incorporation on Nonlinear Optical Response of the KDP Single Crystals / Popov A.S., Uklein A.V., Multian V.V., Pritula I.M., Brodyn M.S., Gayvoronsky V.Ya. // *NANO-2015, – Lviv (Ukraine) 2015. – P. 349.*

7**. Nonlinear optical response of ZnO scintillator crystals under picosecond laser excitation / Uklein A.V., Multian V.V., Kuz'micheva G.M., Popov A.I., Moskina A., Gayvoronsky V.Ya. // *LUMDETR 2015 – Tartu (Estonia) 2015. – P. We-P-15.*

8**. Characterization of the nonlinear optical properties of harmonic nanoparticles / Multian V.V., Uklein A.V., Dantec R., Mugnier Y., Brodyn M.S., Gayvoronsky V.Ya. // *NANO-2016 – Lviv (Ukraine) 2016. – P. 389.*

9**. Nonlinear optical characterization of the KDP single crystals with

incorporated titania nanoparticles of different crystallographic modifications / Popov A.S., Multian V.V., Uklein A.V., Kuz'micheva G.M., Pritula I.M., Gayvoronsky V.Ya. // NANO-2016 – Lviv (Ukraine) 2016. – P. 403.

10**. The correlation of photoinduced total transmission with the degree of the surface functionalization of carbons obtained from natural renewable sources / Diyuk V.E., Grishchenko L.M., Kozhanov V.O., Lisnyak V.V., Uklein A.V., Multian V.V., Gayvoronsky V.Ya. // Ukr. J. Phys. 61, 2016. – P. 863-872.

11**. Nonlinear optical analysis of bulk oxidized carbonaceous materials response / Uklein A.V., Multian V.V., Grishchenko L.M., Diyuk V.E., Lisnyak V.V., Gayvoronsky V.Ya. // CAOL *2016 – Odessa (Ukraine) 2016. – P. 51.

12**. Third-order nonlinear susceptibility of ZnO nanoparticles using third-harmonic generation at interfaces / Multian V.V., Riporto J., Mugnier Y., Dantec R., Gayvoronsky V.Ya. // NANO-2017 – Migove-Chernivtsi region (Ukraine) 2017. – P. 52.

13**. The optical properties and nonlinear optical response of nanosized ZnO / Uklein A.V., Multian V.V., Boldyrieva O., Lisnyak V.V., Gayvoronsky V.Ya. // NANO-2017 – Chernivtsi (Ukraine) 2017. – P. 33.

14**. Surface Response of Brominated Carbon Media on Laser and Thermal Excitation: Optical and Thermal Analysis Study / Multian V.V., Kinzerskyi F.E., Mischanchuk O.V., Kozhanov V.O., Lisnyak V.V., Gayvoronsky V.Ya. // Nanoscale Research Letters. –2017. –Vol. 12, No. 1. –P. 146. (8pp).

15**. Impact of water adsorption on nonlinear optical properties of functionalized porous silicon / Uklein A.V., Multian V.V., Oliinyk B.V., Doroshchuk V.V., Alekseev S.A., Lysenko V.V., Brodyn M.S., Gayvoronsky V.Ya. // Nanoscale Research Letters. — 2017. — Vol. 12, No. 1. — P. 69 (10pp).

16**. Multian V.V., Dantec R., Mugnier Y., Gayvoronsky V.Ya., Characterization of the nonlinear optical properties of ZnO nanoparticles // NANO-2018 – Kyiv (Ukraine) 2018. – P. 707.

17**. Multian V.V., Budnik P.I., Lisnyak V.V., Gayvoronsky V.Ya., Elastic optical scattering of ZnO nanoparticles and bulk crystals under CW laser excitation at 532 nm // NANO-2018 – Kyiv (Ukraine) 2018. – P. 180.

Appendix

Spectral analysis

Characteristics of the instruments used to measure the spectra are presented in Table 1s.1.

The ultraviolet diffuse reflection (UV-DR) spectra of ZnO single crystals and solid precipitates containing ZnO NPs, as well as ultraviolet (UV) absorption spectra of ZnO NPs colloidal suspensions, were recorded at a scanning speed of 1 nm using a spectrophotometer SF1. Spectrophotometer SF2 was used to measure the transmission spectra. The transmission and reflection of ZnO single crystals were measured using an integral sphere to increase the accuracy of the measurement.

Fourier-transform infrared spectroscopy (FTIR) spectra were obtained on SF3. To study samples in the near-infrared range, a monochromator SF4 was used.

Table 1s.1 Applied instruments for spectral measurements.

ID	Brand	Range	Application
		λ , μm	
SF1	Shimadzu, UV-2700	0.2-0.9	Reflectance, transmittance
SF2	Shimadzu UV-2450	0.2-1.1	Transmittance
SF3	Thermo Nicolet Nexus 470 FTIR	2.0-25.0	Transmittance
SF4	MDR-6 LOMO	0.4-1.3	Transmittance
SF5	LS 55, Perkin-Elmer	0.2-0.8	PL
SF6	Andor Shamrock 193	0.2-2.2	PL, SHG, THG
SF7	Lambda 35 PerkinElmer	0.2-1.1	Transmittance

The photoluminescence measurements of the ZnO NPs dispersed in solvents and ZnO monocrystals were carried out at 25 °C using a spectrofluorimeter SF5 with a xenon lamp (150 W). The wavelength of the excitation varied from 200 to 600 nm with 5 nm steps. The excitation and radiation spectra were recorded in the range of 200-800 nm under optimal conditions at maximum wavelengths for each studied system. Spectral data were obtained using a bandwidth of 3 nm and a 0.5 nm step for monochromators of radiation and excitation. It should be noted that all measurements were made through calibrated diaphragms to minimize the loss of useful information through the effects of scattering.

In the multiphoton microscopy setup, a monochromator SF6 with a CCD matrix iDus 40, cooled by the Peltier element, was used.

The transmittance spectra of KDP crystals with incorporated nanoparticles were studied using the spectrophotometer SF7.

Examples of results obtained by elastic light scattering setup

Elastic light scattering technique was applied to study the influence of non-stoichiometry by oxygen on optical quality in phosphate laser glasses $58\text{P}_2\text{O}_5-13\text{K}_2\text{O}-8\text{Al}_2\text{O}_3-4\text{B}_2\text{O}_3-2.5\text{La}_2\text{O}_3-2\text{SiO}_2-0.5\text{Nd}_2\text{O}_3-12(\text{Ba}_{1-x}\text{O}/\text{Sr}_x\text{O})$ with various level of molar substitution x [171].

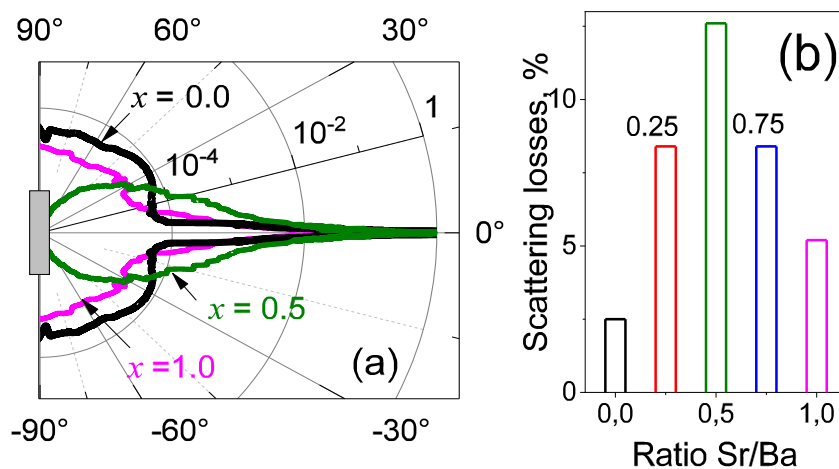


Fig 1s.1 (a) Elastic optical scattering indicatrices for Nd³⁺:Ba_{1-x}Sr_xLPGL under excitation at 1064 nm. (b) Scattering losses in the forward hemisphere for a different Sr/Ba ratio: $x = 0.0, 0.25, 0.50, 0.75, 1.0$.

The analysis revealed non-monotonic changes in the efficiency of elastic optical scattering with increasing Sr/Ba ratio, that correlates with the content of oxygen vacancies in these glasses (see Fig 1s.1b). In cases of $x = 0.25$ and 0.75 scattering losses are about 8.4%. Because of the steric factor, these losses increase 1.5 times for a moderate substitution level $x = 0.5$. The smallest contribution of elastic scattering is observed for glasses with one type of Sr^{2+} ion ($x = 0$) or Ba^{2+} ($x = 1$). In the last case, they are twice as higher in comparison to $x = 0$ due to the smaller radius of cation Sr^{2+} against Ba^{2+} .

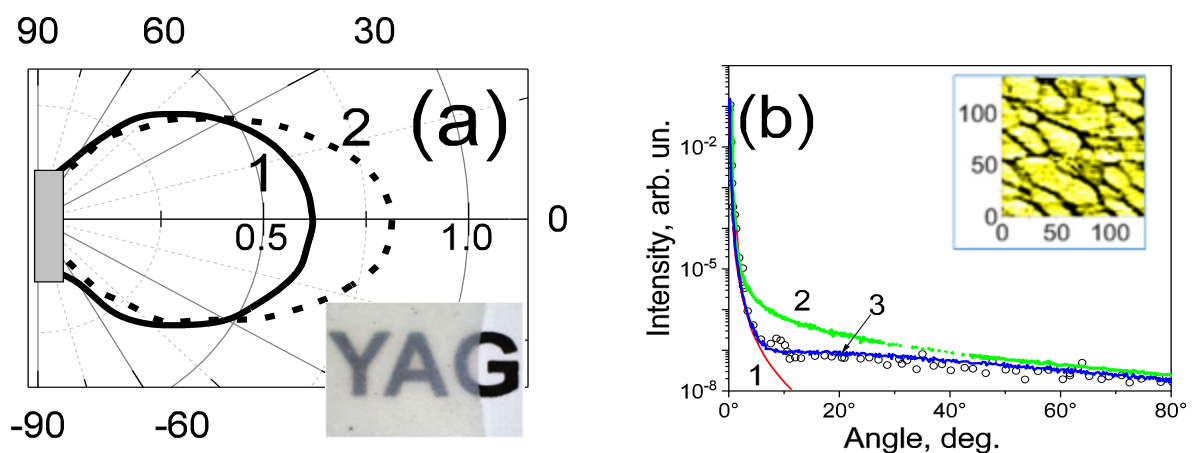


Fig 1s.2 a) Elastic optical scattering indicatrices of YAG laser ceramics with annealing temperatures of 400 °C (1) and 500 °C at 532 nm. The insert contains a photo of a sample of laser ceramics YAG. b) Comparison of different approximations for fitting of nanocrystalline silicon scattering indicatrices: 1) - RGD, 2) - amplitude-phase screen, 3) - T-matrix. The insert contains an AFM image of a nanostructured silicon film with thickness 10 nm.

The phenomena associated with the scattering of light by particles can be fully described by the Mie equation [66]. However, the analysis for this model requires significant computational resources. Alternatively, a several approximations can be used to solve this problem including Rayleigh-Gans-Debye (RGD) approximation [66]. This model was used to analyze the response of YAG laser ceramics [98] that were made at different annealing temperatures. Therefore, they have a different grain size that needs to be estimated. According to the RGD approximation, the distribution of the intensity of scattered light can be described by the equation:

$$I(\theta) = I_0 \frac{32\pi^4}{9\lambda^4 l^2} \left(\frac{\Delta n}{n}\right)^2 (1 + \cos^2 \theta) P_p(u),$$

the distance from the sample to the detector, θ is the scattering angle, n – refractive index of the medium, Δn is the difference between the refractive index of the scatterer and the environment, $P_p(u)$ is the scattering form factor for polydisperse samples, that is defined as:

$$P_p(u) \equiv \sum_V r_j^6 P(u_j), \text{ where } P(u) \equiv \left[\frac{3}{u^3} (\sin u - u \cos u) \right]^2, \quad u \equiv \frac{4\pi r}{\lambda} \sin\left(\frac{\theta}{2}\right).$$

In the framework of the RGD model, it was shown that an increase in the annealing temperature of YAG ceramics from 400 °C to 500 °C (see Fig.1s.2a) leads to an increase in the size of elementary scatterer from 80 to 180 nm with a maximum at 475 °C, which is well in agreement with the data of electron microscopy. This information is important for the production of optical ceramics with high quality [98].

To analyze the angular distribution of scattered radiation for complex nanostructures, it is necessary to use more complex models that require significant computing resources. Thus, in [99], samples of films with nanosized silicon islands with thickness from 3 nm to 85 nm on a silicon substrate were studied. The high sensitivity of the scattering indicatrix to the sizes of nanostructures on the silicon surface was shown. Three approaches were used for simulation: amplitude-phase screen [172,173], RGD approximation, and T-matrix [174] (see Fig 1s.2b). It has been shown that it is possible to determine with high accuracy the size of an elementary scatterer in such structures, if we use estimation of fitting initial parameters from the data of spectral analysis of samples. The proposed approach based on the analysis of optical response data can be used as an alternative or additional technique to the AFM data for rapid diagnosis of the advanced nanostructures [99].

The developed device for scattering indicatrices measurements also showed high efficiency in the study of strongly absorbing and dispersive media. The paper [65] describes the application of a method for analyzing scattering indications for the study of the effect of bromination of carbon fiber sorbents in

order to distinguish the angular distribution of deposits of physically and chemically adsorbed bromine on the surface of fibers. It is known that the physically absorbed bromine, located in nanopores, induces dielectric and structural effects on the polarizability and surface conductivity through the charge effect. An analysis of the experimental data of elastic optical scattering at 532 nm showed a correlation (i) between the scattering efficiency forward and the concentration of chemisorbed bromine; (ii) between the scattering signal in the backward hemisphere and the integral intensity of HBr^+ in the profiles of

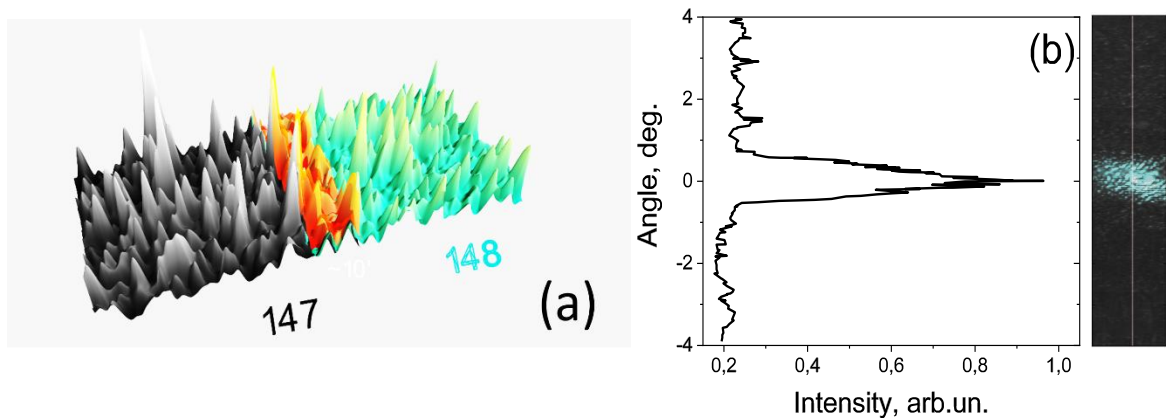


Fig 1s.3 (a) The area of overlapping of two frames. (b) An example of a panorama reproduced with a signal cut through the peak of the beam.

temperature-programmable desorption and mass spectroscopy [65].

Precise measurements of angular distribution of scattered radiation and reconstructing of scattering panoramas the 16-bit CCD matrix ATiK 16 IC-HS (640x480 pixels 7.4x7.4 mkm) was used. To extend the dynamic range of signal registration, a combination of sets of neutral filters and a hardware exposure from 10s to 1 μ s was used.

The process of numerical reconstruction of the scattering indicatrix consists in combining the frames captured with the CCD matrix for the corresponding angular positions of the registration arm and obtaining a cut of the intensity distribution in the horizontal plane. The angular size of the larger side of the image can be written as $\theta_{CCD} = \text{arctg}(a/R) \approx 1.13^\circ$, where $a = 640\text{px} \times 7.4\mu\text{m}$ - the horizontal size of the sensor, $R = 24 \text{ cm}$ - the distance from

the CCD matrix to the center of the device. Measurements were carried out with step 1° to obtain small overlapping of two consecutive frames (Fig 1s.3a). For each frame, the background component is deleted and signal is filtered by two-dimensional Gaussian filter. For the overlap area, also a sliding average filtering is used to ensure that a uniform grid is restored within the frame. After combining frames, one-dimensional slice of 2D panoramas that passes through the center of the peak of intensity is obtained (see Fig 1s.3b).

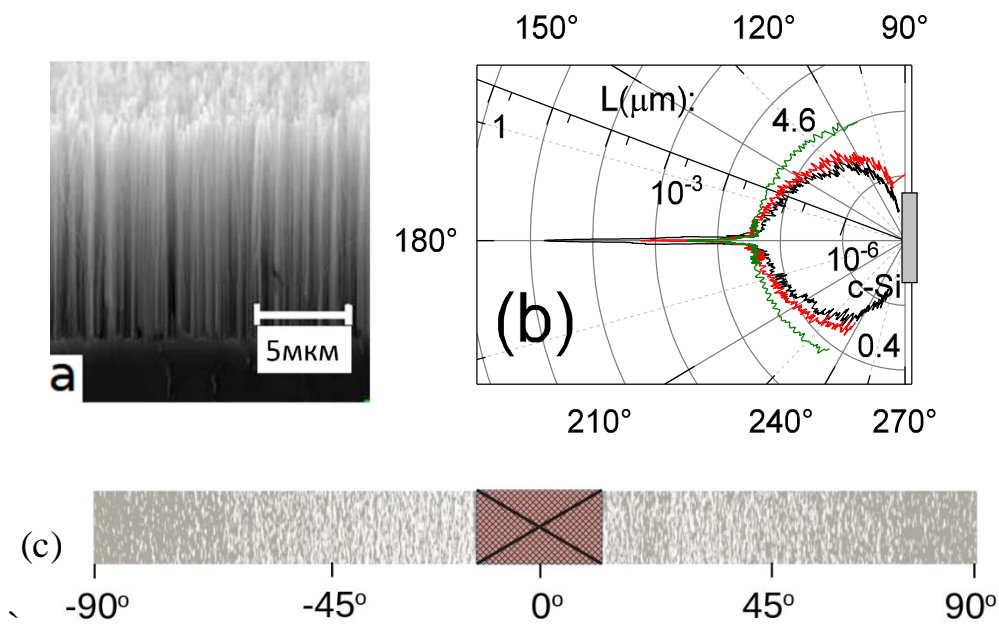


Fig 1s.4 (a) SEM image of silicon nanowires. (b) The cross section of the scattering indicatrix for the silicon c-Si and the silicon nanowires with lengths of 0.4 and 4.6 μm under excitation at 1064 nm. (c) reconstruction of scattering panoramas in the backward hemisphere.

The reconstructed profile is similar to X-ray diffraction profiles and contains a lot of information about sample features. Taking to account the size of the pixel and the distance to the sample, the angular resolution of this registration method is 6 angular seconds per frame. To ensure such high accuracy throughout the scattering panorama, an algorithm for software stabilization of the frame is used. It is based on the next frame position optimization by minimization of the intensity difference of the overlapped regions by the conjugate gradients method [175]. The function for minimization in the overlap area of $N \times M$ has the following form:

$$F_{err}(n, p) = \frac{1}{2^{N \cdot M}} \sum_i \sum_j [S_1(x_i, y_j) - S_2(x_i + n, y_j + p)].$$

This approach makes it possible to improve the frame positioning and increase the resolution of reconstructed profile.

The presented approach allowed to realize a scattering analysis from silicon nanowires length close to the wavelength of excitation. For these samples, the influence of the length of nanowires on the efficiency of the light scattering (see Fig 1s.4) was shown [176].

CCD matrix also allows study the effects of laser beam self-action and analyze changes in the profile of a beam passed through a sample (see Fig. 2.3b). For ZnO single crystals, high optical scattering sensitivity to defects concentration due to high polarizability of defective states and an effective refractive response of photoinduced delocalized carriers was shown [67].

References

1. Biomarkers and surrogate endpoints: Preferred definitions and conceptual framework // *Clin. Pharmacol. Ther.* 2001. Vol. 69, № 3. P. 89–95.
2. Pritula I. et al. Optical, structural and microhardness properties of KDP crystals grown from urea-doped solutions // *Mater. Res. Bull.* 2008. Vol. 43, № 10. P. 2778–2789.
3. Kosinova A.V. et al. KDP single crystal based nonlinear optical material: pat. 49798 UA. 2010.
4. Popov A.S. et al. Nonlinear optical response of nanocomposites based on KDP single crystal with incorporated $\text{Al}_2\text{O}_3 \cdot n\text{H}_2\text{O}$ nanofibriles under CW and pulsed laser irradiation at 532nm // *Opt. Commun.* 2016. Vol. 379. P. 45–53.
5. *Nonlinear Optical Microscopy // Optical Imaging and Microscopy.* Berlin, Heidelberg: Springer Berlin Heidelberg, 2007. Vol. 87. P. 237–268.
6. Streets A.M. et al. Imaging without Fluorescence: Nonlinear Optical Microscopy for Quantitative Cellular Imaging // *Anal. Chem.* 2014. Vol. 86, № 17. P. 8506–8513.
7. Min W. et al. Coherent Nonlinear Optical Imaging: Beyond Fluorescence Microscopy // *Annu. Rev. Phys. Chem.* 2011. Vol. 62, № 1. P. 507–530.
8. Denk W., Strickler J., Webb W. Two-photon laser scanning fluorescence microscopy // *Science.* 1990. Vol. 248, № 4951. P. 73–76.
9. You S. et al. Slide-free virtual histochemistry (Part II): detection of field cancerization // *Biomed. Opt. Express.* 2018. Vol. 9, № 11. P. 5253–5268.
10. Extermann J. et al. Nanodoublers as deep imaging markers for multi-photon microscopy // *Opt. Express.* 2009. Vol. 17, № 17. P. 15342–15349.
11. Staedler D. et al. Harmonic Nanocrystals for Biolabeling: A Survey of Optical Properties and Biocompatibility // *ACS Nano.* 2012. Vol. 6, № 3. P. 2542–2549.
12. Le Xuan L. et al. Photostable Second-Harmonic Generation from a Single KTiOPO_4 Nanocrystal for Nonlinear Microscopy // *Small.* 2008. Vol. 4, № 9. P. 1332–1336.
13. Rogov A., Mugnier Y., Bonacina L. Harmonic nanoparticles: noncentrosymmetric metal oxides for nonlinear optics // *J. Opt.* 2015. Vol. 17, № 3. P. 033001 (12pp).
14. Rodríguez E.M. et al. Non-linear niobate nanocrystals for two-photon imaging // *Opt. Mater.* 2011. Vol. 33, № 3. P. 258–266.
15. Sandeau N. et al. Defocused imaging of second harmonic generation from a single nanocrystal // *Opt. Express.* 2007. Vol. 15, № 24. P. 16051–16060.
16. Albota M.A., Xu C., Webb W.W. Two-photon fluorescence excitation cross sections of biomolecular probes from 690 to 960 nm // *Appl. Opt.* 1998. Vol. 37, № 31. P. 7352–7356.
17. Larson D.R. Water-Soluble Quantum Dots for Multiphoton Fluorescence Imaging in Vivo // *Science.* 2003. Vol. 300, № 5624. P. 1434–1436.
18. Hsieh C.-L. et al. Three-dimensional harmonic holographic microscopy using nanoparticles as probes for cell imaging: erratum // *Opt. Express.* 2010. Vol. 18, № 4. P. 3456–3457.

19. Kachynski A.V. et al. Zinc Oxide Nanocrystals for Nonresonant Nonlinear Optical Microscopy in Biology and Medicine // *J. Phys. Chem. C*. 2008. Vol. 112, № 29. P. 10721–10724.
20. Grange R. et al. Imaging with second-harmonic radiation probes in living tissue // *Biomed. Opt. Express*. 2011. Vol. 2, № 9. P. 2532–2539.
21. König K. et al. Cellular response to near-infrared femtosecond laser pulses in two-photon microscopes // *Opt. Lett.* 1997. Vol. 22, № 2. P. 135–136.
22. Le Dantec R. et al. Ensemble and Individual Characterization of the Nonlinear Optical Properties of ZnO and BaTiO₃ Nanocrystals // *J. Phys. Chem. C*. 2011. Vol. 115, № 31. P. 15140–15146.
23. Joulaud C. et al. Characterization of the nonlinear optical properties of nanocrystals by Hyper Rayleigh Scattering // *J. Nanobiotechnology*. 2013. Vol. 11, № Suppl 1. P. S8.
24. Kim E. et al. Second-Harmonic Generation of Single BaTiO₃ Nanoparticles down to 22 nm Diameter // *ACS Nano*. 2013. Vol. 7, № 6. P. 5343–5349.
25. Liu J. et al. Renal clearable inorganic nanoparticles: a new frontier of bionanotechnology // *Mater. Today*. 2013. Vol. 16, № 12. P. 477–486.
26. Du B., Yu M., Zheng J. Transport and interactions of nanoparticles in the kidneys // *Nat. Rev. Mater.* 2018. Vol. 3, № 10. P. 358–374.
27. Pu Y. et al. Nonlinear Optical Properties of Core-Shell Nanocavities for Enhanced Second-Harmonic Generation // *Phys. Rev. Lett.* 2010. Vol. 104, № 20. P. 207402 (4pp).
28. Zhang Y. et al. Toward Surface Plasmon-Enhanced Optical Parametric Amplification (SPOPA) with Engineered Nanoparticles: A Nanoscale Tunable Infrared Source // *Nano Lett.* 2016. Vol. 16, № 5. P. 3373–3378.
29. Metzger B. et al. Doubling the Efficiency of Third Harmonic Generation by Positioning ITO Nanocrystals into the Hot-Spot of Plasmonic Gap-Antennas // *Nano Lett.* 2014. Vol. 14, № 5. P. 2867–2872.
30. Aouani H. et al. Third-harmonic-upconversion enhancement from a single semiconductor nanoparticle coupled to a plasmonic antenna // *Nat. Nanotechnol.* 2014. Vol. 9, № 4. P. 290–294.
31. Butet J., Brevet P.-F., Martin O.J.F. Optical Second Harmonic Generation in Plasmonic Nanostructures: From Fundamental Principles to Advanced Applications // *ACS Nano*. 2015. Vol. 9, № 11. P. 10545–10562.
32. Celebrano M. et al. Mode matching in multiresonant plasmonic nanoantennas for enhanced second harmonic generation // *Nat. Nanotechnol.* 2015. Vol. 10, № 5. P. 412–417.
33. Light Scattering by a Dielectric Sphere: Perspectives on the Mie Resonances // *Appl. Sci.* 2018. Vol. 8, № 2. P. 184 (22pp).
34. Liu S. et al. III-V Semiconductor Nanoresonators-A New Strategy for Passive, Active, and Nonlinear All-Dielectric Metamaterials // *Adv. Opt. Mater.* 2016. Vol. 4, № 10. P. 1457–1462.
35. Timpu F. et al. Second-Harmonic Enhancement with Mie Resonances in Perovskite Nanoparticles // *ACS Photonics*. 2017. Vol. 4, № 1. P. 76–84.

36. Dubreil L. et al. Multi-harmonic Imaging in the Second Near-Infrared Window of Nanoparticle-Labeled Stem Cells as a Monitoring Tool in Tissue Depth // *ACS Nano*. 2017. Vol. 11, № 7. P. 6672–6681.
37. Zhou J., Liu Z., Li F. Upconversion nanophosphors for small-animal imaging // *Chem Soc Rev*. 2012. Vol. 41, № 3. P. 1323–1349.
38. Regny S. et al. Microwave Synthesis and Up-Conversion Properties of SHG-Active α -(La, Er)(IO₃)₃ Nanocrystals // *Inorg. Chem*. 2019. Vol. 58, № 2. P. 1647–1656.
39. Brasselet S. et al. *In Situ* Diagnostics of the Crystalline Nature of Single Organic Nanocrystals by Nonlinear Microscopy // *Phys. Rev. Lett*. 2004. Vol. 92, № 20. P. 207401 (5pp).
40. Bonacina L. et al. Polar Fe(IO₃)₃ nanocrystals as local probes for nonlinear microscopy // *Appl. Phys. B*. 2007. Vol. 87, № 3. P. 399–403.
41. Yang X., Xie S. Expression of third-order effective nonlinear susceptibility for third-harmonic generation in crystals // *Appl. Opt*. 1995. Vol. 34, № 27. P. 6130–6135.
42. Biaggio I. Nonlocal Contributions to Degenerate Four-Wave Mixing in Noncentrosymmetric Materials // *Phys. Rev. Lett*. 1999. Vol. 82, № 1. P. 193–196.
43. Bosshard C. et al. Non-phase-matched optical third-harmonic generation in noncentrosymmetric media: cascaded second-order contributions for the calibration of third-order nonlinearities // *Phys. Rev. B*. 2000. Vol. 61, № 16. P. 10688–10701.
44. Bredas J.L. et al. Third-Order Nonlinear Optical Response in Organic Materials: Theoretical and Experimental Aspects // *Chem. Rev*. 1994. Vol. 94, № 1. P. 243–278.
45. Tsang T.Y.F. Optical third-harmonic generation at interfaces // *Phys. Rev. A*. 1995. Vol. 52, № 5. P. 4116–4125.
46. Clay G.O. et al. Spectroscopy of third-harmonic generation: evidence for resonances in model compounds and ligated hemoglobin // *J. Opt. Soc. Am. B*. 2006. Vol. 23, № 5. P. 932–950.
47. Zaitseva N., Carman L. Rapid growth of KDP-type crystals // *Prog. Cryst. Growth Charact. Mater*. 2001. Vol. 43, № 1. P. 1–118.
48. Pritula I. et al. Growth and characterization of KDP single crystals doped with TiO₂ nanocrystals // *Funct. Mater*. 2008. Vol. 15, № 3. P. 420–428.
49. Benedict J.B. et al. Up-conversion Luminescence in Dye-Doped Crystals of Potassium Hydrogen Phthalate // *Adv. Mater*. 2003. Vol. 15, № 13. P. 1068–1070.
50. Gayvoronsky V. et al. Giant nonlinear optical response of nanoporous anatase layers // *Appl. Phys. B*. 2005. Vol. 80, № 1. P. 97–100.
51. Gayvoronsky V. et al. Giant nonlinear optical response application for nanoporous titanium dioxide photocatalytic activity monitoring // *Phys. Status Solidi C*. 2005. Vol. 2, № 9. P. 3303–3307.

52. Ogorodnikov I.N. et al. Transient optical absorption of hole polarons in ADP ($\text{NH}_4\text{H}_2\text{PO}_4$) and KDP (KH_2PO_4) crystals // *Phys. Solid State*. 2002. Vol. 44, № 5. P. 880–887.
53. Parikh K.D. et al. Thermal, FT-IR and SHG efficiency studies of L-arginine doped KDP crystals // *Bull. Mater. Sci.* 2007. Vol. 30, № 2. P. 105–112.
54. Grachev V.G. et al. Macroscopic and microscopic defects and nonlinear optical properties of KH_2PO_4 crystals with embedded TiO_2 nanoparticles // *J. Appl. Phys.* 2012. Vol. 112, № 1. P. 014315.
55. Krasnoholovets V.A. A Theoretical Study of the Refractive Index of KDP Crystal Doped with TiO_2 Nanoparticles // *Sustainable Nanosystems Development, Properties, and Applications* / ed. Putz M.V., Mirica M.C. IGI Global, 2017. Vol. 13. P. 524–534.
56. Gayvoronsky V.Y. et al. Impact of incorporated anatase nanoparticles on the second harmonic generation in KDP single crystals // *Laser Phys. Lett.* 2013. Vol. 10, № 3. P. 035401 (5pp).
57. Pritula I. et al. Effect of incorporation of titanium dioxide nanocrystals on bulk properties of KDP crystals // *Opt. Mater.* 2011. Vol. 33, № 4. P. 623–630.
58. Ishioka K., Petek H. Raman generation of coherent phonons of anatase and rutile TiO_2 photoexcited at fundamental absorption edges // *Phys. Rev. B*. 2012. Vol. 86, № 20. P. 205201 (6pp).
59. Golovan L.A. et al. Anomalous enhancement of supercontinuum generation efficiency in KDP crystals incorporated with anatase nanoparticles. Moscow, Russia, 2013. P. IWM6.
60. Khasanov O. et al. Terahertz Generation via Excitation of Surface States Formed from Spatially Separated Electrons and Holes in Nanocomposites. Barcelona, Spain, 2017. P. 233.
61. Fedotova O.M. et al. Harmonic generation via excitation of surface states formed from spatially separated electrons and holes in nanocomposites // *Ultrafast Bandgap Photonics III* / ed. Rafailov M.K. Orlando, United States: SPIE, 2018. P. 49.
62. Rifani M. et al. Solid State Dye Lasers from Stereospecific Host-Guest Interactions // *J. Am. Chem. Soc.* 1995. Vol. 117, № 28. P. 7572–7573.
63. Rudneva E.B. et al. Growth of KDP crystals from solutions with mechanical impurities // *Crystallogr. Rep.* 2006. Vol. 51, № 1. P. 142–149.
64. Chu B. *Laser Light Scattering*. Elsevier, 1974. 333 p.
65. Multian V.V. et al. Surface Response of Brominated Carbon Media on Laser and Thermal Excitation: Optical and Thermal Analysis Study // *Nanoscale Res. Lett.* 2017. Vol. 12, № 1. P. 146 (7pp).
66. Dmitruk N.L., Goncharenko A.V., Venger E.F. *Optics of small particles and composite media*. 2009. 382 p.
67. Uklein A.V. et al. Nonlinear optical response of bulk ZnO crystals with different content of intrinsic defects // *Opt. Mater.* 2018. Vol. 84. P. 738–747.
68. Popov A.S. et al. Nonlinear optical response of the KDP single crystals with incorporated TiO_2 nanoparticles in visible range: effect of the nanoparticles concentration // *Funct. Mater.* 2017. Vol. 24, № 1. P. 5–10.

69. Gayvoronsky V.Y. et al. Interplay of Quadratic and Cubic Nonlinear Optical Responses in KDP Single Crystals with Incorporated TiO₂ Nanoparticles // *Nanomaterials Imaging Techniques, Surface Studies, and Applications*. Springer, 2013. P. 349–365.
70. Rogov A. et al. Simultaneous Multiharmonic Imaging of Nanoparticles in Tissues for Increased Selectivity // *ACS Photonics*. 2015. Vol. 2, № 10. P. 1416–1422.
71. Riporto J. et al. Dielectric Nanoparticles as Efficient RGB Sources by Second, Third, and Fourth Harmonic Generation Excited at Telecom Wavelengths // *ArXiv170708451 Phys*. 2017.
72. Schmidt C. et al. Multi-Order Investigation of the Nonlinear Susceptibility Tensors of Individual Nanoparticles // *Sci. Rep.* 2016. Vol. 6. P. 25415 (9pp).
73. Joulaud C. et al. Characterization of the nonlinear optical properties of nanocrystals by Hyper Rayleigh Scattering // *J. Nanobiotechnology*. 2013. Vol. 11, № Suppl 1. P. S8.
74. Le Dantec R. et al. Ensemble and individual characterization of the nonlinear optical properties of ZnO and BaTiO₃ nanocrystals // *J. Phys. Chem. C*. 2011. Vol. 115, № 31. P. 15140–15146.
75. Schmidt C. et al. Multi-Order Investigation of the Nonlinear Susceptibility Tensors of Individual Nanoparticles // *Sci. Rep.* Nature Publishing Group, 2016. Vol. 6. P. 25415.
76. Bosshard C. et al. Non-phase-matched optical third-harmonic generation in noncentrosymmetric media: Cascaded second-order contributions for the calibration of third-order nonlinearities // *Phys. Rev. B*. 2000. Vol. 61, № 16. P. 10688–10701.
77. Multian V.V. et al. Averaged third-order susceptibility of ZnO nanocrystals from Third Harmonic Generation and Third Harmonic Scattering // *Opt. Mater.* 2018. Vol. 84. P. 579–585.
78. Steerteghem N. Van et al. Third-Harmonic Scattering for Fast and Sensitive Screening of the Second Hyperpolarizability in Solution // *Anal. Chem.* 2017. Vol. 89. P. 2964–2971.
79. Clay G.O. et al. Spectroscopy of third-harmonic generation: evidence for resonances in model compounds and ligated hemoglobin // *J. Opt. Soc. Am. B*. 2006. Vol. 23, № 5. P. 932.
80. Gouy L.G. Sur une propriété nouvelle des ondes lumineuses // *Optics*. Gauthier-Villars, 1890. Vol. 110. P. 1251.
81. Boyd R.W. Intuitive explanation of the phase anomaly of focused light beams // *J. Opt. Soc. Am.* 1980. Vol. 70, № 7. P. 877–880.
82. Barad Y. et al. Nonlinear scanning laser microscopy by third harmonic generation // *Appl. Phys. Lett.* 1997. Vol. 70, № 8. P. 922–924.
83. Débarre D., Beaurepaire E. Quantitative Characterization of Biological Liquids for Third-Harmonic Generation Microscopy // *Biophys. J.* 2007. Vol. 92, № 2. P. 603–612.

84. Gubler U., Bosshard C. Optical third-harmonic generation of fused silica in gas atmosphere: Absolute value of the third-order nonlinear optical susceptibility $\chi^{(3)}$ // *Phys. Rev. B*. 2000. Vol. 61, № 16. P. 10702–10710.
85. Hui P.M., Cheung P., Stroud D. Theory of third harmonic generation in random composites of nonlinear dielectrics // *J. Appl. Phys.* 1998. Vol. 84, № 7. P. 3451–3458.
86. Zhao W., Palffy-Muhoray P. Z-scan measurement of $\chi(3)$ using top-hat beams // *Appl. Phys. Lett.* 1994. Vol. 65, № 6. P. 673–675.
87. Uklein A.V. et al. Photoinduced refractive index variation within picosecond laser pulses excitation as the indicator of oxyorthosilicates single crystals composition modification // *Nanoscale Res. Lett.* 2015. Vol. 10, № 1. P. 102 (7pp).
88. Yakunin S.V. et al. Experimental Technique for the $\chi^{(3)}$ Measurement of Organic Dye in Nematic Liquid Crystal System. Sevastopol (Crimea, Ukraine)., 2003. P. 284.
89. Pergamenschchik V.M. et al. Hypothesis of Dye Aggregation in a Nematic Liquid Crystal: From Experiment to a Model of the Enhanced Light-Director Interaction // *Mol. Cryst. Liq. Cryst.* 2006. Vol. 454, № 1. P. 145/[547]-156/[558].
90. Gayvoronsky V. et al. Techniques to Characterize the Nonlinear Optical Response of Doped Nematic Liquid Crystals // *Mol. Cryst. Liq. Cryst.* 2005. Vol. 426, № 1. P. 231–241.
91. Gayvoronsky V.Y. et al. Nonlinear optical response of liquid crystal doped with anthraquinone dyes. 2006. P. 86–87.
92. Sheik-Bahae M. et al. Sensitive measurement of optical nonlinearities using a single beam // *IEEE J. Quantum Electron.* 1990. Vol. 26, № 4. P. 760–769.
93. Borshch A.A., Brodyn M.S., Gayvoronsky V.Y. Diagnostics of optical nonlinearities: spatial beam distortion technique and its application to semiconductors and novel materials / ed. Svechnikov S.V., Valakh M.Y. 2003. P. 128–136.
94. Gayvoronsky V. et al. Competitive Optical Nonlinearities and Photoinduced Transformation of Epoxy Polymer Based on Diglycidyl Ether of Bisphenol A // *Mol. Cryst. Liq. Cryst. Sci. Technol. Sect. Mol. Cryst. Liq. Cryst.* 2001. Vol. 361, № 1. P. 257–262.
95. Multian V. et al. Characterization of the nonlinear optical properties of ZnO nanoparticles // *NANO-2018*. Kyiv, Ukraine, 2018. P. 707.
96. Young M.D. et al. A pragmatic guide to multiphoton microscope design // *Adv. Opt. Photonics*. 2015. Vol. 7, № 2. P. 276.
97. Melnichenko M.S. et al. Optical and Nonlinear Optical Characterization of Novel Materials Based on Silicon Nanowires. Kyiv, Ukraine, 2013. P. 98.
98. Gayvoronsky V.Y. et al. The Effect of Sintering Temperature on Linear and Nonlinear Optical Properties of YAG Nanoceramics // *Nanocomposites, Nanophotonics, Nanobiotechnology, and Applications* / ed. Fesenko O., Yatsenko L. Springer International Publishing, 2015. P. 147–164.

99. Buchenko V.V. et al. Optical properties of thin nanosilicon films // *Opt. Mater.* 2016. Vol. 62. P. 612–620.
100. Riporto J. et al. Bismuth ferrite dielectric nanoparticles excited at telecom wavelengths as multicolor sources by second, third, and fourth harmonic generation // *Nanoscale*. 2018. Vol. 10, № 17. P. 8146–8152.
101. Barui A.K., Kotcherlakota R., Patra C.R. Chapter 6 - Biomedical applications of zinc oxide nanoparticles // *Inorganic Frameworks as Smart Nanomedicines* / ed. Grumezescu A.M. William Andrew Publishing, 2018. P. 239–278.
102. Du J. et al. ZnO nanoparticles: recent advances in ecotoxicity and risk assessment // *Drug Chem. Toxicol.* 2018. P. 1–12.
103. Chetia T.R., Ansari M.S., Qureshi M. Rational design of hierarchical ZnO superstructures for efficient charge transfer: mechanistic and photovoltaic studies of hollow, mesoporous, cage-like nanostructures with compacted 1D building blocks // *Phys. Chem. Chem. Phys.* 2016. Vol. 18, № 7. P. 5344–5357.
104. Sun X. et al. Morphology-tunable synthesis of ZnO nanoforest and its photoelectrochemical performance // *Nanoscale*. 2014. Vol. 6, № 15. P. 8769–8780.
105. Li X. et al. Microwave hydrothermal synthesis and gas sensing application of porous ZnO core–shell microstructures // *RSC Adv.* 2014. Vol. 4, № 61. P. 32538.
106. Jeen Maria M. et al. Zn-dust derived ultrafine grained ZnO non-linear ceramic resistors via in-situ thermal oxidation of cermet reactant mixture // *Mater. Des.* 2016. Vol. 92. P. 387–396.
107. Shi W., Song S., Zhang H. Hydrothermal synthetic strategies of inorganic semiconducting nanostructures // *Chem. Soc. Rev.* 2013. Vol. 42, № 13. P. 5714–5743.
108. Multian V., Le Dantec R., Gayvoronsky V. Characterization of colloidal nanoparticle suspensions using the third harmonic generation at interfaces // *Ukr. J. Phys. Opt.* 2018. Vol. 19, № 2. P. 92–98.
109. Yakunin S. et al. Nanosecond Laser Pulse-Induced Refractive Index Changes in Anthraquinone-Doped Liquid Crystal // *Mol. Cryst. Liq. Cryst.* 2008. Vol. 496, № 1. P. 310–321.
110. Kajzar F., Messier J. Third-harmonic generation in liquids // *Phys. Rev. A.* 1985. Vol. 32, № 4. P. 2352–2363.
111. Pillai R.S., Brakenhoff G.J., Müller M. Analysis of the influence of spherical aberration from focusing through a dielectric slab in quantitative nonlinear optical susceptibility measurements using third-harmonic generation // *Opt. Express*. 2006. Vol. 14, № 1. P. 260.
112. Zappettini A. et al. Wavelength dependence of the third order non-linear coefficient in hydrothermally grown ZnO crystals // *Phys. Status Solidi C*. 2004. Vol. 1, № 4. P. 997–1000.
113. Bentley J.L. Multidimensional binary search trees used for associative searching // *Commun. ACM*. 1975. Vol. 18, № 9. P. 509–517.
114. Orthogonal Range Searching // *Computational Geometry*. Berlin, Heidelberg: Springer Berlin Heidelberg, 2008. P. 95–120.

115. Dhara S., Lynch S.A. Second Harmonic Generation in ZnO Nanowires // Nanowires - New Insights / ed. Maaz K. InTech, 2017. P. 21.
116. Prasanth R. et al. Resonance enhancement of optical second harmonic generation in a ZnO nanowire // Appl. Phys. Lett. 2006. Vol. 88, № 18. P. 181501 (5pp).
117. Riporto J. et al. Second harmonic spectroscopy of ZnO, BiFeO₃ and LiNbO₃ nanocrystals // Opt. Mater. Express. 2019. Vol. 9, № 4. P. 1955–1966.
118. Multian V.V. et al. Synthesis, Characterization, Luminescent and Nonlinear Optical Responses of Nanosized ZnO // Nanoscale Res. Lett. 2017. Vol. 12, № 1. P. 164 (8pp).
119. Tonto P. et al. Preparation of ZnO nanorod by solvothermal reaction of zinc acetate in various alcohols // Ceram. Int. 2008. Vol. 34, № 1. P. 57–62.
120. Hu Z., Oskam G., Searson P.C. Influence of solvent on the growth of ZnO nanoparticles // J. Colloid Interface Sci. 2003. Vol. 263, № 2. P. 454–460.
121. Pourrahimi A.M. et al. Water-based synthesis and cleaning methods for high purity ZnO nanoparticles – comparing acetate, chloride, sulphate and nitrate zinc salt precursors // RSC Adv. 2014. Vol. 4, № 67. P. 35568–35577.
122. Kaurova I.A., Kuz'micheva G.M., Rybakov V.B. Growth and structural, optical, and electrical properties of zincite crystals // Crystallogr. Rep. 2013. Vol. 58, № 2. P. 226–233.
123. Kaurova I.A. et al. Structural peculiarities and point defects of bulk-ZnO single crystals // J. Alloys Compd. 2014. Vol. 616. P. 71–75.
124. Zeng Y.-J. et al. Electronic Band Structures and Native Point Defects of Ultrafine ZnO Nanocrystals // ACS Appl. Mater. Interfaces. 2015. Vol. 7, № 19. P. 10617–10622.
125. Luitel H. et al. Defect generation and recovery in polycrystalline ZnO during annealing below 300 °C as studied by in situ positron annihilation spectroscopy // J. Mater. Sci. 2017. Vol. 52, № 12. P. 7615–7623.
126. Chan K.S. et al. Equilibrium shape of nano-cavities in H implanted ZnO // Appl. Phys. Lett. 2015. Vol. 106, № 21. P. 212102 (5pp).
127. Datta D.P. et al. Temporal evolution of nanoporous layer in off-normally ion irradiated GaSb // J. Appl. Phys. 2014. Vol. 115, № 12. P. 123515.
128. Dutta S. et al. Role of defects in tailoring structural, electrical and optical properties of ZnO // Prog. Mater. Sci. 2009. Vol. 54, № 1. P. 89–136.
129. Bang J. et al. Understanding the presence of vacancy clusters in ZnO from a kinetic perspective // Appl. Phys. Lett. 2014. Vol. 104, № 25. P. 252101 (5pp).
130. Sarkar A. et al. Theoretical and experimental investigation of possible ferromagnetic ordering in wide band gap ZnO and related systems // Nucl. Instrum. Methods Phys. Res. Sect. B Beam Interact. Mater. At. 2016. Vol. 379. P. 18–22.
131. Oga T. et al. Origins of low resistivity in Al ion-implanted ZnO bulk single crystals // J. Appl. Phys. 2011. Vol. 109, № 12. P. 123702.
132. Lines M.E. Influence of *d* orbitals on the nonlinear optical response of transparent transition-metal oxides // Phys. Rev. B. 1991. Vol. 43, № 14. P. 11978–11990.

133. Goh E.G., Xu X., McCormick P.G. Effect of particle size on the UV absorbance of zinc oxide nanoparticles // *Scr. Mater.* 2014. Vol. 78–79. P. 49–52.
134. Talam S., Karumuri S.R., Gunnam N. Synthesis, Characterization, and Spectroscopic Properties of ZnO Nanoparticles // *ISRN Nanotechnol.* 2012. Vol. 2012. P. 1–6.
135. Tauc J. Optical properties and electronic structure of amorphous Ge and Si // *Mater. Res. Bull.* 1968. Vol. 3, № 1. P. 37–46.
136. Jortner J. Cluster size effects // *Z. Phys At. Mol. Clust.* 1992. Vol. 24, № 3. P. 247–275.
137. Viswanatha R. et al. Understanding the quantum size effects in ZnO nanocrystals // *J. Mater. Chem.* 2004. Vol. 14, № 4. P. 661.
138. Uklein A.V. et al. Characterization of oxidized carbon materials with photoinduced absorption response // *Appl. Phys. B.* 2016. Vol. 122, № 12. P. 287–295.
139. Duchateau G. et al. Electron-hole dynamics in normal and deuterated KH_2PO_4 illuminated by intense femtosecond laser pulses // *Phys. Rev. B.* 2011. Vol. 83, № 7. P. 075114 (10pp).
140. Thu C. et al. Role of the Metal-Oxide Work Function on Photocurrent Generation in Hybrid Solar Cells // *Sci. Rep.* 2018. Vol. 8, № 1. P. 3559 (8pp).
141. Sokol A.A. et al. Point defects in ZnO // *Faraday Discuss.* 2007. Vol. 134. P. 267–282.
142. Garba L.G. DFT Calculation of Vibrational Frequencies in Nanostructure Zinc Oxide (ZnO) and the Raman Spectra // *International Journal of Engineering Science Invention.* Vol. 5, № 5. P. 66–70.
143. Rodnyi P.A., Khodyuk I.V. Optical and luminescence properties of zinc oxide (Review) // *Opt. Spectrosc.* 2011. Vol. 111, № 5. P. 776–785.
144. Djurišić A.B. et al. ZnO nanostructures: growth, properties and applications // *J. Mater. Chem.* 2012. Vol. 22, № 14. P. 6526–6535.
145. Peng Y. et al. Stable yellow ZnO mesocrystals with efficient visible-light photocatalytic activity // *CrystEngComm.* 2014. Vol. 16, № 34. P. 7906–7913.
146. Børseth T.M. et al. Identification of oxygen and zinc vacancy optical signals in ZnO // *Appl. Phys. Lett.* 2006. Vol. 89, № 26. P. 262112 (3pp).
147. Kukreja L.M. et al. Correlation of spectral features of photoluminescence with residual native defects of ZnO thin films annealed at different temperatures // *J. Appl. Phys.* 2012. Vol. 112, № 1. P. 013525 (10pp).
148. Alvi N.H. et al. The origin of the red emission in n-ZnO nanotubes/p-GaN white light emitting diodes // *Nanoscale Res. Lett.* 2011. Vol. 6, № 1. P. 130.
149. Dong Y. et al. Vacancy defect and defect cluster energetics in ion-implanted ZnO // *Phys. Rev. B.* 2010. Vol. 81, № 8. P. 081201 (4pp).
150. Pal S. et al. Clustered vacancies in ZnO: chemical aspects and consequences on physical properties // *J. Phys. Appl. Phys.* 2018. Vol. 51, № 10. P. 105107.
151. Li H. et al. Zinc Oxide as a Model Transparent Conducting Oxide: A Theoretical and Experimental Study of the Impact of Hydroxylation, Vacancies,

- Interstitials, and Extrinsic Doping on the Electronic Properties of the Polar ZnO (0002) Surface // *Chem. Mater.* 2012. Vol. 24, № 15. P. 3044–3055.
152. McCluskey M.D., Jokela S.J. Defects in ZnO // *J. Appl. Phys.* 2009. Vol. 106, № 7. P. 071101.
153. Oba F. et al. Point defects in ZnO: an approach from first principles // *Sci. Technol. Adv. Mater.* 2011. Vol. 12, № 3. P. 034302 (7pp).
154. Janotti A., Van de Walle C.G. Oxygen vacancies in ZnO // *Appl. Phys. Lett.* 2005. Vol. 87, № 12. P. 122102 (4pp).
155. Ahmed G. et al. Lattice defects of ZnO and hybrids with GO: Characterization, EPR and optoelectronic properties // *AIP Adv.* 2018. Vol. 8, № 2. P. 025218 (11pp).
156. Khan Z.R. et al. Optical and Structural Properties of ZnO Thin Films Fabricated by Sol-Gel Method // *Mater. Sci. Appl.* 2011. Vol. 02, № 05. P. 340–345.
157. Zhang X.Q. et al. Resonant exciton second-harmonic generation in self-assembled ZnO microcrystallite thin films // *J. Phys. Condens. Matter.* 2003. Vol. 15, № 30. P. 5191–5196.
158. Pommiès M. et al. Impurities detection by optical techniques in KH_2PO_4 crystals // *Opt. Commun.* 2007. Vol. 275, № 2. P. 372–378.
159. Grachev V.G. et al. Paramagnetic defects in KH_2PO_4 crystals with high concentration of embedded TiO_2 nanoparticles // *J. Appl. Phys.* 2016. Vol. 119, № 3. P. 034301 (6pp).
160. Gayvoronsky V. et al. Self-focusing effect on the second harmonic generation in the KDP single crystals with incorporated anatase nanoparticles // *Funct. Mater.* 2012. Vol. 19, № 1. P. 54–59.
161. Pritula I.M. et al. Peculiarities of the growth of KDP single crystals with incorporated aluminium oxyhydroxide nanoparticles // *J. Cryst. Growth.* 2012. Vol. 355, № 1. P. 26–32.
162. Pritula I.M. et al. Some characteristic features of formation of composite material based on KDP single crystal with incorporated $\text{Al}_2\text{O}_3 \cdot n\text{H}_2\text{O}$ nanoparticles: Some characteristic features of formation of composite material... // *Cryst. Res. Technol.* 2014. Vol. 49, № 5. P. 345–352.
163. Fujioka K. et al. Optical properties of rapidly grown KDP crystal improved by thermal conditioning // *J. Cryst. Growth.* 1997. Vol. 181, № 3. P. 265–271.
164. Gayvoronsky V.Y. et al. Optical quality characterization of KDP crystals with incorporated TiO_2 nanoparticles and laser scattering experiment simulation // *ArXiv10121741 Cond-Mat Physicsphysics.* 2010.
165. Kostenyukova E.I. et al. Effect of L-arginine additive on the growth and physical properties of Potassium Dihydrogen Phosphate single crystals // *Funct. Mater.* 2018. Vol. 25, № 2. P. 246–257.
166. Golovan L.A. et al. Broadband second-harmonic and sum-frequency generation in KH_2PO_4 crystals doped with anatase nanocrystals // *Laser Phys. Lett.* 2014. Vol. 11, № 7. P. 075901 (5pp).

167. Gayvoronsky V.Y. et al. Photoinduced refractive index variation in the KDP single crystals with incorporated TiO₂ nanoparticles under CW laser excitation // Ukr J Phys. 2012. Vol. 57, № 2. P. 159–165.
168. Karlash A.Y. et al. Effect of thermal treatment and ageing on IR transmission and visible photoluminescence of nanostructured aluminum oxyhydroxide // J. Phys. Appl. Phys. 2012. Vol. 45, № 36. P. 365108 (7pp).
169. Kumaresan P., Moorthy Babu S., Anbarasan P.M. Thermal, dielectric studies on pure and amino acid (l-glutamic acid, l-histidine, l-valine) doped KDP single crystals // Opt. Mater. 2008. Vol. 30, № 9. P. 1361–1368.
170. Pritula I.M. et al. KDP crystal doped with L-arginine amino acid: growth, structure perfection, optical and strength characteristics // Opt. Mater. 2016. Vol. 57. P. 217–224.
171. Uklein A.V. et al. Probing of the oxygen-related defects response in Nd:phosphate glass within self-action of the laser radiation technique // J. Non-Cryst. Solids. 2018. Vol. 498. P. 244–251.
172. Barchuk O.I. et al. Experimental investigations of light depolarization under multiple scattering / ed. Angelsky O.V. 2006. P. 62540W (9pp).
173. Barchuk O.I., Goloborodko A.A., Kurashov V.N. Propagation of Coherent Light Through Optically Inhomogeneous Media // 2006 International Conference on Mathematical Methods in Electromagnetic Theory. Kharkov, Ukraine: IEEE, 2006. P. 375–377.
174. Peterson B., Ström S. T -matrix formulation of electromagnetic scattering from multilayered scatterers // Phys. Rev. D. 1974. Vol. 10, № 8. P. 2670–2684.
175. Nocedal J., Wright S.J. Numerical optimization. Corr. 2. print. New York, NY: Springer, 2000. 636 p.
176. Efimova A.I. et al. New evidence of non-Rayleigh type of light scattering in silicon nanowire arrays formed by metal-assisted chemical etching. Alicante-Benidorm, Spain, 2014. P. 40–41.
177. Zou W. et al. Broadband dye-sensitized upconversion of near-infrared light // Nat. Photonics. 2012. Vol. 6, № 8. P. 560–564.
178. Pantazis P. et al. Second harmonic generating (SHG) nanoprobe for in vivo imaging // Proc. Natl. Acad. Sci. National Acad Sciences, 2010. Vol. 107, № 33. P. 14535–14540.
179. Staedler D. et al. Harmonic Nanocrystals for Bio-Labeling: a Survey of Optical Properties and Biocompatibility Harmonic Nanocrystals for Bio-Labeling: a Survey of Optical Properties and Biocompatibility . // ACS Nano. 2012. Vol. 6, № 3. P. 2542–2549.
180. Geissbuehler M. et al. Nonlinear correlation spectroscopy (NLCS) // Nano Lett. 2012. Vol. 12, № 3. P. 1668–1672.

Résumé en français

Les nanoparticules harmoniques (HNP) sont un nouveau type de marqueurs optiques non linéaires (ONL) pour l'imagerie biomédicale basés sur des nanocristaux inorganiques de structure non centrosymétrique, qui convertissent efficacement le rayonnement laser [10–12]. Ce terme a été introduit pour désigner une nouvelle classe de nanoparticules (NP) qui peuvent générer simultanément la deuxième (SHG), la troisième (THG) et des harmoniques supérieures avec une grande efficacité.

Les marqueurs HNPs sont prometteurs pour des applications dans le domaine de la bio-imagerie en raison de l'interaction optique non résonante, qui offre la possibilité de fixer la longueur d'onde d'excitation dans les fenêtres de transparence biologique. Cela permet de réaliser des images avec une profondeur élevée [10]. De plus, ces marqueurs présentent une excellente photostabilité pour une observation à long terme. Enfin, ces particules peuvent être facilement identifiées dans des environnements complexes grâce à leurs signaux harmoniques très spécifiques et distincts de la réponse des composants des tissus biologiques [11,12].

En général, la génération d'harmoniques dans les cristaux massifs est réalisée dans les conditions d'accord de phase. En raison de la dispersion de l'indice de réfraction, ces conditions ne peuvent être obtenues que dans une gamme limitée de longueurs d'onde d'excitation, pour des orientations spécifiques du cristal et de la polarisation du faisceau pompe. Cependant, si la taille des cristaux ne dépasse pas la longueur de cohérence (généralement inférieure à un micron), ces restrictions disparaissent [15] et il est possible d'observer la génération de signaux harmoniques à toutes les longueurs d'onde d'excitation. Les nanocristaux utilisés pour ces applications sont par exemple, KNbO_3 , BiFeO_3 (BFO), LiNbO_3 , BaTiO_3 , $\text{Fe}(\text{IO}_3)_3$, $\text{Ba}(\text{BO}_2)_2$ (BBO), KTiOPO_4 (KTP) et ZnO [13]. Par rapport aux fluorophores typiques, les HNPs ont une réponse spectrale beaucoup plus étroite et les signaux harmoniques sont assez importants pour être détectés dans la plupart des systèmes standards de microscopie optique non linéaire.

Au cours des dernières années, il y a eu une croissance significative du nombre d'applications pratiques basées sur les HNPs, y compris le photovoltaïque [177], les systèmes de télécommunication, la bio-imagerie [2,3] et la détection [4]. Cela stimule les études sur la synthèse de nouveaux nanocristaux offrant une grande efficacité pour la génération d'harmoniques, avec un contrôle effectif de leur taille et de leur forme. Les HNPs ont de nombreuses caractéristiques intéressantes mais la mise en œuvre dans les applications de bio-imagerie nécessite parfois une diminution de la taille pour une meilleure compatibilité avec les tissus biologiques [25,26]. Cependant, l'intensité des signaux émis est proportionnelle au carré du volume du nanocristal [22–24]. Lorsque la taille des particules diminue, il y a donc une réduction significative des signaux (par exemple, une diminution du diamètre des particules d'un facteur 2 diminue le signal SHG d'un facteur 64).

Plus généralement, il y a un fort intérêt à améliorer l'efficacité des processus optiques non linéaires à l'échelle nanométrique. Une approche est d'exploiter la réponse des plasmons de surface sur des structures métalliques ou hybrides. Une autre approche, plus récente, est basée sur l'utilisation de résonances de Mie sur des nanostructures diélectriques - résonances des courants de déplacement. Conformément à la théorie de Mie, la résonance [33] est située à $\lambda \sim nd$, où d est la taille caractéristique de la NP et n son indice de réfraction. L'amplification du champ dans ces structures diélectriques est généralement plus faible que dans les structures métalliques, mais les facteurs de qualité élevés permettent d'obtenir des réponses efficaces. Ceci a permis d'observer un gain significatif en efficacité SHG et THG dans les matériaux diélectriques et semi-conducteurs [34,35].

Dans ce contexte, il est important de développer des outils adaptés pour caractériser les propriétés optiques non linéaires (ONL) de ces nanostructures. Dans le cadre des applications de bio-imagerie, les premiers travaux ont porté sur la génération de la deuxième harmonique des HNPs. Cependant, exploiter la réponse de la troisième harmonique ou des harmoniques supérieures est également très intéressant. En effet, la détection simultanée de ces signaux peut améliorer significativement l'identification des HNPs dans une image par rapport au signal de fond des tissus biologiques. Il est donc important de pouvoir caractériser les propriétés de THG de ces HNPs.

En complément des nanoparticules harmoniques, nous présentons dans cette thèse nos études portant sur des cristaux massifs de dihydrogénophosphate de potassium (KDP), dopés par des nanoparticules d'oxydes métalliques. Les cristaux de KDP sont bien connus et largement utilisés en optique non linéaire. Ses principaux avantages sont sa technologie de croissance en solution, relativement simple et peu coûteuse, qui permet de réaliser des cristaux de grandes dimensions et son seuil élevé de dommage optique. Par ailleurs, les propriétés des cristaux de KDP purs sont très bien caractérisées. Il devient alors intéressant d'un point de vue théorique et pratique de réaliser des matériaux composites basés sur ces cristaux. Dans ce travail, un ensemble de cristaux composites, basés sur la matrice KDP a été étudié : KDP:TiO₂ et KDP:NOA (NOA : nanofibres d'oxyhydroxyde d'aluminium) et KDP:L-arg dopés avec des molécules de L-arginine. L'objectif de ces dopages est d'améliorer les processus optiques non linéaires au sein de la matrice de KDP.

Ce travail a été réalisé dans le cadre d'une cotutelle entre la France et l'Ukraine. Une partie de la recherche a été effectuée dans le laboratoire SYMME à Annecy et l'autre dans le laboratoire AMNOD à Kiev. Cette thèse présente les résultats obtenus dans ces deux laboratoires et le manuscrit se compose de 5 chapitres.

- Le chapitre 1 présente une revue de la littérature sur les HNPs et les cristaux composites à base de KDP.

- Le chapitre 2 décrit les techniques expérimentales conçues et optimisées pour l'analyse des propriétés optiques des matériaux étudiés. En particulier, j'ai développé des outils pour la mesure des indicatrices de diffusion, la technique I-scan pour la mesure de l'indice de réfraction non linéaire, la mesure de l'efficacité de génération de troisième harmonique, et le développement d'un microscope multiphotonique sous excitation laser femtoseconde dans le domaine spectral 710 - 1300 nm.

- Le chapitre 3 présente les principaux résultats obtenus avec des HNPs commerciales de ZnO (40-150nm) et se compose de deux parties : (i) analyse de l'efficacité THG à partir de mesures d'ensemble, basé sur la technique de la THG aux interfaces et (ii) étude de la réponse spectrale de nanoparticules individuelles avec le microscope.

- Le chapitre 4 présente les caractérisations des propriétés ONL de différentes nanoparticules et structures basées sur le ZnO : (i) très petites nanoparticules (<10 nm) ; (ii) nanostructures de type « framboise » constituées de petites NPs (<10 nm) enrobant de plus grandes NPs (<150 nm) ; (iii) cristaux massifs avec différentes concentrations de défauts.

- Le chapitre 5 présente les résultats sur les monocristaux de KDP dopés par des NPs de TiO₂, des nanoparticules/nanofibres de NOA et par des molécules de L-arginine. La réponse quadratique et cubique est analysée dans chacun des cas.

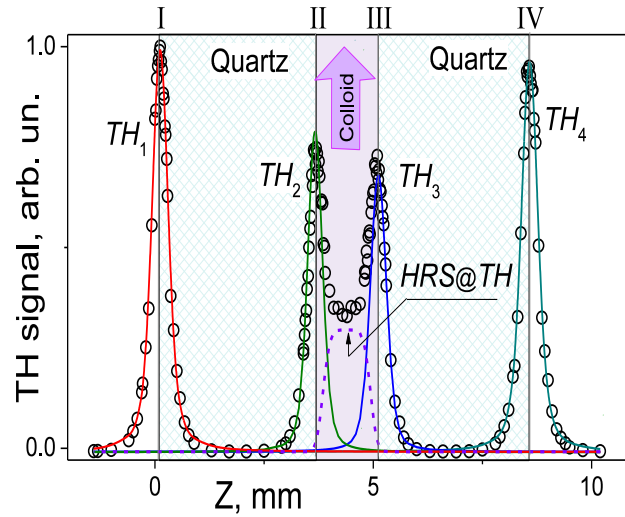


Figure 1 : Signal THG obtenu par balayage à travers une cuvette de silice contenant une suspension de nanoparticules de ZnO de taille ~ 150 nm dans l'éthanol (concentration 1.4×10^{-2} mg/mL). On observe quatre pics aux interfaces I, II, III, IV et un signal de diffusion de troisième harmonique au centre de la cuvette (HRS@TH) [77].

Dans ce résumé, je vais d'abord présenter les principaux résultats concernant la caractérisation de la susceptibilité non linéaire d'ordre 3 de nanocristaux de ZnO (chapitre 3). Nous avons développé une technique originale (THG aux interfaces) qui permet une mesure d'ensemble sur une suspension colloïdale. Initialement, cette méthode avait été développée pour déterminer la susceptibilité de liquides et de gaz [46]. Nous l'avons modifié pour mesurer la susceptibilité moyenne de NPs de ZnO et comparé les valeurs obtenues avec des mesures de diffusion de troisième harmonique.

La technique de THG aux interfaces [46] permet d'estimer la susceptibilité non linéaire cubique d'un échantillon liquide $\chi^{(3)}(3\omega)$ par comparaison avec la valeur connue $\chi_{gl}^{(3)}(3\omega)$ de la cuvette contenant le liquide, généralement en silice [43]. En pratique, le signal de THG aux interfaces échantillon-verre et verre-air est mesuré en déplaçant le point focal du laser (laser YAG 1064 nm) grâce à une platine de translation motorisée sur laquelle est placé la lentille de focalisation (Figure 1).

La susceptibilité du liquide est proportionnelle à la racine carrée du rapport des signaux TH aux interfaces Is échantillon/verre et Ia verre/air :

$$\chi^{(3)}(3\omega) \sim \chi_{gl}^{(3)}(3\omega) (1 \pm (I_s/I_a)^{1/2}) \quad (1)$$

Dans le cas d'une suspension colloïdale, avec une fraction volumique f de NPs très faible, la susceptibilité effective $\chi_{col}^{(3)}$ de la suspension colloïdale peut être écrite comme [85] :

$$\chi_{col}^{(3)}(3\omega) = f \left(\frac{3\epsilon_b(3\omega)}{\epsilon_a(3\omega) + 2\epsilon_b(3\omega)} \right) \left(\frac{3\epsilon_b(\omega)}{\epsilon_a(\omega) + 2\epsilon_b(\omega)} \right)^3 \langle \chi_{NPS}^{(3)}(3\omega) \rangle + \chi_s^{(3)}(3\omega) \quad (2)$$

avec ϵ_a et ϵ_b les permittivités des nanoparticules et du solvant.

En utilisant cette approche, nous avons mesuré les susceptibilités des suspensions $\chi_{col}^{(3)}$ pour différentes concentrations de NPs de ZnO et ensuite estimé la susceptibilité moyenne des particules $\langle |\chi_{NPS}^{(3)}|^2 \rangle^{1/2}$. Nous avons trouvé des valeurs de l'ordre de $\langle |\chi_{NPS}^{(3)}(3\omega = \omega + \omega + \omega)| \rangle \sim 10^{-18} \text{ m}^2/\text{V}^2$ pour ces particules de ZnO. On peut noter que nous avons développé en parallèle au laboratoire un protocole de mesure de susceptibilité basé sur la technique de diffusion de troisième harmonique, et que les deux méthodes donnent des valeurs de

susceptibilité similaires qui correspondent par ailleurs aux valeurs obtenues sur des cristaux massifs.

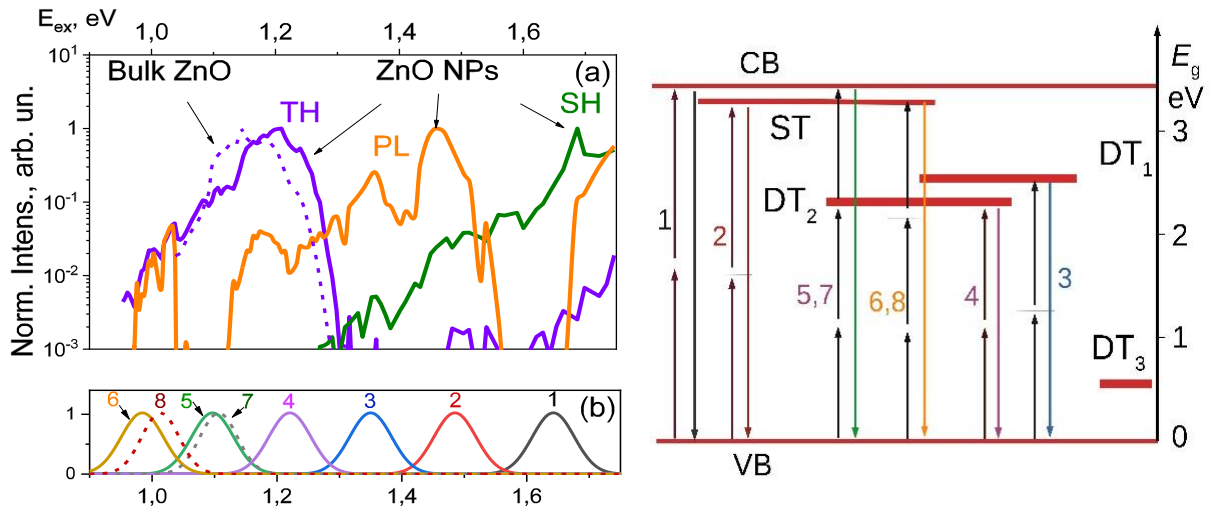


Figure 2. (a) Intensité normalisée (échelle logarithmique) de deuxième, troisième harmoniques et de PL en fonction de la longueur d'onde d'excitation pour un nanocristal de ZnO (~150 nm) - Intensité THG pour un cristal massif de ZnO pour comparaison [95]. (b) Positions des niveaux d'énergie associées aux défauts, obtenues par l'analyse de la photoluminescence de cristaux massifs de ZnO. Ces niveaux peuvent être excités par deux (lignes solides) ou trois (lignes en tirets) photons. (c) Schéma des mécanismes possibles d'amplification résonante de la génération d'harmoniques [67].

Par la suite, afin d'étudier la réponse individuelle des nanoparticules, un prototype de microscope multiphotonique a été développé. Il est basé sur un laser femtoseconde accordable sur une plage de longueurs d'onde de 710 à 1300 nm. Avec ce système, il devient possible de sonder la réponse des particules en fonction de la longueur d'onde d'excitation. Pour des NPs de ZnO de taille <150 nm, nous observons principalement des signaux de second et de troisième harmonique, et de photoluminescence (PL). Comme le montre la figure 2, chaque processus est favorisé sur une plage de longueurs d'onde spécifique.

Pour interpréter ces différentes réponses, nous proposons (chapitre 4) une analyse des propriétés de cristaux massifs de ZnO. L'intérêt de cette étude est la très bonne connaissance de la structure de défauts sur ces cristaux, qui permet d'analyser et d'interpréter les réponses optiques non linéaires quadratiques et cubiques. En particulier, en utilisant la technique I-scan, nous avons mesuré l'indice de réfraction non linéaire (partie réelle et imaginaire) des cristaux et corrélié la réponse avec les données de la spectroscopie PL et infrarouge. Il a également été démontré la sensibilité de la diffusion optique (indicatrices de diffusion) à la concentration des défauts. Enfin, l'ensemble des données a été utilisé pour interpréter la réponse spectroscopique obtenue sur les nanoparticules individuelles.

En effet, la figure 2 distingue trois gammes de longueurs d'onde pour lesquelles une amélioration du signal est observée : (1) $\lambda < 1000$ nm (1.24 eV), (2) 1000 nm (1.24 eV) $< \lambda < 1100$ nm (1.13 eV), (3) $\lambda > 1150$ nm (1.08 eV). Dans la plage (1), la SHG et la PL sont favorisées en raison de l'excitation à deux photons de la bande interdite et des niveaux réels de défauts (voir Figure 2c). La bande (2) est caractérisée par une haute efficacité de la troisième harmonique, due à l'excitation directe à trois photons de la bande interdite et des niveaux de défauts. Dans la gamme (3), la troisième harmonique est amplifiée en raison de l'excitation à trois photons des niveaux proches du bas de la bande de conduction. Nous avons donc observé une corrélation très intéressante entre la structure des niveaux d'énergie du ZnO et la

réponse optique non linéaire. Ces premières données doivent encore être confirmées, mais elles montrent l'intérêt du dispositif expérimental mis au point, qui permet de réaliser une spectroscopie optique non linéaire de nano-objets individuels.

Dans le chapitre 5, l'influence du dopage de monocristaux de KDP sur les propriétés optiques a été étudiée. En particulier, il a été démontré que l'incorporation de TiO_2 induit une augmentation de l'efficacité SHG de 60 / 35 % pour les secteurs de croissance pyramidaux / prismatiques sous excitation laser femtoseconde à 800 nm. Une augmentation d'un facteur 10 pour la SHG a été observée pour KDP:NOA par rapport à un cristal KDP nominale pur sous excitation laser nanoseconde à 1064 nm [4]. D'autre part, nous avons étudié les indicatrices de diffusion de ces cristaux. Sur des cristaux de KDP nominale purs, il a été démontré que les pertes de diffusion élastique à 1064 nm sont supérieures à celles des cristaux de KDP: TiO_2 , en raison d'une concentration inférieure d'impuretés non contrôlées dans les cristaux dopés[68]. Nous avons aussi montré que les pertes de diffusion dans un monocristal de KDP:NOA dépendent de la concentration en nanofibres de NOA. Des mesures précises de l'indice de réfraction non linéaire ont enfin été réalisées, montrant la grande influence du dopage des cristaux sur ces propriétés.

Acknowledgement

The author expresses his sincere gratitude to the thesis directors V. Gayvoronsky and R. Dantec for the permanent support and fruitful discussions in the process of scientific research and preparation of the thesis. The author is also grateful to A. Uklein and J. Riporto for their assistance in performing the experiments in Ukraine and France correspondingly. Many thanks to V. Lisnyak, M. Urbain and Y. Mugnier for the results of chemical analysis, synthesis and preparation of the samples for the research. This work was financially supported by PHC Dnipro project 37824WJ. Author also thanks the French Embassy in Ukraine and the Auvergne Rhône Alpes Région (CMIRA 2016 - Accueil DOC) for travel and accommodation scholarships.



Résumé :

Ce travail porte sur la détermination expérimentale des propriétés optiques linéaires et non linéaires de nanoparticules harmoniques - une nouvelle classe de marqueurs biologiques - et de cristaux massifs de KDP avec incorporation de nanoparticules d'oxydes métalliques. Nous avons mis au point une série de bancs expérimentaux dédiés, comme la mesure des indicatrices de diffusion, la technique I-scan pour la mesure de l'indice de réfraction non linéaire, la mesure de l'efficacité de génération de troisième harmonique (THG), ou le développement d'un microscope multiphotonique sous excitation laser femtoseconde dans le domaine spectral 710 - 1300 nm.

Des mesures de susceptibilité non linéaire d'ordre 3 ont été effectuées sur des suspensions colloïdales de nanoparticules de ZnO par la technique de la THG aux interfaces, montrant une valeur de susceptibilité proche de la valeur de référence des cristaux massifs. Par ailleurs, les propriétés optiques de ces nanoparticules ont été étudiées par microscopie multiphotonique. Les spectres d'émission des nanoparticules montrent des signaux de génération de second harmonique (SHG), de THG et de photoluminescence, dont la réponse spectrale a été corrélée avec une étude portant sur la spectroscopie de défauts de cristaux massifs de ZnO. Par ailleurs, nous avons étudié l'influence sur les propriétés optiques de l'incorporation de nanoparticules d'oxyde métalliques dans des cristaux KDP. Il a été démontré que ces nanoparticules peuvent être à l'origine d'une augmentation de l'efficacité de SHG par comparaison avec un cristal de KDP pur. Un ensemble de mesures optiques a été réalisé sur ces cristaux composites, démontrant en particulier la corrélation entre les effets non linéaires d'ordre 3 et l'augmentation observée.

Abstract:

This work focuses on the experimental characterization of the linear and nonlinear optical properties of harmonic nanoparticles - a new class of biological markers - and of composites based on KDP single crystals with incorporated metal oxide nanoparticles. We have developed several experimental setups, such as light scattering indicatrices technique, laser beam self-action analysis, the third harmonic generation efficiency (THG) measurements, and multiphoton microscopy with femtosecond laser excitation in the 710 - 1300 nm spectral range.

The third order susceptibility measurements were performed by analyzing the THG at the interface of a cuvette filled with ZnO colloidal suspensions, showing a susceptibility value close to the reference value of the bulk crystal. In addition, the optical properties of these nanoparticles were studied with multiphoton microscopy. The emission spectra of the nanoparticles show the second harmonic generation (SHG), the THG and photoluminescence signals. The spectral response has been correlated with the structure of defects in bulk ZnO crystals. In addition, we studied the influence of the incorporation of metal oxide nanoparticles into KDP crystals. It has been shown that these nanoparticles can increase the SHG efficiency compared to nominally pure KDP crystal. A set of optical measurements was carried out on these composite crystals, demonstrating the relationship between the third order nonlinear optical effects and the observed SHG efficiency enhancement.

Keywords: second and third optical harmonics generation; zinc oxide; harmonic nanoparticles; laser radiation self-action effects; elastic optical scattering; KDP.

